Integrated Computational Materials Design for Alloy Additive Manufacturing: Introducing Data-Driven Approach to Physical Metallurgy

by

Xin Wang

Bachelor of Engineering, Dalian University of Technology, 2014

Master of Engineering, Shandong University, 2017

Submitted to the Graduate Faculty of the

Swanson School of Engineering in partial fulfillment

of the requirements for the degree of

Doctor of Philosophy

University of Pittsburgh

2023

UNIVERSITY OF PITTSBURGH

SWANSON SCHOOL OF ENGINEERING

This dissertation was presented

by

Xin Wang

It was defended on

April 7, 2023

and approved by

Brian Gleeson, Professor, Mechanical Engineering and Materials Science

Albert C. To, Ph.D., Professor, Mechanical Engineering and Materials Science

Jörg Wiezorek, Professor, Mechanical Engineering and Materials Science

Mostafa Bedewy, Assistant Professor, Mechanical Engineering and Materials Science

Qing Chen, Adjunct Professor, Materials Science and Engineering, KTH Royal Institute of Technology

Dissertation Director: Wei Xiong, Ph.D., Associate Professor, Mechanical Engineering and Materials Science

Copyright © by Xin Wang

2023

Integrated Computational Materials Design for Alloy Additive Manufacturing: Introducing Data-Driven Approach to Physical Metallurgy

Xin Wang, Ph.D.

University of Pittsburgh, 2023

Additive manufacturing (AM) attracts broad interest due to its ability to produce complex geometries, fast prototyping, and in-situ repair. However, AM involves many parameters and uncertainties, which lead to products property variation. For instance, the influence of composition variation on AM component is an important issue that has not been thoroughly studied. Moreover, micro-segregation in AM caused by the high-cooling rate makes the as-built structure and properties vary locally within the prints. The alloy bulk properties may change with different AM processing parameters. Such variations must be studied while the experimental study is time- and cost-consuming.

This thesis introduced the data-driven approach, such as statistical analysis, machine learning, and Bayesian inference combined with integrated computational materials engineering (ICME), to address the AM property variation challenges. Firstly, the process-structure-property-performance (PSPP) relationships for AM high-strength low-alloy (HSLA) 115 steel with post-treatment were established to study feedstock composition impact on the print performance. High-throughput calculations of the ICME framework quantified uncertainties in critical properties, such as yield strength, printability, and low-temperature ductility, with the feedstock composition variation. Moreover, the machine learning approach was implemented to surrogate the ICME model framework for an accelerated simulation for a more comprehensive study and robust feedstock composition optimization. Finally, the printed optimized HSLA 115 steel showed excellent properties even though the printed composition differs from the designed composition,

which proves the successfulness of the design with uncertainty in composition. This thesis studied the impact of AM 316L stainless steel segregation on the deformation mechanism and mechanical properties. A machine learning-based stacking fault energy (SFE) predictor, which surpassed the conventional thermodynamic and empirical models, was developed to predict the SFE change with segregation in AM. This data-driven model successfully explained the twinning behavior in as-built AM 316L. Finally, a Bayesian-based model calibration was applied to understand the considerable variation in the mechanical properties of CoCrFeMnNi HEAs with different AM techniques and processing parameters. It revealed the importance of dislocation density and grain size in strengthening the AM products, and correlation analysis was conducted to find the relationship between the strengthening mechanism and processing parameters.

Table of Contents

List of Tables

List of Figures

Acknowledgement

First, I would like to sincerely thank my advisor, Dr. Wei Xiong, for his unwavering support, encouragement, and mentorship throughout my Ph.D. studies. His intellectual guidance, encouragement, and patience have been invaluable in shaping my research work. Over the years, Dr. Xiong has provided me with valuable guidance on my research work and has been an excellent role model in many other aspects of my academic and personal life. His enthusiasm and positive attitude have inspired me to strive for excellence.

I am also grateful to my committee members, Dr. Brian Gleeson, Dr. Albert C. To, Dr. Jörg Wiezorek, Dr. Mostafa Bedewy, and Dr. Qing Chen, for their constructive feedback and support, which have helped me to refine and improve my research work.

I am deeply grateful to my colleagues and friends, especially those in my research group, for their support and encouragement for creating a pleasant, collaborative, and stimulating research environment. I am grateful for the friendship, collaboration, and experiences that have enriched my Ph.D. study.

Finally, I would like to express my deepest gratitude to my family, especially my father and mother, who have been a constant source of love, encouragement, and support throughout my academic journey. Their unwavering belief in me and their sacrifice have been crucial in enabling me to achieve this milestone in my academic career. I want to dedicate my thesis to them as a token of my love, gratitude, and appreciation for everything they have done for me.

List of Publications

1. **Wang, X.,** et al. (2022). Design metastability in high-entropy alloys by tailoring unstable fault energies. *Science advances*, *8*(36), eabo7333.
2. **Wang, X.,** & Xiong, W. (2020). Uncertainty quantification and composition optimization for alloy additive manufacturing through a CALPHAD-based ICME framework. *npj Computational Materials*, *6*(1), 1-11.
3. **Wang, X.,** Sridar, S., & Xiong, W. (2020). Thermodynamic investigation of new high-strength low-alloy steels with heusler phase strengthening for welding and additive manufacturing: high-throughput CALPHAD calculations and key experiments for database verification. *Journal of Phase Equilibria and Diffusion*, *41*(6), 804-818.
4. **Wang, X.,** & Xiong, W. (2020). Stacking fault energy prediction for austenitic steels: thermodynamic modeling vs. machine learning. *Science and Technology of Advanced Materials*, *21*(1), 626-634.
5. Sridar, S., Zhao, Y., Li, K., **Wang, X.**, & Xiong, W. (2020). Post-heat treatment design for high-strength low-alloy steels processed by laser powder bed fusion. *Materials Science and Engineering: A*, *788*, 139531.
6. Hoffman, A., Arivu, M., Wen, H., He, L., Sridharan, K., **Wang, X.**, et al. (2020). Enhanced resistance to irradiation induced ferritic transformation in nanostructured austenitic steels. *Materialia*, *13*, 100806.
7. Sridar, S., Sargent, N., **Wang, X.**, et al. (2022). Determination of Location-Specific Solidification Cracking Susceptibility for a Mixed Dissimilar Alloy Processed by Wire-Arc Additive Manufacturing. *Metals*, *12*(2), 284.

8. De Vecchis, R. R., **Wang, X**., et al. (2022). Introducing Heusler intermetallics for synergic effect of grain refinement and precipitation strengthening in high-strength low-alloy steels. *Journal of Alloys and Compounds*, *904*, 163885.
9. Sridar, S., **Wang, X.**, et al. Design of Graded Transition Interlayer for Joining Inconel 740H Superalloy with P91 Steel using Wire-arc Additive Manufacturing, Meeting: 10th International Symposium on Superalloy 718 and Derivatives, (2023), Proceedings: Superalloy 718 & Derivatives
10. Sargent, N., Wang, Y., Li, D., Zhao, Y., **Wang, X.,** & Xiong, W. (2023). Exploring Alloy Design Pathway Through Directed Energy Deposition of Powder Mixtures: A Study of Stainless Steel 316L and Inconel 718. Additive Manufacturing Letters, 100133.

List of Abbreviations, symbols, and nomenclature

Abbreviations	Meaning
AM	Additive manufacturing
ASTM	American society for testing and materials
CAD	Computer-aided design
DBTT	Ductile-brittle transition temperature
SHAP	Shapley additive explanations
ML	Machine learning
ICME	Integrated computational materials engineering
CALPHAD	Calculation of phase diagrams
DSC	Differential scanning calorimetry
EBSD	Electron backscatter diffraction
EDM	Electric discharge machining
EDS	Energy-Dispersive X-ray Spectroscopy
FEA	Finite element analysis
HAGB	High-angle grain boundary
HIP	Hot isostatic pressing
HSLA	High-strength low-alloy
ITT	Impact transition temperature
LAGB	Low-angle grain boundary
LHS	Latin hypercube sampling
MAE	Mean absolute error
PSPP	Process-structure-property-performance
PF	Phase field
RMSE	Root mean square error
SD	Standard deviation
SEM	Scanning electron microscopy
SFE	Stacking fault energy
TRIP	Transformation-induced plasticity
TWIP	Twinning-induced plasticity
UE	Uniform elongation
UMFE	Unstable martensite fault energy
UTFE	Unstable twin fault energy
UTS	Ultimate tensile strength
YS	Yield strength

1.0 Introduction

1.1 Additive Manufacturing

Additive manufacturing (AM), a technique that fabricates components by printing layer by layer with a computer-aided design (CAD) file, is capable of producing complex geometries, rapid-prototyping with low cost, and performing in-situ repair tasks [1,2]. Due to those advantages, AM has gained various interests from the academic community and industrial fields, making a market worth billions of dollars [3]. The current AM approach can work with different materials, such as polymers, ceramics, metals, etc., and the AM techniques have been successfully commercialized with polymers [4]. On the contrary, metal AM greatly impacts many industrial fields, and various technical barriers remain to be solved [5].

As defined by the American Society for Testing and Materials (ASTM) Internal Committee F42, the AM processes fall into seven categories: 1. Vat photopolymerization, 2. Material jetting, 3. Binder jetting, 4. Material extrusion, 5. Powder bed fusion, 6. Sheet lamination, and 7. Directed energy deposition [6]. For metal AM, the most common techniques are powder bed fusion (PBF) and directed energy deposition (DED), which make up 70% of the metal additive manufacturing market [1]. Their difference is that a PBF will have the powder evenly distributed. Only the energy source, such as the electron/laser beam [7], will move as the designed pattern to selectively fuse metallic powder particles layer over layer, where the process is illustrated in Fig.1-1. On the contrary, the material feeder and the energy source will move in the DED technique. Compared to

the PBF, the DED is cheaper and good at shaping complex geometries, while the accuracy is not comparable with PBF [8].

The manufacturing process of PBF and DED approaches seems to be simple, while there are complex physical phenomena in the whole process, such as rapid melting and solidification, evaporation, and complex thermal history when the heat source moves within the same layer and moves between successive layers. All of those are controlled by the feedstock properties and composition, printing parameters like the scan pattern and speed, heat source power, layer height, beam diameter, and hatch space. Moreover, the combination of the numerous parameters and complex physics will lead to different grain sizes, precipitates, porosities, etc., making the final product performance vary and hard to be qualified for certain engineering applications [9].

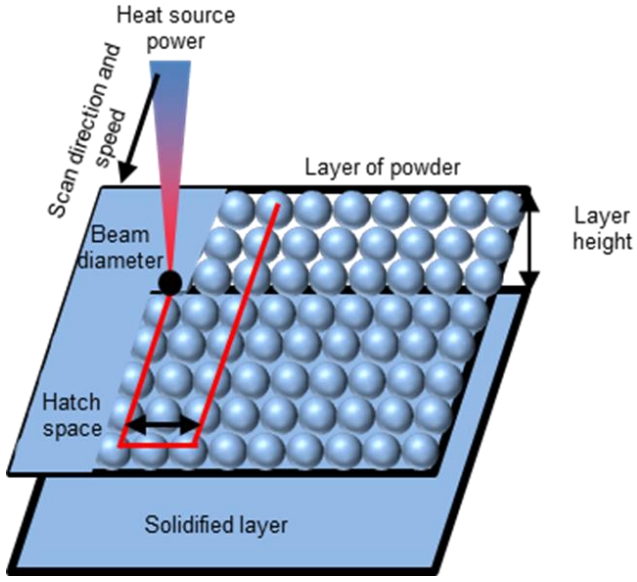

Figure 1-1 Schematics of the powder bed fusion process. The common processing parameters are 1. Power: Energy delivered by the heat source. 2. Beam diameter: Diameter of the heat source on the powder bed. 3. Scan speed: Travel speed of heat source. 4. Layer height: Thickness of each layer. 5. Hatch space: Distance between two consecutive scans. Figures adopted and modified from [9] under the terms of the Creative Commons CC-BY license.

1.2 Integrated Computational Materials Engineering (ICME)

1.2.1 ICME in AM

To better control the AM components' performance and make it satisfy the stringent requirements for industrial application, we need to gain an in-depth understanding of the process-structure-property-performance (PSPP) relationship throughout the manufacturing process. However, the traditional experiment-based Edisonian approach is insufficient and impractical to explore the multicomponent alloys and understand the large design space in AM. Meanwhile, the rapidly growing computing power and well-developed simulation tools provide a new approach, i.e., integrated computational materials engineering (ICME) [10–12], for predicting properties, designing alloys, and optimizing printing parameters and post-heat treatment conditions. It integrates various computation tools and databases to simulate the product from the atomistic level to the bulk components and shortens the time needed for alloy development from 10-20 years to around two years [13]. Many countries have acknowledged and embraced the concept of ICME due to its potential to utilize computational materials engineering in the future industry [14].

The keys in ICME include process, structure, property, performance, and the linkage between the four aspects. Moreover, the PSPP relationships for AM differ from the conventionally manufactured materials, which brings new challenges in applying ICME for metal AM.

- For process, AM alloys undergo a very complex thermal, mechanical, and composition change, which are determined by the feedstock properties, the AM processing parameters, and the post-treatment. From feedstock to post-treatment,

the large design space provides much freedom in tuning the material's structure and properties. At the same time, the numerous choices of parameters may impede a successful design with a trial-and-error approach. Understanding the influence of the feedstock and parameters on product performance is vital for the AM [15], while such a thorough understanding is not sufficiently studied [16,17].

- For structure, the microstructure of metals is usually described by the grain size, dislocation densities, precipitation fractions, and porosities in materials science. However, AM products show more unique structures than conventionally manufactured metals, such as elongated columnar grains, higher dislocation density, and different types of pores [18]. Moreover, the AM local composition and microstructure may change at the voxel level, whether controlled or stochastic [19], bringing challenges in understanding the properties.
- For property, it varies based on the application of the material, such as thermal conductivity, corrosion, and oxidation resistance. This thesis will mainly focus on mechanical properties, such as yield strength, low-temperature ductility, and deformation mechanisms.
- For performance, it means the product meets all requirements for its application. It is a comprehensive evaluation of multiple property requirements.

The foundations of a successful ICME framework include a comprehensive understanding of the PSPP relationship, accurate and feasible modeling tools, reliable databases, and a seamless linkage between each model. Currently, most of the ICME modeling work for AM focuses on the AM process, where the details have been summarized by Hu *et al.* [20]. The heat source model,

powder bed model, melting pool model, etc., can be applied to predict the properties and performance of AM products. For example, with the input parameters, such as the scan speed, laser power, and particle size distribution, the melting pool model enables the prediction of melt pool geometry, thermal boundary conditions, and surface roughness [21–26]. Then, the predicted thermal boundary conditions can serve as inputs for the finite element analysis (FEA)-based or phase-field method (PF)-based residual stress model to predict the residual stress, shrinkage, and deformation of the final products [25,27,28]. In terms of the alloy design, the CALPHAD (CALculation of PHase Diagrams) [14,29–31] has been well developed for modeling the phase transformation in various alloys. Moreover, the *ab initio* method based on the density functional theory predicts structure and property on a small scale [32].

However, the computational resources for the abovementioned approaches will be extensive when integrated for massive calculations required for AM with ample design space and complex physics [33]. In the meantime, the wealthy data generated during production, academic research, and the data-driven approach provide an alternative way to the existing ICME model framework and can be applied for more detailed study [34].

1.2.2 Data-Driven Approaches and Applications for AM

Incorporating data-driven approaches, such as machine learning and deep learning, is recognized as the ‘fourth paradigm of science’ [35] and the ‘fourth industrial revolution’ [36]. It shows great potential in enhancing the role of computational materials in materials science, such as property prediction, materials discovery, and process optimization [37–41], due to the unique

advantages of the machine learning method compared with the traditional modeling approaches [37,41–45]. First, it is easy to use. Building a machine learning model requires constructing a database, selecting the algorithm and training the model, and evaluating the performance [41]. It does not require skillful and knowledgeable researchers to master the relationship between each input and the property of interest to ensure the correct prediction. The machine learning algorithms will automatically model the hidden links in each attribute. Second, suppose the machine learning model has been established. Once the new experiments have been performed, the latest data could be easily incorporated into the model and enhance the model's performance. This feature offers an advantage for automated model improvement as the new data are generated during industrial production and academic research. Finally, the machine learning model is fast and accurate if enough data and the appropriate algorithm have been used to build the model.

In addition to machine learning, the Bayesian statistical method can bridge the model and the experimental data and improve the ICME model accuracy. By providing a few experimental data, it can calibrate either a machine learning surrogate model or physics-based material property models for more accurate prediction and quantify the uncertainty of the model parameters that offers an in-depth understanding of physics [46,47].

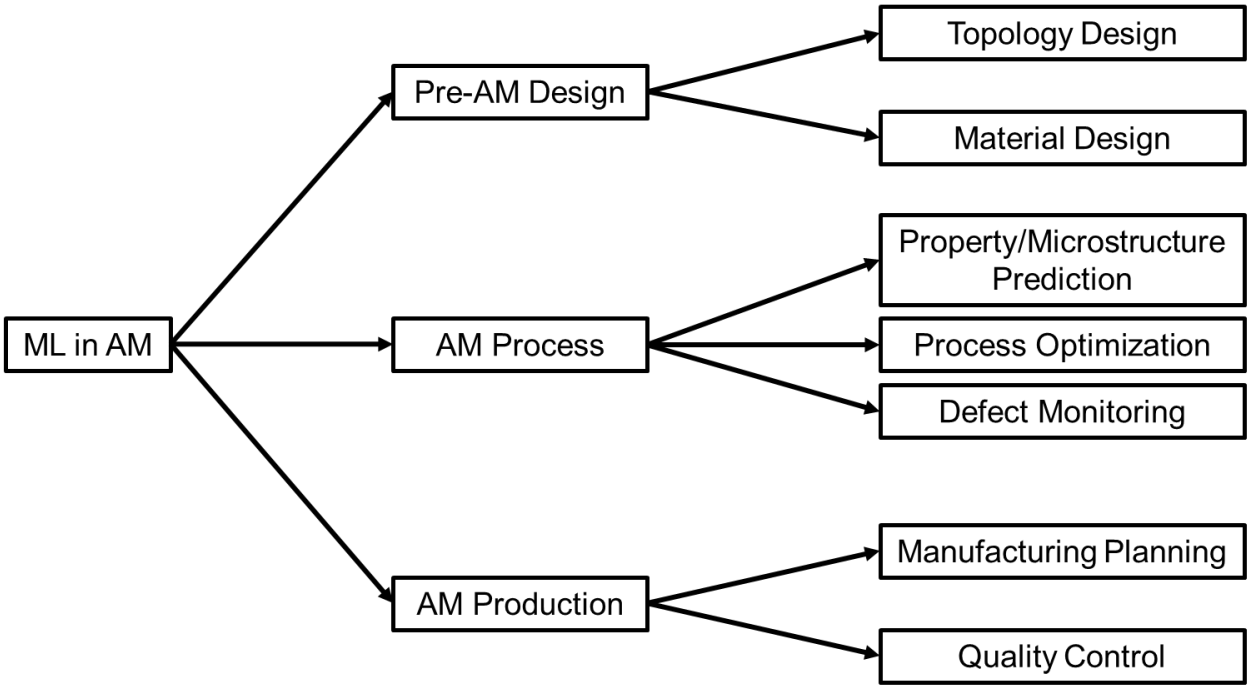

Figure 1-2 Application of machine learning in additive manufacturing.

Currently, many works utilize the data-driven approach for AM [48]. As shown in Fig. 1-2, the current applications include the design before the product, such as topology and feedstock design, and the design for AM processes, which includes optimizing the processing parameters and printing the microstructure. Finally, it is also capable of manufacturing planning. For example, Cang et al. [49] used the neural network for topology design with minimized compliance. Martin et al. [50] applied an algorithm to search through 4500 different possible nucleates and find the one that makes the laser powder bed fusion (LPBF) Al alloy with desired microstructure. Tapia et al. [51] also demonstrated that machine learning could surrogate the physics model and predict the melt pool depth with printing parameters accurately and quickly. Mech et al. [52] demonstrated using the machine learning approach for estimating build time for better planning the AM

production. As materials research, this thesis will not cover all applications of ML in AM but mainly focus on using data-driven ICME for material design, property prediction, and the PSPP relationship for AM.

1.3 Challenges in AM – Variation in Composition, Structure, and Property

Figure 1-3 shows the three types of variation in the additive manufacturing process that will be addressed in this work. The feedstock quality may vary in different batches. The deviation from the desired composition could lead to detrimental phase formation during solidification [53] and post-heat treatment [54] and lead to undesired properties. The second problem is that AM prints usually have micro-segregation and ununified properties due to rapid cooling [55]. Last, the yield strength of the AM alloy with the same composition is found to have a significant difference. A detailed discussion of the three variations is given in the following context.

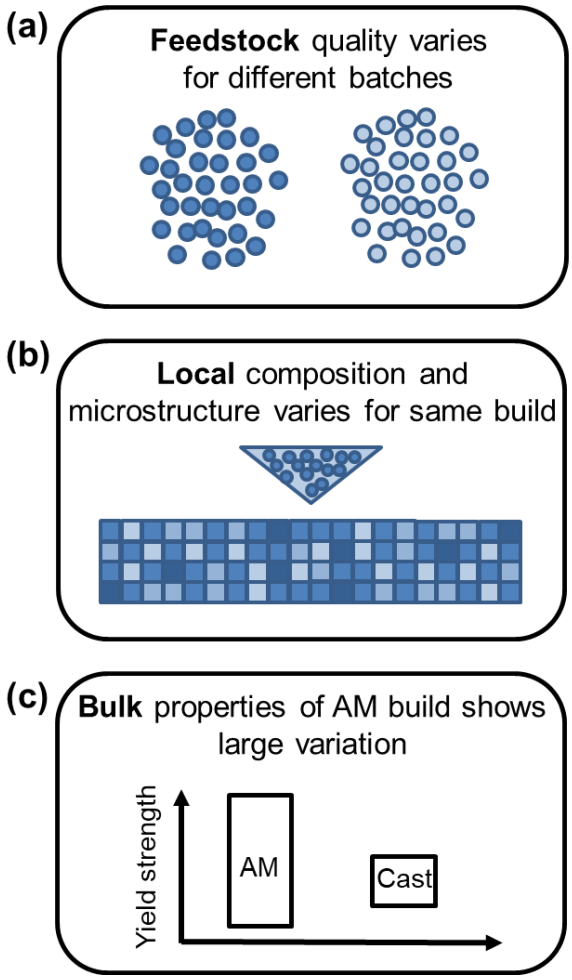

Figure 1-3 Common properties variation in AM. (a) The feedstock composition varies in different batches. (b) During the printing, the as-built prints may have different compositions at different locations due to micro-segregation and other reasons. (c) the yield strength varies for the same alloy with different processing parameters and different manufacturing approaches.

1.3.1 Variation of Feedstock Composition

1.3.1.1 Problem Statement

Uncertainty quantification is essential for quality control in AM. Based on the given uncertainty of processing parameters, uncertainty quantification can determine the microstructure variation and mechanical properties for AM builds. Currently, most uncertainty quantification studies focus on manufacturing processes [20,21,56]. However, the influence of uncertainty in the feedstock is often overlooked. The cost of metal materials is the second-highest in AM part [57], and the feedstock quality plays a vital role in the AM build performance. Moreover, the choice of commercialized AM powder is much less than the alloys manufactured by the conventional manufacturing approach, and not all existing alloys are suitable for metal AM [58], such as, using the alloys designed for casting may result in poor processibility in AM process. As a result, composition adaptation is required to enhance processability and functionality for 3D printing of conventional alloys [59].

Many works have studied the feedstock density impact on the final product porosity [60] and the influence of powder size distribution and morphology on the process quality [61,62]. In contrast, the impact of the composition variation is not well studied for the post-heat-treated AM products. Deviation from the desired composition could lead to detrimental phase formation during solidification [53] and post-heat treatment [54]. It may also introduce cracks and pores and alter physical properties such as specific heat and melting point, further influencing the choice of processing parameters [63]. Moreover, the composition variation in AM products is unavoidable, which comes from various sources. First, the powder composition varies in different batches [64].

Additionally, a large amount of unprinted powder needs to be recycled after the AM process to improve sustainability, which causes degradation with contamination. The above composition-related issues propagate uncertainty throughout the AM process and should be addressed during the composition design of the feedstock material. This implies that the nominal composition of an alloy needs to be well-designed to avoid the negative impact of the uncertainty on the final build. However, the study of the relationship between alloy composition and the performance of AM builds after post-treatment is limited. Only a few studies have reported the impact of composition variation on the AM builds with experiments [65,66]. Moreover, the comprehensive modeling tool to facilitate decision making on the composition range in feedstock manufacturing is yet unavailable.

1.3.1.2 Study Case

Unlike commercialized alloy powder such as Inconel 718, Ti-64, and Stainless Steel 316, many alloys have not been massively produced for AM, and the production of customized powder is usually in a small batch and expensive. For example, high-strength low-alloy steels are widely used in many structural applications, such as bridges, ship hulls, and mining equipment [67–70]. Due to the excellent mechanical properties and good weldability, HSLA-115 steel is an outstanding candidate for AM, but no commercial powder is available. Moreover, the powder vendor Praxair, Inc. provides a composition range for the powder that is based on the wrought HSLA composition. For example, the carbon content ranges from 0.027 to 0.078 wt.%. However, we do not know if the composition in the specified range will meet all property requirements. The printed component should have a yield strength higher than 115 ksi, a low ductile-to-brittle

transition temperature (DBTT), and good printability that has high density and can avoid cold cracking [71] and hot cracking [72] in the products.

As a result, there is a need to develop a method to quantify the impact of the feedstock composition variation in the final product and optimize the nominal composition that can still perform well with the composition variation.

1.3.1.3 Proposed Solution

The first step is to build a CALPHAD-based ICME model framework to optimize the composition and predict the key properties based on the alloy composition. The CALPHAD method in combination with phenomenological models was applied for predicting the dislocation density [73], grain size [74,75], impact transition temperature (ITT) [76], and carbon equivalent [77]; 2) Data-mining decision tree model for martensite start (M_S) temperature [78]; and 3) Physics-based strengthening model [79] consisting of the simulation of hardening effect caused by dislocations [80], grain boundaries [81,82], precipitates [83,84] and solid solution atoms [85,86] to predict the key properties like yield strength, low-temperature ductility, and weldability for a given composition and heat treatment process. However, this approach is computationally intensive and only suitable for the reliability design, and there is a need for a faster prediction with more comprehensive research.

The second step is using machine learning to surrogate the ICME model framework to accelerate the calculation and perform the robust design to discover more compositions and predict the mean and standard deviations (SD) of critical properties for a given nominal composition with

uncertainty. This helps us conduct more simulations and gain an in-depth understanding of the uncertainty propagation from the feedstock composition to the final product properties.

Finally, the powder with optimized composition was printed, and its properties were verified through a systematic microstructure characterization. Based on the results, this study has been proven effective and can be applied to other alloy composition optimization to expand the choices of alloys for additive manufacturing. The details of the design process and verification are available in Chapter 3.

1.3.2 Variation of Local Composition and Properties

1.3.2.1 Problem Statement

Due to the high-speed cooling rate [87–89] of additive manufacturing, the solutes will partition from the dendrites into the surrounding liquid, which will not have enough time to reach the equilibrium states. This will result in the composition gradient in additively manufactured products and leaves the chemical heterogeneity and various properties [90]. The hierarchical structure and composition gradient enables some unique properties in AM, while the varying local composition also requires more experiments or simulation to understand the structure and properties variation in the AM prints. Thus, fast and accurate models for property prediction are necessary for AM.

1.3.2.2 Study Case

The AM 316L stainless steel shows higher yield strength, elongation, and tensile strength than the cast form [18,91,92]. Furthermore, the excellent mechanical properties were attributed to high dislocation density, twinning-induced plasticity (TWIP), and fine subgrain structure [18]. TWIP can improve the strength and ductility simultaneously during deformation by forming twin boundaries to hinder dislocation movement [93,94]. Moreover, the TWIP phenomenon is achievable when Stacking fault energy (SFE), which is related to the energy required for dissociating a perfect dislocation into two partial dislocations along with the formation of a stacking fault [95], lies between 20-40 mJ/m^2(Fig. 1-4) [96]. However, the SFE of TWIP AM 316L stainless steel is measured to be 46 mJ/m^2 [97], while Pham et al. claimed that their TWIP AM 316L stainless steel has low SFE due to the nitrogen gas used in printing without measuring or calculating the SFE. Thus, it is necessary to consider the segregation and understand the impact on SFE to reveal why TWIP is a common and pronounced strengthening mechanism in AM 316L stainless steel.

The SFE can be measured by experimental methods, including transmission electron microscopy [98–100] and X-Ray/Neutron diffraction [101,102], which are time-consuming and complex. Computational methods such as empirical equations, *ab initio* calculations, and thermodynamic models may serve as alternative solutions for SFE prediction. But none of those modeling tools are accurate and quick at the same time. (Detailed discussion in Chapter 3).

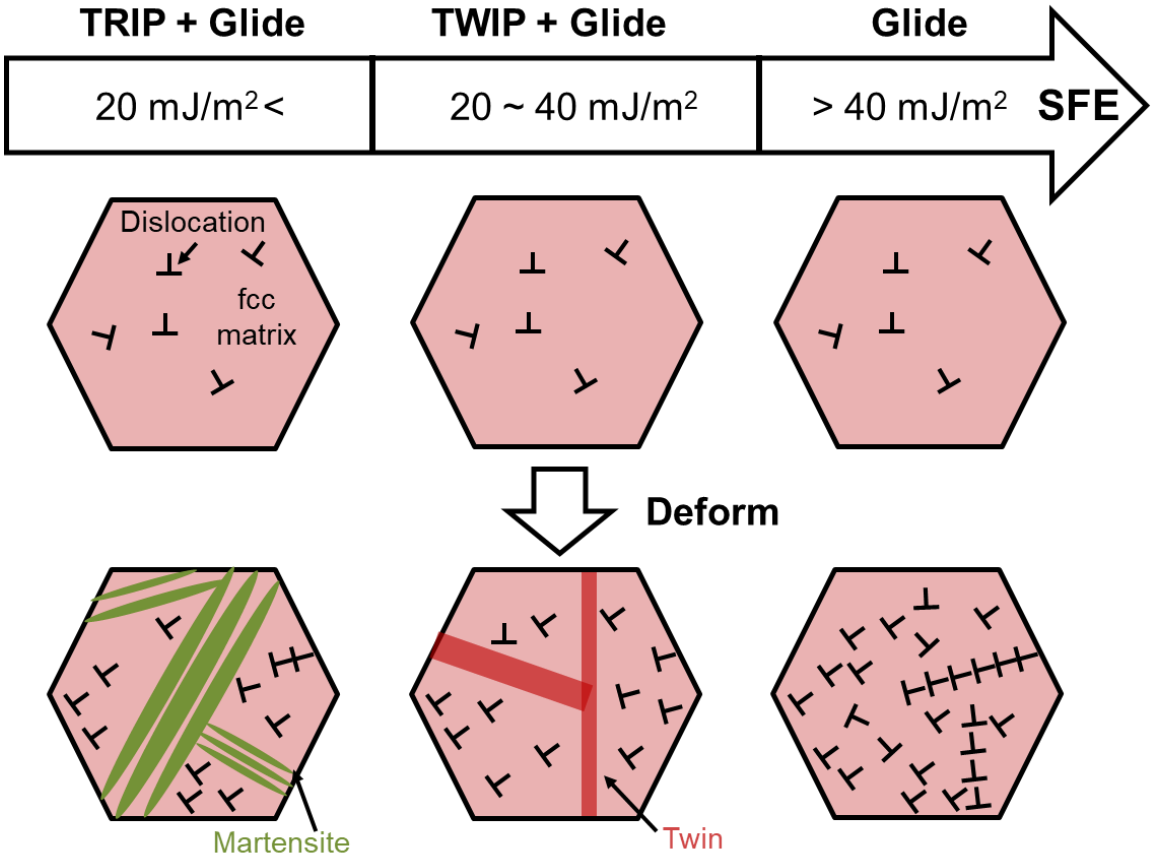

Figure 1-4 The schematic of stacking fault energy and the deformation mechanisms.

1.3.2.3 Proposed Solution

In this thesis, hundreds of compositions and experiments measured stacking fault energies were collected. This database will be used as an input for the machine learning model to learn the relationship between composition and SFE. The relationship found by the model will be revealed by the explainable ML tools such as SHAP. Finally, the model will be used for predicting the SFE change with the segregation profile simulated by Scheil prediction for 316L. Finally, the critical stress for twinning with nominal composition and segregation profile will be compared to elucidate why TWIP is operatable in AM 316L stainless steel.

1.3.3 Variation of Bulk Properties for Same Alloy

1.3.3.1 Problem Statement

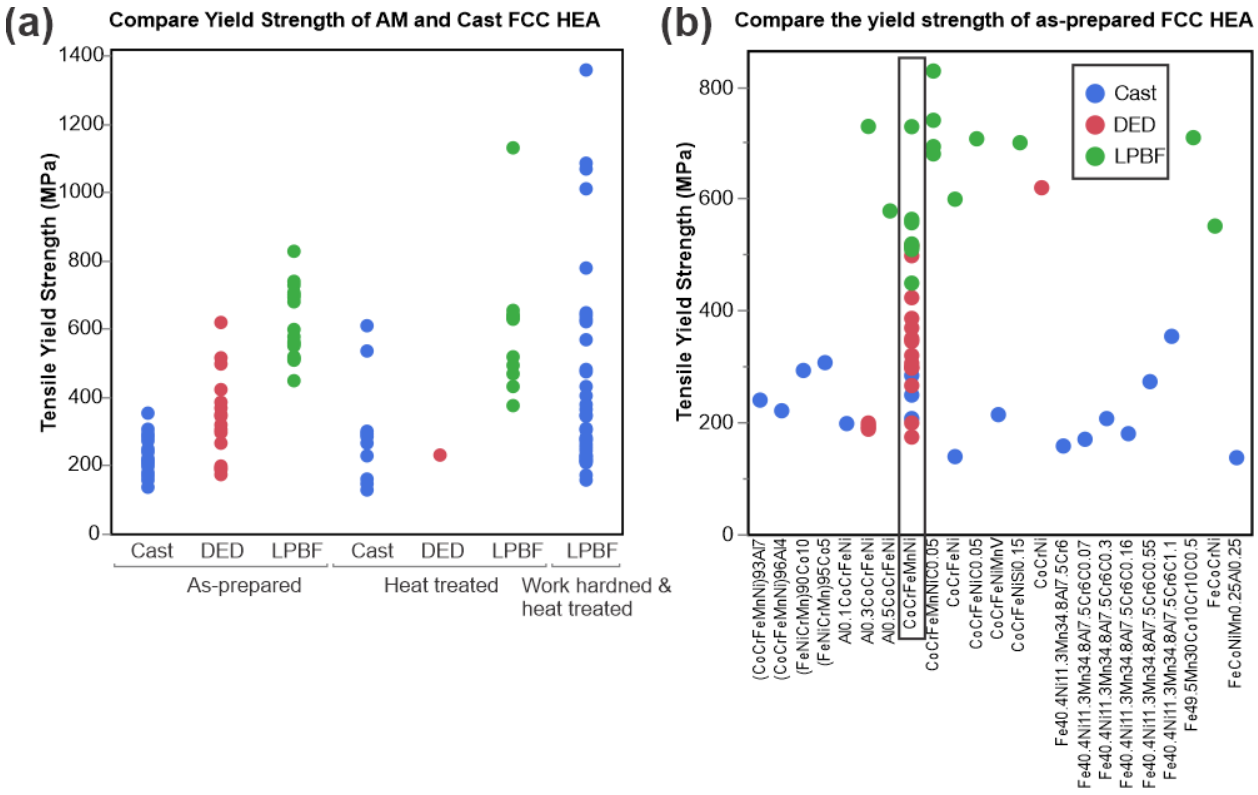

Figure 1-5 Literature review of the tensile test yield strength difference between fcc HEAs made by DED, LPBF, and cast. (a) Summary of the FCC HEA yield strength at as-built, heat treated, and work hardened with heat treatment status and (b) Summary of the as-prepared FCC HEA for different alloy compositions.

The yield strength of FCC high-entropy alloys, a new type of alloy that explores the vast composition with multi-principle elements, was summarized in Fig. 1-5(a). As for the as-prepared condition, the AM manufactured alloys tend to have higher yield strength than the cast alloys, and LPBF prepared HEAs will have higher yield strength than the DED manufactured samples, and

this phenomenon is kept even after the heat treatment. However, the cast alloy yield strength can be further tuned using work hardening and heat treatment to refine the grain size, increase dislocation density and introduce some precipitates. On the contrary, no AM HEA has been work hardened and heat-treated due to the neat-net shape nature of AM.

1.3.3.2 Study Case

Fig. 1-5(b) was plotted based on the alloy composition for the as-prepared FCC HEAs. The Cantor alloy CoCrFeMnNi [103] is the most studied FCC-type EA, and the cast alloys have a yield strength ranging from 200-300 MPa. The DED alloys show a more significant yield strength variation ranging from 200 to 500 MPa. The LPBF shows a yield strength of 400-700 MPa, much higher than cast and DED. Two following questions need to be addressed. 1. Why does the yield strength of AM alloy show a larger variation than the cast one? 2. What differences in the microstructure and process lead to a higher yield strength in LPBF and DED, and if we could control yield strength by tuning the process?

1.3.3.3 Proposed Solution

Setting up experiments and preparing the raw materials for the comprehensive study will rapidly increase costs. Thus, utilizing the existing data and exploring the relationship by reusing the experiment data is a good solution to reduce the overall time and resources. The Bayesian calibration approach [104–106] can utilize the experimental observations to adjust the model based on the conventionally manufactured alloy and correct the model inadequacy between the best-fitted model and observation to get the model that is suitable for AM alloy. With the iteration of

the model-guided designing and the model calibration process, we can develop an accurate model for AM alloys and understand the model parameters difference in the AM and conventionally manufactured alloys that can help us explain the structural difference in AM.

1.4 Objectives and Hypothesis

This research aims to develop an ICME modeling framework integrated with a data-driven approach to assist in designing advanced materials for additive manufacturing and gain an in-depth understanding of the impact of chemical composition, AM process, and post-treatment impact on the AM products' quality. It is hypothesized that by seamlessly integrating the CALPHAD method, physical-based models, and data-driven machine learning approach, we can understand and control the variation in AM feedstock, local properties, and bulk properties. While the process-structure-properties-performance relationships encompass numerous facets and details, the initial work here to build a modeling framework should start relatively simplified due to the computational costs and the complexity of the AM properties [107].

Three case studies, objectives, and proposed approaches are described in detail in chapter 1.3 and will be summarized below:

Feedstock composition variation:

- **Background:** HSLA 115 powder is not commercialized for AM, and the powder vendor composition variation in batches may lead to inferior AM builds. Thus, we must adapt the wrought HSLA composition and ensure it is robust to composition

variation. However, there are millions of composition combinations that need to be studied.

- **Solution:** Build an ICME modeling framework to predict alloy key properties, such as yield strength, DBTT, and printability. Build an ML surrogate model for accelerated high-throughput simulation to guide composition design.
- **Validation:** Print optimized alloy and perform experiments to verify the performance of printed alloys.

Local composition and properties variation:

- **Background:** AM 316L stainless steel shows better mechanical properties than its cast or wrought counterparts. It is hypothesized that TWIP in AM 316L stainless steel is one reason for the excellent mechanical properties, and the segregation in AM prints can lower the SFE and promote the TWIP. Thus, an accurate and fast model is needed to understand the SFE change with segregation.
- **Solution:** It is hypothesized that an ML approach can model the relationship between composition and SFE efficiently and accurately. Thus, SFE data of stainless steel will be collected and a machine learning model will be developed to predict SFE.
- **Validation:** Apply Scheil prediction to simulate the segregation profile for literature-reported AM 316L steel and use the SFE model to calculate the critical twinning stress for the nominal composition and segregation profile to validate if the segregation in AM prints makes the twinning more operatable.

Bulk property variation for the same alloy:

- **Background:** The as-built AM CoCrFeMnNi HEAs show significant variation in yield strength. We need to understand the structural differences resulting from AM and the impact of processing parameters on properties. However, the processing parameters are complex, and the data are very limited for the conventional ML approach.
- **Solution:** It is hypothesized that we can find the critical structure difference between AM and conventional approaches by combining the existing yield strength model for the conventional manufacturing approach and AM experiments data using the Bayesian method. As a result, the Bayesian calibration can be applied to the yield strength model and the differences in dislocation density, grain boundary strengthening, etc., can be determined for different manufacturing approaches. Finally, the correlation analysis will be conducted for studying the impact of processing parameters on the strengthening effects.
- **Validation:** Compare the model-calibrated parameters like dislocation densities with the experimentally measured value reported in the literature. Print FCC alloy, i.e., 316L, with different processing parameters to validate the findings discovered with the Bayesian approach.

In summary, this work is not intended to be a comprehensive and exhaustive framework addressing every challenge in modeling for AM. Instead, it aims to highlight pathways of

combining ICME and data-driven approaches to apply to material feedstock and process design and understand the relationship between process, structure, and property for AM.

2.0 Methods

2.1 Simulation and Modeling

2.1.1 CALPHAD

CALPHAD was first proposed by Kaufman [108]. It can reveal the equilibrium phase information as a temperature, pressure, and composition function. The physical theory behind it is to encode the Gibbs free energy of each phase and find the equilibrium states where the Gibbs free energy of a system reaches the minimum for a given condition. The mathematical equation is $\min\{\sum_\phi f_\phi G_m^\phi\}$ and with the constrain that $\sum_\phi f_\phi = 1$ and $\sum_i f_i x_i^\phi = 1$, where f_ϕ is the molar fraction of phase ϕ, G_m^ϕ is the molar Gibbs free energy of phase ϕ, x_i^ϕ is the atomic fraction of element i in phase ϕ. In terms of the nonequilibrium cases, it is possible to suspend the stable phases and get the metastable phase diagrams.

In this work, the software Thermo-Calc and its high-throughput software development kit (SDK) TC-Python [109,110] will be employed for CALPHAD simulations. Various thermodynamic and kinetic databases available in Thermo-Calc were used based on the alloy composition and availability of the databases when the work was performed.

2.1.2 Physics-based and Phenomenological Models

The physics-based model equation is obtained from the literature, and Python [111] was used to code those equations for simulation. In this work, the physics-based and phenomenological models include yield strength prediction for HSLA and HEA, printability prediction, DBTT prediction, and SFE calculation, where the details are provided in each chapter since the parameter values are different for different alloys.

2.1.3 Data-driven Approach

Hundreds of papers and reports were reviewed to collect the data and build databases for SFE, microstructure, yield strength, manufacturing approaches, and other information on the alloys studied in this work. The statistics of the collected data will be analyzed using Python to explore the relationships between each attribute to gain knowledge of how the composition and treatment process influence the property of interest. The selection of machine learning algorithms and hyper-parameters optimization will be performed based on the performance in cross-validation [112] using Scikit-learn [113] to ensure accuracy and generalizability.

In order to understand how the model works, the SHAP (SHapley Additive exPlanations), which was introduced by Lundberg and Lee [114] based on the cooperative game theory, was applied to calculate the contribution of each input feature to the prediction. This helps us extract helpful information from the model to guide the alloy design. We could also compare the model

with domain knowledge to ensure the model follows the rules that are well-accepted by the material scientist.

The Bayesian and Gaussian model calibration process was performed with OpenTURNS [115] in Python. During the Bayesian calibration, the mean and SD of a parameter are determined based on the literature, and it will be updated with the experiments' measured observations. The Metropolis-Hastings algorithm was used for obtaining the samples during the Bayesian calibration process with a thinning parameter 3, burn-in period of 1000. Finally, the Gaussian approach was used to find the model parameters within the range of Bayesian calibrated parameter ranges where the model outputs will match the experiments' measured yield strength.

2.2 Experiments

2.2.1 Sample Preparation

The optimized HSLA powder for Chapter 3 and the 316L powder for Chapter 5 were printed using laser powder bed fusion with the printer EOS M290 laser sintering machine that is available in Pitt ANSYS Additive Manufacturing Research Laboratory. The processing parameters and the powder composition are listed in each chapter. The necessary heat treatment process will be performed in the box/tube furnace for samples that are encapsulated in vacuumed quartz tubes with back-filled argon gas where the detailed treatment temperature and time can be found in each chapter.

2.2.2 Microstructure Characterization

The printed samples were ground using SiC emery paper with grit ranges from 400 to 1200, followed by polishing with diamond and Al_2O_3 suspensions containing particles. The cracks and porosity were checked by using a Zeiss Sigma 500 VP scanning electron microscope (SEM) and Zeiss Axio A1 optical microscope.

For the 316L, the X-ray diffractograms (XRD) were obtained using a Bruker D8 Discover X-ray Diffractometer (Bruker Corporation, USA) using a Cu-K_α radiation. The measurements were taken in the 2θ range of 20–95° with 0.02° as the step size, and with 0.05 seconds as time per step.

2.2.3 Property Test

For the measurement of AM HSLA steel yield strength, the uniaxial tensile test was performed on the dog-bone plate type sample using the MTS880 universal testing machine together with a 25 mm gauge length extensometer. The sample dimension follows ASTM-E8/E8M [116] standard.

For the measurement of the ductile to brittle transition temperature of HSLA steel, the Charpy V-notch test was conducted using the Tinius Olsen high energy impact tester. To perform the low temperature measurement at -20 and -40°C, the testing bars were immersed in liquid nitrogen and cooled until the temperature reached the target temperature, which was monitored using an infrared thermometer.

For the measurement of the hardness of 316L stainless steel, the Leco LM-800 tester with 300g load and 10d dwell time was used. The test repeats 16 times, and the average and SD will be calculated. In order to eliminate the obvious interference of the pores, the indents that hit a pore will be removed.

3.0 HSLA-115 Steel Composition Uncertainty Quantification and Optimization Using ICME and Surrogate ML Model

This chapter is modified from the publication: Wang, Xin, and Wei Xiong. "Uncertainty quantification and composition optimization for alloy additive manufacturing through a CALPHAD-based ICME framework." npj Computational Materials 6.1 (2020): 1-11. https://doi.org/10.1038/s41524-020-00454-9, Under the CC BY 4.0 license.

3.1 System Design Chart of HSLA-115 Steel

In order to establish the model framework for HSLA-115 Steel, we have to understand the process-structure-property relationships, summarized in the systems design chart, as shown in Fig. 3-1. The systems design chart exhibits how hierarchical structural features contribute to the mechanical properties and how the structure evolves during different processes and compositions [79,117]. Each line connecting the process, structure, and property indicates a relationship/model between these attributes. HSLA steel has a combination of high strength and good low-temperature impact toughness. This is achieved through hot isostatic pressing (HIP)/austenitization, quenching, and tempering that leads to a dense part with a fine martensite/bainite matrix and dispersed nano-sized Cu and M_2C precipitates. HIP aims to reduce the porosity of as-built components for improved mechanical properties and corrosion resistance [118]. In dense builds, austenitization helps achieve a homogenized austenitic structure by dissolving undesirable phases and eliminating

segregation due to rapid solidification. During post-heat treatment, it is expected that enough undissolved MX particles (mainly the NbC) exist to pin the grain boundaries and prevent excessive grain growth. Water quenching is applied to form a fine lath bainitic/martensitic structure that improves the strength. Lastly, the tempered martensite formed after tempering enhances the impact toughness by reducing dislocation density. More importantly, the coherent Cu (3-5 nm in radius) and M_2C (1.5-3 nm in radius) will precipitate during tempering, causing a significant hardening effect [119,120]. The precipitation of M_2C will dissolve the cementite and avoid the decrease in impact toughness due to the formation of coarse cementite. Other precipitates, such as $M_{23}C_6$, may also form while they usually have large sizes and contribute negligible strengthening effects [121]. Finally, the excellent weldability of this steel originates from the low carbon content and other alloying elements.

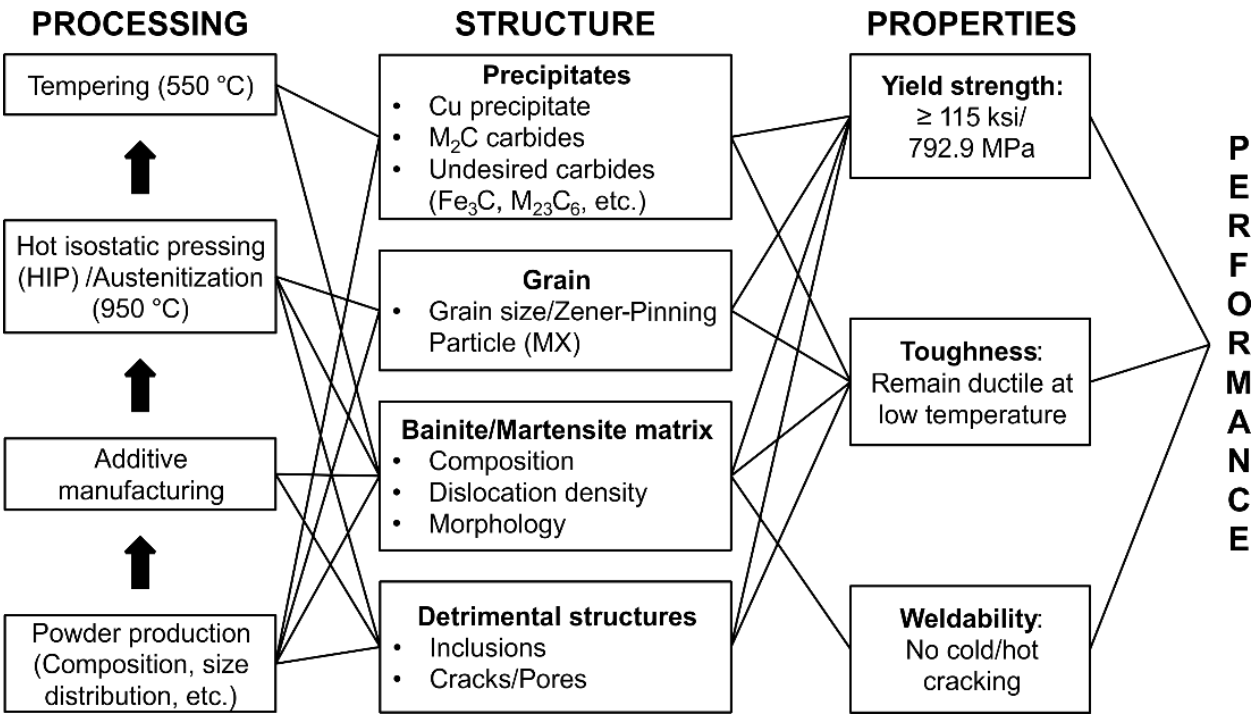

Figure 3-1 Systems design chart for AM HSLA-115.

3.2 ICME Framework

Based on the systems design chart, this work established an ICME modeling framework to evaluate the yield strength, weldability/printability, and impact transition temperature of HSLA steels. As illustrated in Fig. 3-2, the composition and processing parameters were taken as inputs for the decision tree model, CALPHAD-based thermodynamic model, and Graville diagram [77]. The outputs from these models, such as the dislocation density, matrix composition, and so on, were coupled with the physics-based strengthening, ITT, and weldability evaluation models to calculate the yield strength, ITT, and weldability that includes the freezing range and Graville diagram index for each composition. Finally, the calculated properties for each composition were used to find the optimized composition for AM that will give the highest chance of a successful build that meets all property requirements. The explicit description of models, the screening, and the analysis process will be given in the following context.

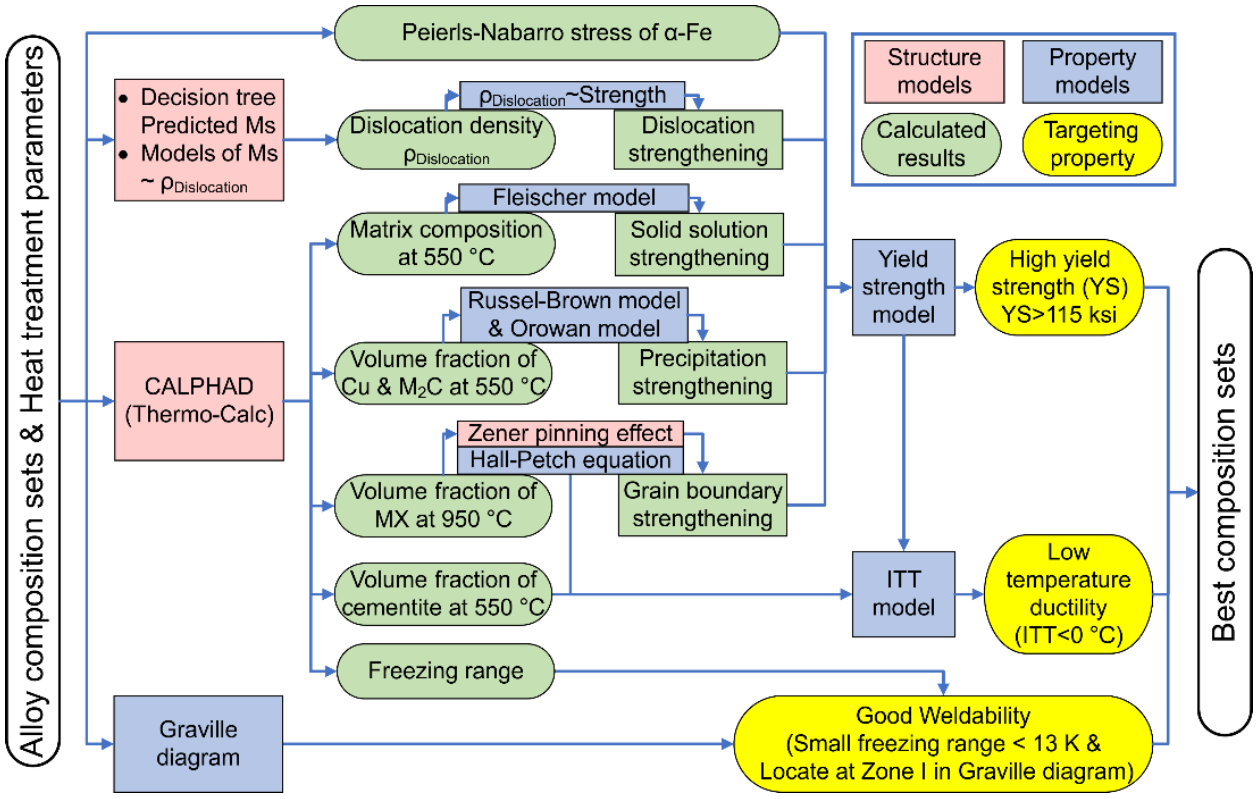

Figure 3-2 ICME modeling workflow for HSLA-115 steel composition design. The pink box denotes structure models predicting features such as phase fraction of different phases and dislocation density based on composition and heat treatment process; the blue box denotes the property models which can simulate the strength, freezing range, etc., based on structure and compositions; the green box denotes the calculated property or structural information from the models; the yellow box denotes the target properties.

As illustrated in Fig. 3-2, the alloy yield strength, σ_Y [79], arises from the combined strengthening effects of Peierls-Nabarro (P-N) stress σ_0, dislocation strengthening σ_d, solid solution strengthening σ_{ss}, precipitation strengthening σ_{ppt}, and grain boundary strengthening $\sigma_{H\text{-}P}$:

$$\sigma_Y = \sigma_0 + \sigma_d + \sigma_{H-P} + \sigma_{ppt} + \sigma_{ss} \quad (3\text{-}1)$$

Where σ_0 = 50 MPa is the P-N stress of α-Fe [75], the details of calculation for other strengthening effects are given below.

The martensitic/bainitic structure in the HSLA-115 steel, with high dislocation density, forms due to rapid cooling. Takahashi and Bhadeshia [73] proposed a phenomenological equation to describe the relationship between the M_S temperature, dislocation density, and the strengthening effect from dislocations in the as-quenched steel σ_{DS}^0) [73,80]:

$$\sigma_{DS}^0 = M\tau_{DS}^0 = 0.38MGb\sqrt{\rho} \quad (3\text{-}2)$$

$$\log(\rho) = 9.2848 + 6880.73/T - 1780360/T^2 \quad (3\text{-}3)$$

Where temperature T is max(570 K, M_S), and M is the Taylor orientation factor to convert the shear stress to normal stress, which ranges from 2.6 to 3.06 in bcc materials, and M is 2.75 in this study [122], G = 80 GPa is the shear modulus [123], b = 0.25 nm is the Burgers vector in α-Fe [124], ρ is the dislocation density. The M_S temperature can be either predicted using theoretical modeling or determined using experiments such as dilatometry. This work uses a data-mining generated decision tree model [78] to predict M_S temperature. The dislocation density will decrease during the tempering heat treatment, and it is related to the ratio of the precipitate fraction formed during the heat treatment process to the equilibrium value f_{ppt} [125]:

$$\sigma_{DS} = M\tau_{DS} = M(\tau_{DS}^0 - \sqrt{0.8}\tau_{DS}^0 f_{ppt}) \quad (3\text{-}4)$$

Since the precipitate fraction does not increase significantly after enough aging time [119,126], it is assumed that the ratio f_{ppt} is 1 after tempering.

The contribution from solid solution strengthening arises from the size and elastic modulus misfit between the solvent and the solute atoms. Fleischer's equation [85] is adopted to evaluate the strengthening effects in multicomponent solid solutions [127]:

$$\sigma_{ss} = \left[\sum_i {\beta_{ss,i}}^2 c_i\right]^{0.5}, i = \text{Ni, Mn, Cr, Al, Mo, Cu} \quad (3\text{-}5)$$

where $k_{ss,Ni}$=708 MPa atomic fraction^{-1} (MPa at^{-1}), $k_{ss,Mn}$=540 MPa at^{-1}, $k_{ss,Cr}$=622 MPa at^{-1}, $k_{ss,Al}$=196 MPa at^{-1}, $k_{ss,Mo}$=2362 MPa at^{-1}, $k_{ss,Cu}$=320 MPa at^{-1}are the strengthening coefficients [86], and c_i is the atomic fraction of the strengthening element in the matrix at the tempering temperature obtained using the CALPHAD method.

The most critical strengthening mechanism in HSLA-115 steel is the precipitation hardening due to Cu and M_2C precipitates at the tempering temperature (550°C). For predicting the strengthening effect of Cu precipitates, the Russel-Brown model is valid [83,128]. This model is based on the interaction between the dislocations and Cu precipitates, which originates from the difference in elastic modulus between the matrix and precipitates [83], and it can be calculated using the equations 3-6 and 3-7:

$$\sigma_{Cu} = 0.8M\frac{Gb}{L_{Cu}}[1-(\frac{E_p}{E_m})^2]^{\frac{1}{2}};\ \sin^{-1}\left(\frac{E_p}{E_m}\right) \leq 50° \quad (3\text{-}6)$$

$$\sigma_{Cu} = M\frac{Gb}{L_{Cu}}[1-(\frac{E_p}{E_m})^2]^{\frac{3}{4}};\ \sin^{-1}\left(\frac{E_p}{E_m}\right) \geq 50° \quad (3\text{-}7)$$

Where E_p and E_m are the dislocation line energy in the Cu precipitates and the matrix, respectively. L_{Cu} is the mean planar spacing of Cu precipitates, and $L_{Cu}^{-1} = f_{Cu}^{\frac{1}{2}}/1.77r_{Cu}$, f_{Cu} is the volume fraction of Cu precipitates, and r_{Cu} is the mean radius of the Cu precipitates. The f_{Cu} is calculated using the Thermo-Calc software with the TCFE9 database. In order to simplify the model, we assume that the r_{Cu} is 4 nm since the radius of the Cu-rich precipitate in aged HSLA alloy is usually 3-5 nm [121,126,129]. The E_p/E_m ratio can be calculated with the following equations:

$$\frac{E_{\mathrm{p}}}{E_{\mathrm{m}}} = \frac{E_{\mathrm{P}}^{\infty} \log \frac{r}{r_{\mathrm{o}}}}{E_{\mathrm{m}}^{\infty} \log \frac{R}{r_{\mathrm{o}}}} + \frac{\log \frac{R}{r}}{\log \frac{R}{r_{\mathrm{o}}}} \tag{3-8}$$

Where E_{p}^{∞} and E_{m}^{∞} denote the energy per unit length of dislocation in an infinite medium, and their ratio is 0.62, $R = 1000r_0$ is the outer cut-off radius, $r_0 = 2.5b$ is the inner cut-off radius or dislocation core radius [128].

The strengthening mechanism of M_2C precipitates in HSLA steels or similar alloys should follow the Orowan-Ashby dislocation strengthening effect, provided the precipitate size is larger than 1.1 nm [84]. For HSLA steel aged at 550°C, the mean radius of M_2C precipitate r_{M2C} is usually less than 2.5 nm [119,126], and it is assumed that $r_{\mathrm{M2C}} = 2$ nm in this work. The Orowan equation can be written in the following format [130]:

$$\sigma_{\mathrm{M2C}} = MY \frac{G}{4\pi(1-v)^{0.5}} \frac{2b}{\omega_{\mathrm{L}} r_{\mathrm{M2C}}} \ln\left(\frac{2\omega_{\mathrm{D}} r_{\mathrm{M2C}}}{b}\right) \sqrt{\frac{\ln\left(\frac{2\omega_{\mathrm{D}} r_{\mathrm{M2C}}}{b}\right)}{\ln\left(\frac{\omega_{\mathrm{L}} r_{\mathrm{M2C}}}{b}\right)}} \tag{3-9}$$

$$\omega_{\mathrm{L}} = \left(\frac{\pi\omega_{\mathrm{q}}}{f_{\mathrm{M2C}}}\right)^{0.5} - 2\omega_{\mathrm{r}} \tag{3-10}$$

$$\frac{1}{\omega_{\mathrm{D}}} = \frac{1}{\omega_{\mathrm{L}}} + \frac{1}{2\omega_{\mathrm{r}}} \tag{3-11}$$

Where $v = 0.3$ is the Poisson's ratio, $Y = 0.85$ is the M_2C spatial-distribution parameter for Orowan dislocation looping, f_{M2C} is the volume fraction of M_2C, ω_{r} is the constant to convert the mean particle radius of M_2C to the effective radius that intersects with the glide plane, and ω_{q} establishes the relationship between the mean area of precipitate intersecting with the glide plane. A detailed discussion about ω_{r}, ω_{q}, and Y can be found in Ref. [119].

The following equation is used to evaluate the overall strengthening due to precipitation with two different sets of precipitates:

$$\sigma_{\mathrm{ppt}} = (\sigma_{\mathrm{Cu}}^{k} + \sigma_{\mathrm{M2C}}^{k})^{\frac{1}{k}} \tag{3-12}$$

Where k = 1.71 is the superposition exponent to superpose the strengthening effects of two different strengthening particles [84].

The strengthening effect due to the grain size refinement can be estimated using the Hall-Petch equation [81,82]:

$$\sigma_{\mathrm{H-P}} = \frac{k_{\mathrm{y}}}{\sqrt{d_{\mathrm{packet}}}} \tag{3-13}$$

Where k_{y} = 600 MPa $\mu m^{-0.5}$ is the Hall-Petch coefficient [131], d_{packet} is the size of the martensite packet or bainite, which is closely related to the size of prior austenite D_{g} [75]. In lower bainite/martensite matrix materials, the martensite block size will be even smaller [132,133]. As a result, we assume the grain size relationship is similar in martensitic steel, which can be written in the form of the following equation [75]:

$$d_{\mathrm{packet}} = 0.40 D_{\mathrm{g}} \tag{3-14}$$

The NbC phase in HSLA steels remains undissolved at the austenitization temperature (950°C), which can pin the austenite grain boundary to prevent excessive grain growth. The maximum austenite grain size after austenitization is a function of the size and volume fraction of pinning particles [74]:

$$D_{\mathrm{g}} = \begin{cases} 8r_{\mathrm{MX}}/\left(9{f_{\mathrm{MX}}}^{0.93}\right), & f_{\mathrm{MX}} < 0.1 \\ 3.6r_{\mathrm{MX}}/\left({f_{\mathrm{MX}}}^{0.33}\right), & f_{\mathrm{MX}} > 0.1 \end{cases} \tag{3-15}$$

Where r_{MX} is the average radius of the MX (M = Nb, X = C, N) in HSLA steels, and it is reported to be around 13 nm in different HSLA steels with various compositions and heat treatment parameters [134,135], f_{MX} is the volume fraction of MX at austenitization temperature (e.g., 950°C) which can be obtained using the Thermo-Calc software with TCFE9 database.

As shown in Fig. 3-2, the ITT is used as an evaluation criterion for the low-temperature ductility. The ITT corresponds to the ductile-brittle transition temperature (DBTT) or fracture appearance transition temperature (FATT), which are close to each other. The material is ductile at a temperature above the ITT; otherwise, it is brittle. The phenomenological equation to calculate 50% ITT [76] (˚C) for the ferritic-pearlitic steels after the calibration with reported HSLA ITT [136] is given below:

$$50\%\ \text{FATT} = 112t^{0.5} - 13.7d^{-0.5} + 0.43\Delta y - 54 \qquad (3\text{-}16)$$

Where t is the cementite thickness in μm, d is the grain size in mm, Δy is the strength contributed from the precipitation hardening in MPa that can be obtained through the precipitation strengthening model and Zener pinning effect as shown in Fig. 3-2. However, this model should be used with low confidence because it was initially designed for ferritic-pearlitic steels, and it is reported that the error from this model can be up to 34 K [137]. Thus, the ITT criterion for this design to select a composition with good ductility at low temperature is set to 0 °C to avoid over-filtering.

The chemical composition determines the weldability by influencing the hardenability and phase transformations during welding. Carbon plays a crucial role in weldability and has two major effects. Firstly, high carbon content leads to carbide precipitation during the AM process and increases the freezing range (the difference between the liquidus and solidus temperatures), which

may initiate cracking through hot tearing effects [138]. Secondly, it causes an increase in hardenability and thus lowers ductility [139]. The low carbon content of HSLA steel makes it a suitable candidate material for additive manufacturing. This study evaluates the ability to avoid hot and cold cracking for different compositions by calculating the freezing range and location in the Graville diagram [77], as shown in Fig. 3-2.

Hot cracking occurs near the solidus temperature where the liquid exists. A reduced freezing range is desirable to avoid hot cracking during additive manufacturing [140,141]. In this study, the freezing range is $T_{80\%\text{liquid}} - T_{20\%\text{liquid}}$ (the difference between temperatures with 80% and 20% liquid), and the equilibrium freezing range is calculated based on the TCFE9 database of the Thermo-Calc software. The allowable maximum freezing range for compositions with good weldability is set to be 13 K.

Cold cracking occurs when the weld has cooled down to room temperature, which is also called hydrogen-induced cracking (HIC). As a phenomenological method, the Graville diagram is very useful in determining the ability to avoid HIC [77]. If the alloy composition locates in Zone I of the Graville diagram, cold cracking only occurs when the hydrogen content is very high and weldability is good. In contrast, compositions in Zone II or Zone III have a medium or high susceptibility to HIC, respectively [142], and the details of the Zone in the Graville diagram and the location of different steels are illustrated by Caron, J [142]. An alloy with good weldability should satisfy the following equation to avoid cold cracking:

$$0 \leq -0.0515 \cdot \mathrm{CE} + 0.127 - \mathrm{C} \qquad (3\text{-}17)$$

Where C is the carbon content of steel in weight percent, CE = C + (Mn+Si)/6 + (Ni+Cu)/15 + (Cr+Mo+V)/5 is the carbon equivalent (CE) of the steel in wt.%.

3.3 Screening Strategy for Reliability Design

For the reliability design, the goal is to avoid failure build. As a result, finding the best composition range for each element will be needed to lead to a successful build. The initial composition and screening ranges listed in Table 3-1 are employed for high-throughput calculations. The screening range spans a broader composition space in comparison with the initial composition range provided by the vendor. The screening composition range was determined to ensure that in the screening range, the percent of compositions meeting all property requirements exhibit a peak or plateau for each composition screening range so that we do not miss the possible optimized composition space. Since there are nine elements whose composition needs to be optimized, it implies that nine variables with a certain range need to be considered in the mathematical space for sampling. The sampling space will have an exponential increase associated with a broad composition range for each element and thus require a huge sampling size to ensure that the analysis is based on enough calculations. For example, suppose we discover the optimized composition for all components in the screening range that we defined at one time, it is found that such a multi-dimensional composition space is $1.7x10^6$ times larger than the initial composition space, and $1.7x10^6$ is the product of the ratios listed in Table 3-1. As a result, it is challenging to screen enough compositions to represent the whole screening space. As a mitigation method to reduce the computational load, we optimized the composition for each element one by one. Take carbon as an example, and we sampled 50,000 compositions from the screening range of carbon and the initial composition range for the rest of the elements using the Latin hypercube sampling approach [143] with a random uniform distribution. The same procedure was repeated for all

elements; finally, 450, 000 compositions were sampled. This method requires much fewer calculations during the screening process while still effectively cover the required composition space for discovering the optimized composition. The yield strength, ITT, and weldability of these samples were calculated with the ICME framework to identify the influence of each element on the microstructure-property relationship. During the optimization process, we utilized nine cores and finished the simulation in less than two days, which proves that the efficiency of this computational framework is high. Further, the composition was optimized such that it maximized the possibility of a successful build, which could satisfy all the requirements for yield strength, weldability, and low-temperature ductility after post-heat treatment.

Table 3-1 The initial composition range (wt.%), screening range (wt.%), and their ratio for different elements in the manufactured AM powder for HSLA-115 steel

	Fe	C	Cr	Cu	Mn	Nb	Mo	Ni	Si	Al
Initial composition range	Bal.	0.053 ± 0.025	0.66 ± 0.10	1.27 ± 0.15	0.98 ± 0.20	0.03 ± 0.01	0.57 ± 0.10	3.43 ± 0.20	0.225 ± 0.125	0.03 ± 0.01
Screening composition range	Bal.	0.06 ± 0.04	0.6 ± 0.5	1.25 ± 0.45	1.15 ± 0.95	0.055 ± 0.045	0.7 ± 0.5	3.5 ± 1.5	0.25 ± 0.25	0.055 ± 0.045
Ratio (Screening range/ Initial composition range)		1.6	5	3	4.75	4.5	5	7.5	2	4.5

Once the optimized composition was determined, 50,000 compositions within the uncertainty range of the initial nominal composition and the optimized nominal composition were sampled using the Latin hypercube sampling approach following a random uniform distribution, respectively. Later, the probability analysis on successful additive manufacturing was performed, and the improvement in the optimized composition compared with the initial composition was evaluated.

3.4 Results of Reliability Design

Figure 3-3 shows the model predicted yield strength against the experimental measurements for several HSLA steels [119,129,144] with different compositions and tempering temperature ranges from 450 to 650 °C (For alloys heat treated with the same temperature and different times, the closest value to prediction was chosen in Fig. 3-3). The ICME model prediction and experimental results show a good agreement. These results indicate that the strengthening model within the ICME framework can predict the yield strength of HSLA steels.

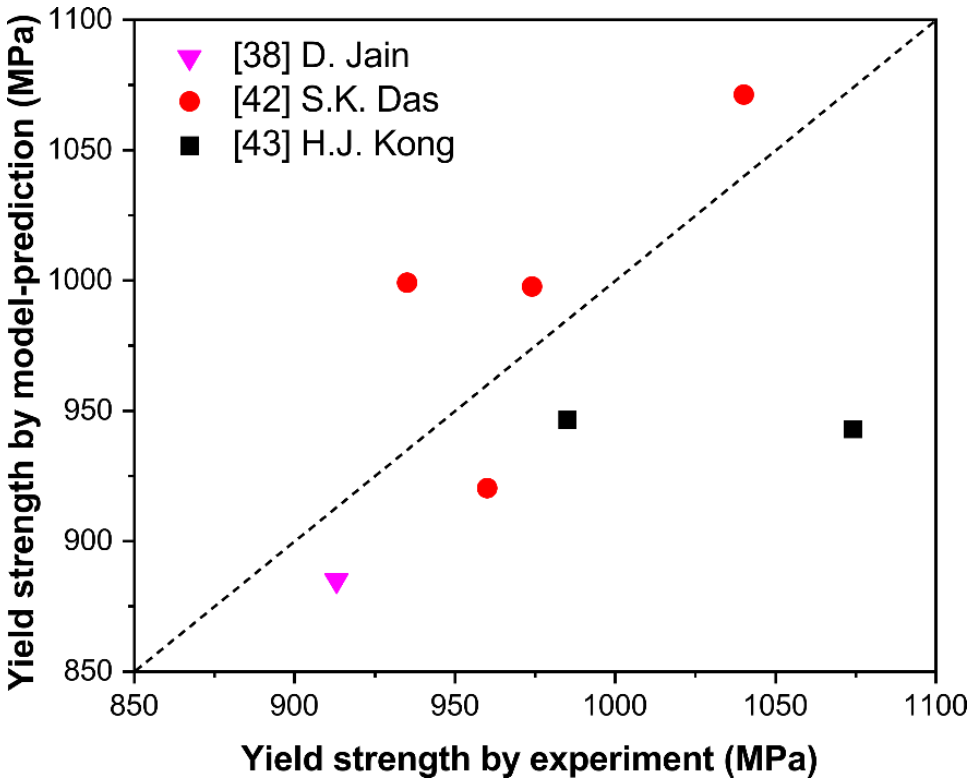

Figure 3-3 Comparison of the yield strength by model prediction and the experiments. The model-predicted value is equal to the experimental value if the symbol is located on the dashed diagonal line.

Figure 3-4 shows the variation of all properties as a function of carbon content. The same procedure is also applied to other elements. It allows us to assess the influence of each element on the strength, low-temperature ductility, and weldability. Each column represents the model prediction for one set of compositions with the same range of carbon content, i.e., 0.0025 wt.% carbon. The number under each bin corresponds to the smallest carbon content in the bin. For example, bin 0.05 contains all compositions that have a carbon content between 0.05 and 0.0525, i.e., [0.050, 0.0525) and other elements in their initial composition range, which is listed in Table 3-1. Evidently, with the increase in carbon content, the yield strength, as shown in Fig. 3-4(a), initially increases and then decreases, which is different from Saha's [145] work on the high-strength steels that the strength will continuously increase with the addition of carbon content. The contradiction is from the incorrect assumption in Saha's work that carbon only forms the M_2C. However, carbon will also dissolve in the martensite matrix and form other carbides. Furthermore, the fraction of M_2C will change with different compositions. Based on our calculation (Fig. 3-5), when the carbon increases, the fraction of M_2C will increase first and then decrease. Moreover, even if the carbon content is similar, the fraction of M_2C will also change with different alloying elements. For low-temperature ductility, as the carbon content increases, the ITT increases and then decreases (see Fig. 3-4(b)), indicating a worsening of low-temperature ductility at the first stage and improvement in the later stage. Further, as more carbon is added to an alloy, the freezing range increases, as shown in Fig. 3-4(c), which indicates a higher probability of hot cracking. Similarly, the location of the composition in the Graville diagram will move out of Zone I when the carbon content is around 0.085 wt.% and the susceptibility to cold cracks increases (Fig. 3-

4(d)). These results are consistent with the expected influence of carbon content on the weldability of HSLA steels.

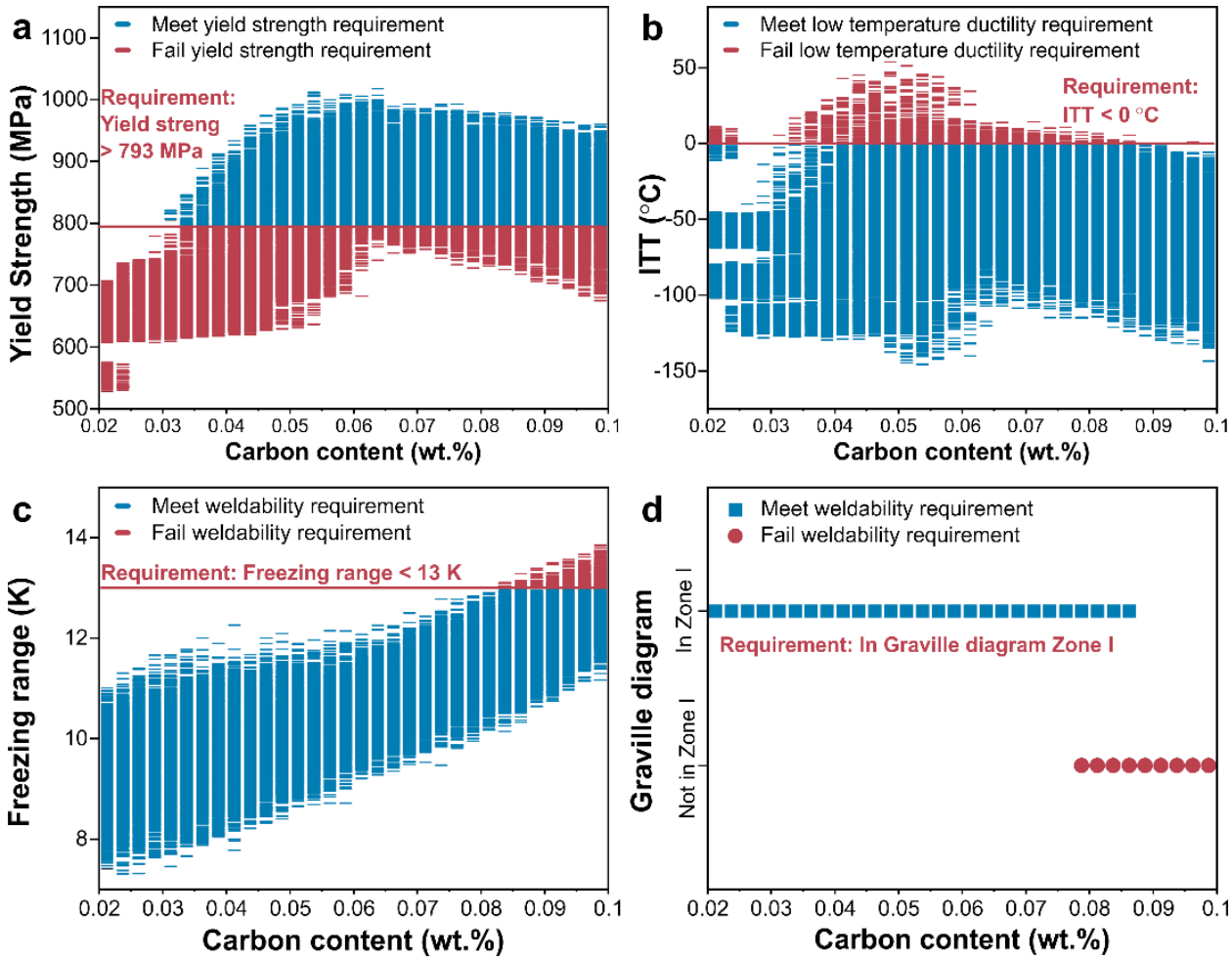

Figure 3-4 Variation in properties due to the change in carbon content. Trend analysis on (a) yield strength, (b) ITT, (c) freezing range, and (d) Graville diagram location. The compositions that meet the requirements are in blue. The compositions that failed the property requirements are in red.

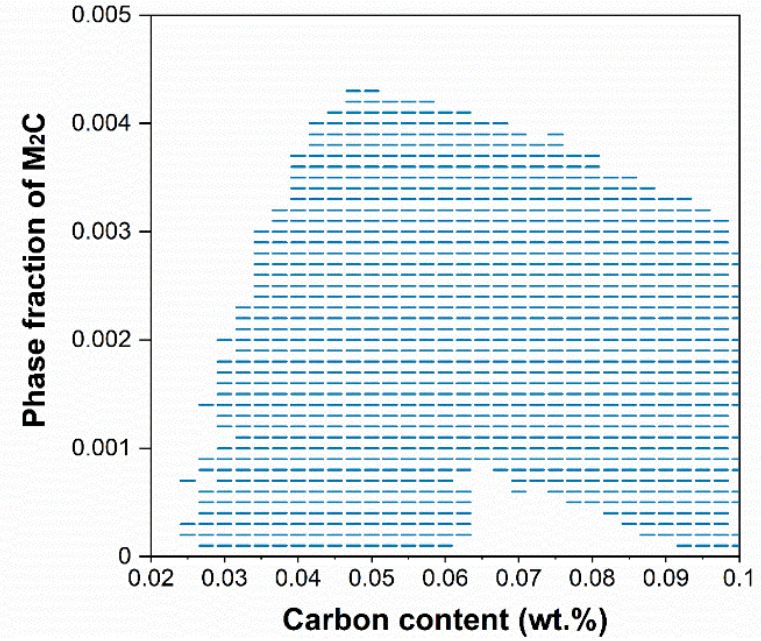

Figure 3-5 Change of M_2C fraction with different carbon content. The carbon content is within the screening range, and different other elements are within their initial composition range

The influence of carbon content on the yield strength and different hardening effects are shown in Fig. 3-6(a). The increase in carbon content leads to increased strengthening effects from grain boundaries and dislocations since carbon introduces the formation of Zener pinning particle NbC and promotes higher dislocation density after quenching. However, the strength achieved from the precipitation hardening increases initially and then decreases, which results in a peak hardening with the carbon content between 0.06-0.065 wt.%. Precipitation hardening is critical and depends on the formation of nano-size M_2C and Cu particles in the HSLA-115 steel. According to Fig. 3-6(b), the addition of carbon has no apparent influence on Cu precipitation, while it has a significant impact on the precipitation of M_2C.

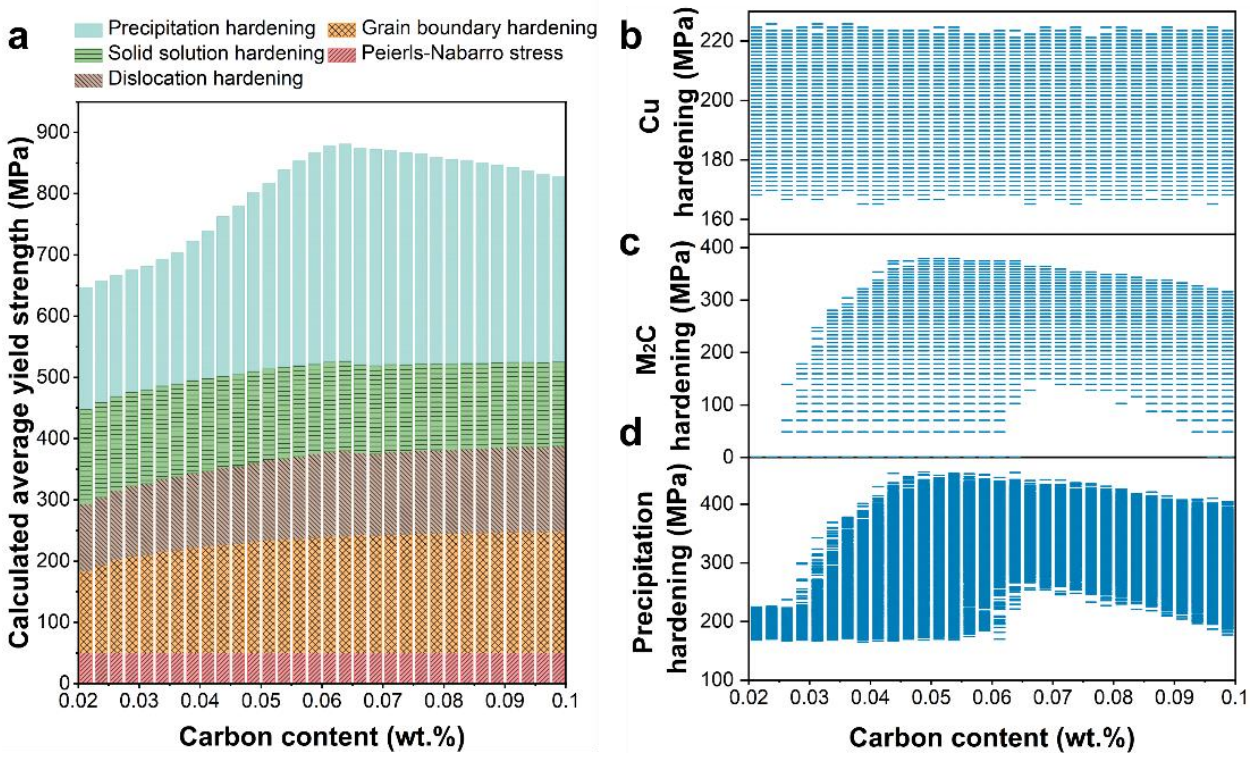

Figure 3-6 Predicted yield strength and the contribution from different strengthening mechanisms versus carbon content. (a) Average strength from different strengthening effects versus carbon content, precipitation strengthening effect from (b) Cu precipitation, (c) M_2C precipitation, and (d) sum of Cu and M2C precipitates.

Figure 3-7 provides an overview of the qualified composition range with all the considered properties as the selection criterion. In such a histogram, the composition sets of every single bin are categorized into different groups based on the number and type of criterion the composition meets. The percentage of compositions in the group with no pattern and in pink (compositions meeting all property requirements) continues to increase with the increase in carbon content, displaying a maximum at 0.06 wt.% carbon, which is higher than the initial nominal composition 0.053 wt.% carbon that is determined based on the cast HSLA steel. However, when the carbon

content is higher than 0.085 wt.%, only a few compositions can satisfy the weldability requirement. Since the uncertainty in carbon content is ± 0.025 wt.%, it is better to avoid the targeted average carbon content higher than 0.0575 wt.%. The insufficient strength in this composition range can be made up by tuning the composition of other elements to increase the hardening effects.

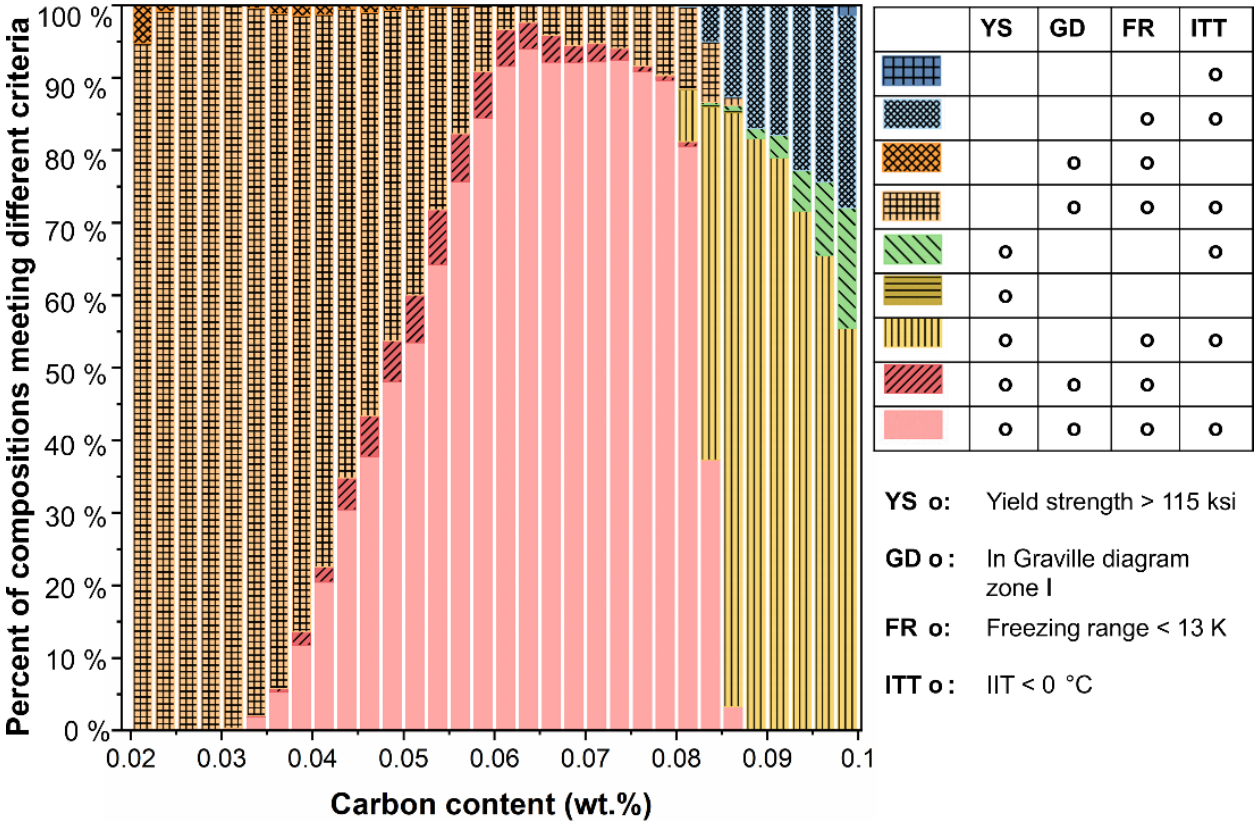

Figure 3-7 Optimization of carbon content by visualizing the percentages of compositions meeting different criteria. Pink color without pattern filling: The percentage of compositions with yield strength higher than 115 ksi, good weldability, and ITT lower than 0 K. The meaning of other color and pattern-filled bars can be understood in a similar way based on the table in the figure, and groups smaller than 0.1 % are not listed for better illustration.

Other elements were screened and analyzed using the same method implemented for carbon. In total, 450,000 compositions sampled using the strategy mentioned in the method section were calculated and analyzed. Table 3-2 summarizes the elemental influence on the structure and strengthening effects within the composition range listed in Table 3-1. For each screening range, the arrow ↑ means the increase in the component is beneficial to the property; the arrow ↓ means the increase in the component is detrimental to the property; the symbol O means the increase in the component has no obvious effect on the property; ↑↓means the increase in the component is beneficial to the property first, and then detrimental to the property; ↓↑means the increase in the component is detrimental to the property first, and then beneficial to the property. For instance, the weldability decreases when molybdenum increases from 0.2 to 1.2 wt.%. While the yield strength increases at first due to the improvement in precipitation hardening from M_2C particles, solid solution strengthening, and dislocation hardening effects, and then decreases due to the reduction in the phase fraction of M_2C when Mo reaches a threshold value. The low-temperature ductility will first decrease and then increase. The influences of other elements can be explained based on Table 3-2 and following the same method.

Table 3-2 Summary of the influence of elements in HSLA-115 on the key properties

	C	Cr	Cu	Mn	Nb	Mo	Ni	Si	Al
Resistance to cold cracking	↓	↓	O	↓	O	↓	↓	O	O
Resistance to hot cracking	↓	O	O	↓	↓	↓	↑	↓	↓
Ductility at low temperature	↓↑	↓↑	↓	↑	↑	↓↑	O	↑	O
Yield strength	↑↓	↑↓	↑	↓	↑	↑↓	O	↓	O
Cu hardening	O	O	↑	↓	O	O	↓	↑	O
M_2C hardening	↑↓	↑↓	O	O	↓	↑↓	O	↓	O
Solid solution hardening	↓	↑	O	↓	↑	↑	↑	O	O
Dislocation hardening	↑	↑	O	↑	O	↑	↑	O	O
Grain boundary hardening	↑	O	O	O	↑	O	O	O	O

Table 3-3 lists the initial and optimized composition in wt.%. Compared with the initial composition, the contents of C, Cu, and Mo have increased to ensure that the yield strength is higher than 115 ksi (793 MPa). In contrast, the contents of Cr, Mn, and Si have decreased to balance the deterioration of weldability. The Nb content is increased to introduce a higher phase fraction of MX during the austenitization process to effectively avoid excessive grain growth, improve the low-temperature ductility, and increase the strength. Elements such as Mo, Ni, and Al do not change since their initial content is sufficient for the required properties, or they do not have a pronounced influence on critical properties.

Table 3-3 Comparison of initial composition and optimized composition (wt.%)

Element	Fe	C	Cr	Cu	Mn	Nb	Mo	Ni	Si	Al
Initial composition	Bal.	0.053 ± 0.025	0.66 ± 0.1	1.27 ± 0.15	0.98 ± 0.2	0.03 ± 0.01	0.57 ± 0.1	3.43 ± 0.2	0.225 ± 0.125	0.03 ± 0.01
Optimized composition	Bal.	0.057 ± 0.025	0.525 ± 0.1	1.55 ± 0.15	0.5 ± 0.2	0.08 ± 0.01	0.57 ± 0.1	3.43 ± 0.2	0.125 ± 0.125	0.03 ± 0.01

In comparison with the calculated properties of the initial and optimized nominal composition (Table 3-4), it is evident that the optimized one has much higher yield strength and lower ITT from model prediction. This indicates that by slightly tuning the initial composition, HSLA steel could achieve a higher strength while remaining ductile at low temperatures. For example, less $M_{23}C_6$ and more M_2C precipitates form at the tempering temperature with the optimized composition, as shown in Fig. 3-8. Also, a higher fraction of NbC remains stable at high temperature and hence, retard the grain growth and coarsening. Importantly, the optimized alloy has achieved a small freezing range, and it is in Zone I of the Graville diagram. This indicates that

the printability for AM of alloy with initial composition is similar to the one after composition optimization.

Table 3-4 Comparison of model-predicted key properties of the initial and optimized nominal compositions

Calculated properties	Yield strength	ITT	Freezing range	Graville diagram
Initial composition	873 MPa	-15°C	10.10 K	Zone I
Optimized composition	1076 MPa	-100°C	10.24 K	Zone I

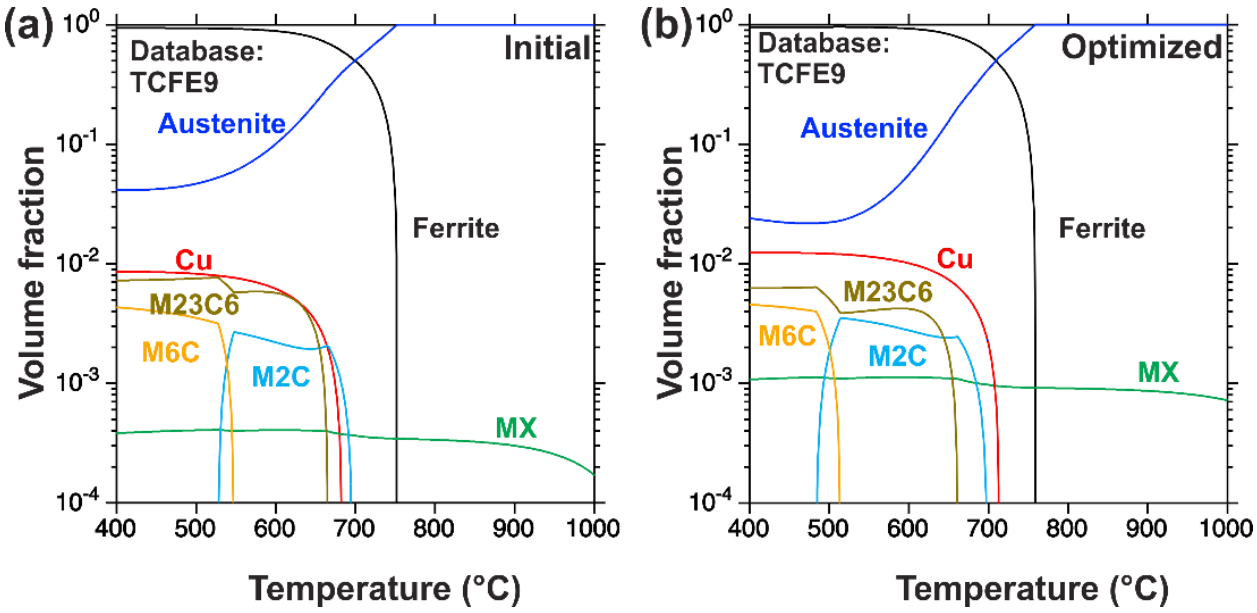

Figure 3-8 Equilibrium phase fraction plots as a function of temperature. Diagrams of (a) initial and (b) optimized compositions calculated using the TCFE9 database.

To further verify the improvement after optimization in terms of the composition uncertainty, 50,000 compositions were randomly sampled from the initial and optimized composition spaces listed in Table 3-3, respectively. The yield strength, ITT, freezing range, and

Graville diagram location were calculated for each data point. The same criteria listed in the previous sections were used to evaluate whether the composition meets the property requirements.

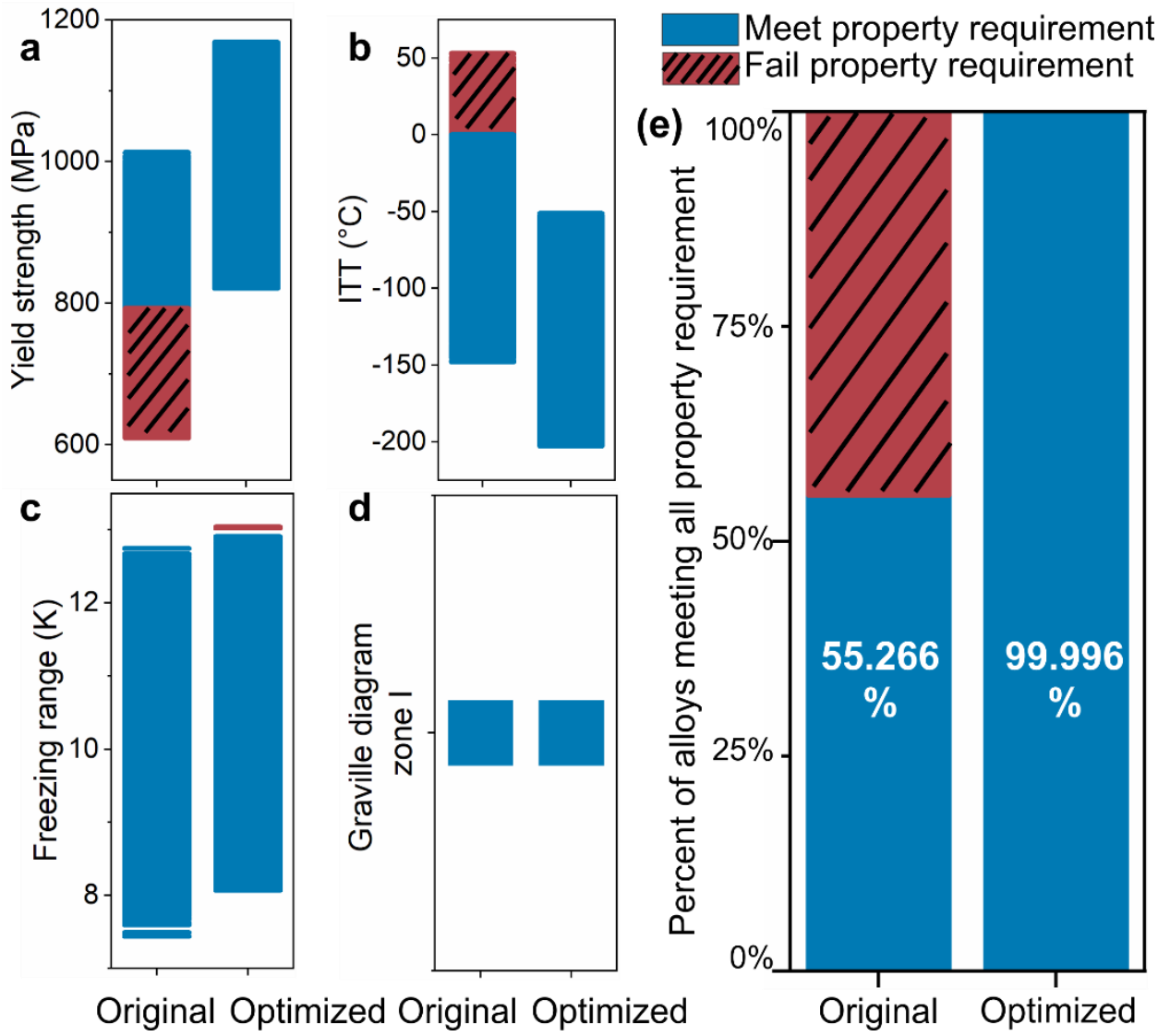

Figure 3-9 Distribution of calculated key properties of initial and optimized composition within their uncertainty range. (a) yield strength, (b) ITT, (c) freezing range, and (d) location at the Graville diagram. (e) Percentage of alloys meeting the criteria of initial composition and optimized composition. The ones that meet all requirements are in blue without a stripe pattern. The ones that failed to match the requirement are in red with a stripe pattern.

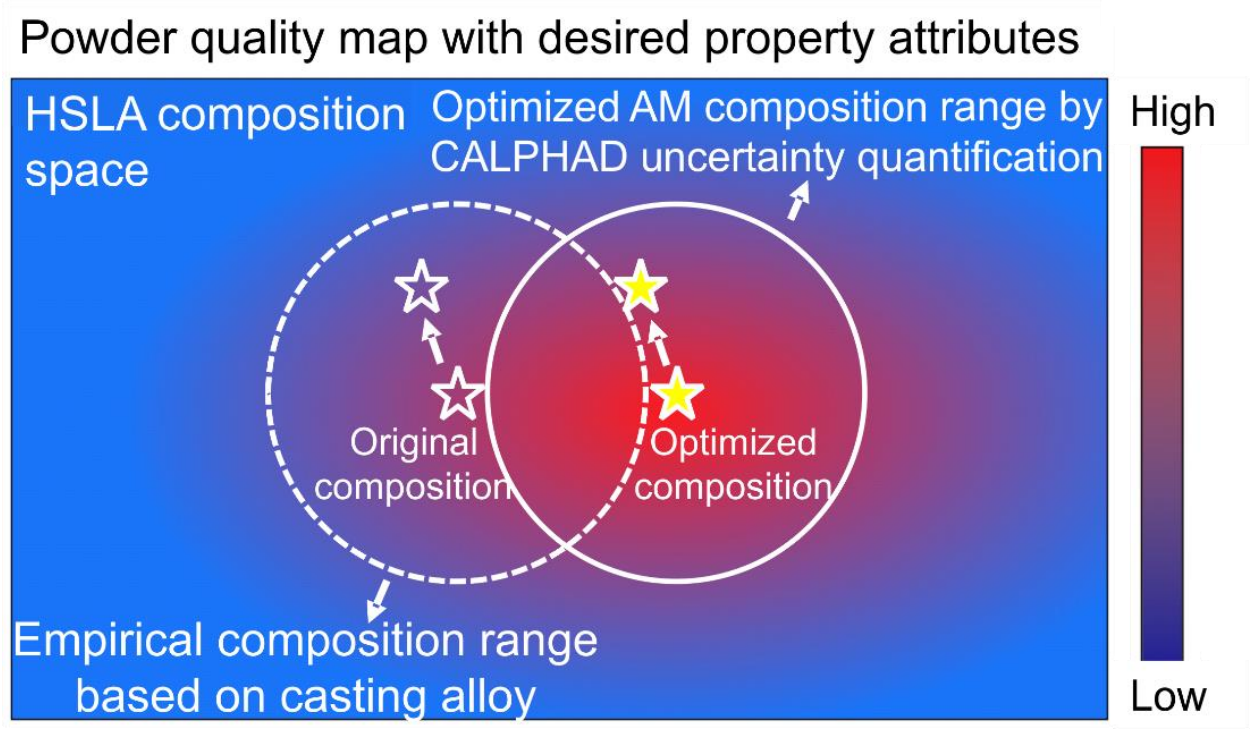

Figure 3-10 Conceptual graphic illustrating the improvement of composition with uncertainty after ICME optimization. The color bar indicates the satisfaction of the powder composition, i.e., powder quality, with the potential to match the requirements of the design target.

According to Fig. 3-9, the optimized composition exhibits higher strength and lower ITT without sacrificing weldability. Most importantly, the lowest strength and highest ITT among the 50,000 samples taken from the optimized composition with uncertainty are still higher than 115 ksi (793 MPa) and lower than 0°C, respectively. As a result, the optimized composition shows a higher chance of achieving successful builds (99.996%) compared with the initial composition (55.266%). Figure 3-10 illustrates how the composition was shifted to gain the highest success rate with a fixed composition uncertainty. In the composition space, there is a subspace that can meet all the required properties. However, all the initial compositions with variation may not be present

in that subspace, i.e., with the deviation from nominal composition, the AM build may not have the required properties. After the optimization, the nominal composition is shifted, and as a result, all the possible compositions meet the requirements considered with composition uncertainty.

3.5 Machine Learning Accelerated Robust and Optimal Design

The above optimization is used for reliability design which can only reduce the likelihood of failure and ensure that the product can meet the property requirements with uncertainty in composition. Sometimes, the robust design to achieve consistent performance with composition uncertainty or the optimal design to have the best average performance is required for specific applications. A comprehensive screening with much more calculations is required for a robust or optimal design, which brings a computational challenge.

To quickly perform the robust and optimal design, this work adopted the machine learning approach to build surrogate models to optimize the alloy composition [146–149]. All models were evaluated using 10-fold cross-validation [112]. Statistical analyses, such as Spearman's rank correlation and Sobol's indices, were performed to understand the influence of elements on the properties [150–154]. An optimal composition set with 69 compositions was found, and some compositions are close to the composition determined in this work. The details are given in the following context. Table 3-5 shows how we build the machine learning surrogate model and how we find the optimal and robust compositions.

The first step of building machine learning is constructing the training database. As a result, we firstly generated 500,000 samples from the screening composition range listed in Table 3-6 using the LHS method to cover the design screening space. The properties of interest of all compositions have been calculated using the CALPHAD-based modeling framework discussed in Chapter 3.1.3

Table 3-5 Steps of determining the optimal composition using surrogate models

Step	Description
1	Sample 500, 000 samples using the LHS method, and calculate the properties of interest using CALPHAD-based ICME modeling framework
2	Build surrogate models using gradient boosting algorithms and 500, 000 compositions calculated in step 1, evaluate models using 10-fold cross-validation
3	Perform Spearman's rank correlation analysis and calculate Sobol's indices to reveal the elements' influence and the importance of elements in the uncertainty of critical properties and determine the screening compositions
4	Prepare 100 000 compositions using the LHS method within the uncertainty range of each screened composition and calculate the property of interest & find the optimal compositions that all 10, 000 compositions within its uncertainty range meet all property requirements.

Table 3-6 Summary composition range in wt.% used for building the surrogate model

Fe	C	Cr	Cu	Mn	Nb	Mo	Ni	Si	Al
Bal.	0.02 - 0.1	0.1 - 1.1	0.8 - 1.7	0.2 - 2.1	0.01 - 0.1	0.2 - 1.2	2 - 5	0 - 0.5	0.01 - 0.1

The criterion for the Graville diagram is a linear regression and can be calculated quickly, so there is no need to build a surrogate model for it. Four surrogate models predicting the yield strength, freezing range, impact transition temperature (ITT), and the phase fraction of cementite were built by using the 500,000 calculated results and gradient boosting (GB) algorithm [148,149]. The cementite fraction is calculated since it is detrimental to the ITT temperature. Moreover,

cementite does not show in the composition space for the reliability design, but it shows in some of the compositions defined by Table 3-6. All models were evaluated using 10-fold cross-validation [112] to ensure the model has not only high accuracy but also good generalizability. During the cross-validation, the 500,000 samples were randomly split into ten subsets, and the model was fitted with nine subgroups (training dataset) and tested with the remaining subgroup (testing dataset). After training and testing ten times, the average performance metrics such as the mean absolute error (MAE), root mean square error (RMSE), and coefficient of determination (R^2) were calculated using the following equations, respectively:

$$\mathrm{MAE} = \frac{\sum_{i=1}^{n}\left|y_i^{\mathrm{P}} - y_i^{\mathrm{S}}\right|}{n} \tag{3-19}$$

$$\mathrm{RMSE} = \sqrt{\frac{\sum_{i=1}^{n}(y_i^{\mathrm{P}} - y_i^{\mathrm{S}})^2}{n}} \tag{3-20}$$

$$R^2 = 1 - \frac{\sum_{i=1}^{n}(y_i^{\mathrm{P}} - y_i^{\mathrm{S}})^2}{\sum_{i=1}^{n}(y_i^{\mathrm{P}} - \overline{y^{\mathrm{P}}})^2} \tag{3-21}$$

where n is the number of data points in the testing dataset, y_i^{P} and y_i^{S} are CALPHAD-based model framework predicted property and surrogate model predicted results of the datapoint i, respectively. $\overline{y^{\mathrm{P}}} = \frac{\sum_{i=1}^{n} y_i^{\mathrm{P}}}{n}$ is the mean value of y_i^{P} in the testing dataset.

Table 3-7 lists the performance of the surrogate models. The MAE represents the average of absolute error of the model prediction, while the RMSE is the standard deviation of the error introduced by the surrogate model that penalizes the samples with large errors. R^2 measures to what extent the variance of a dependent variable can be explained by the variables in a regression model. For yield strength, ITT, and freezing range, more than 90 % variance of results can be explained by the model, and their MAE and RMSE are acceptable. But the model prediction of the

cementite phase fraction only has low MAE and RMSE, which means a small error made by the model. However, the R^2 is close to 0, indicating the variance cannot be well-explained.

Table 3-7 Average of the MAE, RMSE, and R^2 of the 10-fold cross-validation

Properties of interest	MAE	RMSE	R^2
Yield strength (MPa)	33.80	44.52	0.93
ITT (°C)	16.00	20.76	0.94
Freezing range (K)	0.37	0.49	0.97
Cementite fraction	0.0000	0.0002	0.00

In order to reveal the element influence on the properties of interest, we first performed the Spearman's rank correlation [150] of the properties predicted by the CALPHAD-based modeling framework and the composition based on 500,000 calculated results. The Spearman's correlation coefficient ρ and its p are listed in Table 3-8. The coefficient ρ measures the strength of the monotonic relationship, and its value ranges from -1 to 1. A positive/negative value represents a positive/negative monotonic relationship, while 0 indicates no monotonic relationship between two variables. If the absolute value of ρ is smaller than 0.4, the monotonic relationship is weak; if ρ is higher than 0.6, the relationship is strong, and there is a moderate monotonic relationship if ρ is located between 0.4 to 0.6 [151]. The associated p indicates the chance that the null hypothesis is true, and the null hypothesis in calculating ρ is that we can get the same ρ when the two variables are not correlated. If the p is smaller than 0.05, one can conclude that calculated Spearman's coefficient is statistically significant [152].

Table 3-8 Spearman's correlation coefficient ρ and its p-value of the composition and properties of interest

	Graville diagram		Freezing range		Yield strength		ITT		Cementite fraction	
	ρ	p-value	ρ	p-value	ρ	p-value	ρ	p-value	ρ	p-value
C	-0.71	0.00	0.58	0.00	0.31	0.00	0.09	0.00	0.06	0.00
Cr	-0.08	0.00	-0.04	0.00	-0.31	0.00	-0.32	0.00	-0.08	0.00
Cu	-0.03	0.00	0.01	0.00	0.21	0.00	0.15	0.00	0.00	0.74
Mn	-0.13	0.00	0.18	0.00	-0.06	0.00	-0.07	0.00	0.03	0.00
Nb	0.00	0.63	0.16	0.00	0.48	0.00	-0.69	0.00	-0.01	0.00
Mo	-0.08	0.00	0.35	0.00	0.30	0.00	0.22	0.00	-0.07	0.00
Ni	-0.08	0.00	-0.50	0.00	-0.05	0.00	-0.09	0.00	-0.03	0.00
Si	-0.04	0.00	0.24	0.00	-0.01	0.00	-0.02	0.00	-0.01	0.00
Al	0.00	0.39	0.06	0.00	0.00	0.76	0.00	0.03	0.00	0.25

Take carbon as an example. The carbon content is correlated to all properties since they all have a non-zero ρ, and p-values are all 0. If the carbon increases, there is a strong monotonic trend to shift the Graville diagram from Zone I (1) to Zone II/III (0). The freezing range and yield strength have a moderate monotonic trend towards increasing when carbon is added to the alloy. Moreover, ITT and cementite fractions only show a weak positive monotonic relationship with carbon content. The influence of other elements can also be analyzed similarly. It is noted that Al has no monotonic relationship with the Graville diagram, yield strength, ITT, and Cementite and only has a weak positive relationship with a freezing range.

In order to reduce the dimension of screening composition space, the global sensitivity analysis was performed to reveal the contribution of each element on the variance of the property of interest by calculating Sobol's indices [153,154]. The first-order indices (S1) and total indices (ST) measure the contribution to output variance by a single input alone and the total contributions of an input that include interactions with other variables. The S1 and ST of each input in the surrogate model have been calculated and plotted in Fig. 3-11. Sobol's indices of Al are close to 0

in all surrogate models. Moreover, Al is not included in the equation for determining the location in the Graville diagram. As a result, during the composition screening process, Al is fixed as the original composition to reduce the number of compositions during the optimization. Similarly, if an element is highly correlated to the key properties and has a large contribution to the model prediction, i.e., large S1 and S2 values, there will be more screening grids for the composition for more accurate screening of the composition space. However, if the element has minor impacts on key properties, there will be less screening grid to reduce the number of calculations. Table 3-9 shows the screening grids based on Sobol's indices and correlation analysis. Finally, 5,334,336 nominal compositions will be screened.

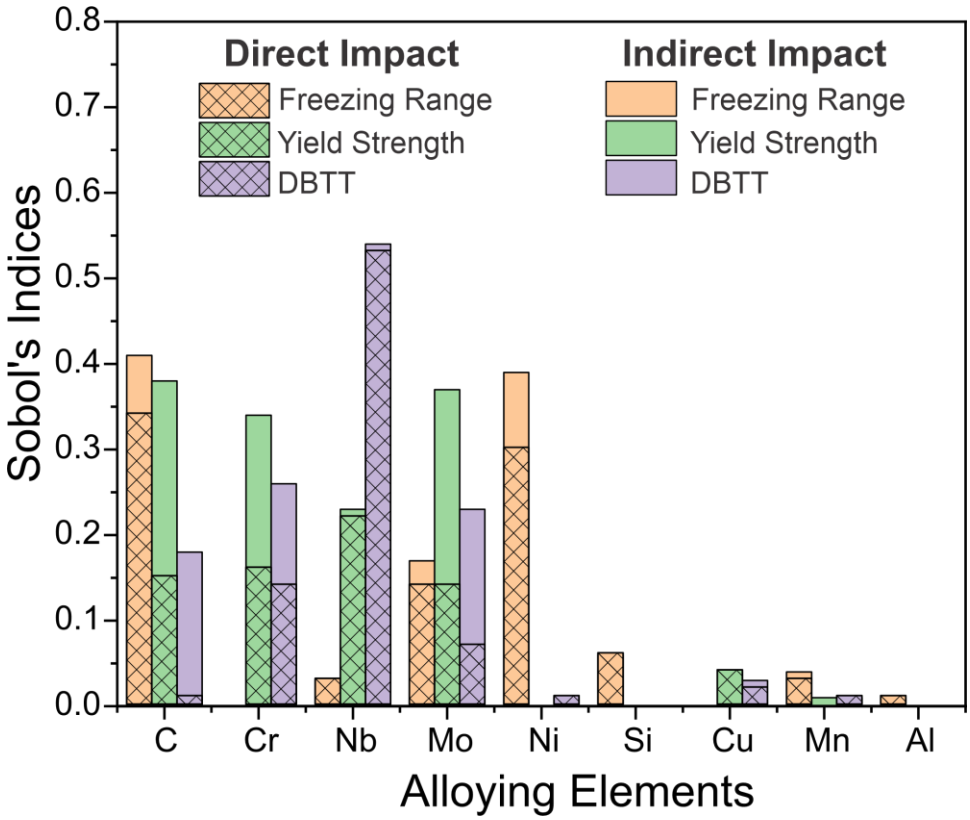

Figure 3-11 Sensitivity analysis of inputs in surrogate model

Table 3-9 Screening compositions and the uncertainty range

	Fe	C	Cr	Cu	Mn	Nb	Mo	Ni	Si	Al
Screening composition	Bal.	0.045, 0.050, …, 0.075	0.2, 0.3, …, 1.0	1.0, 1.15, …, 1.45	0.4, 0.6, …, 1.8	0.02, 0.03, …, 0.08	0.3, 0.4, …, 1.1	2.2, 2.4, …, 4.8	0.125, 0.250, 0.375	0.03
Uncertainty range	Bal.	± 0.025	± 0.1	± 0.15	± 0.2	± 0.01	± 0.1	± 0.2	± 0.125	± 0.01

For each grid defined by Table 3-9, 5,000 compositions have been generated using the LHS approach within the composition uncertainty range and calculated using the surrogate models. For example, for one composition defined by the smallest value in all elements, 5000 compositions were obtained from C:0.045 ± 0.025, Cr:0.2 ± 0.1, Cu: 1.0± 0.15, Mn:0.4± 0.2, Nb: 0.02± 0.01, Mo:0.3± 0.1, Ni:2.2± 0.2, Si:0.125± 0.125, Al:0.03± 0.01, and their properties were calculated. The mean and SD of the freezing range, yield strength an ITT, and the percent of samples meeting all property criteria (criteria are listed in the manuscript) of 5,000 compositions were also calculated. This procedure has been performed for all combinations listed in Table 3-9. The compositions that have a 100 % chance of meeting all property requirements have been stored and used for another screening. In the second screening, we generated 100,000 rather than 5,000 compositions to get more samples and modified the property criteria with the surrogate model RMSE to increase the reliability. The criteria are the Graville diagram located in zone I, freezing range < 13 – 0.5 K, yield strength > 793 + 45 MPa, ITT < 0 – 21 K, and cementite fraction < 0.0001 (Cementite is bad for low-temperature ductility). Finally, 69 compositions that enable all 100,000 compositions with their uncertainty range to meet all property requirements have been found in Table 3-10. Many of the compositions listed in Table 3-10 are close to what we designed using the ICME modeling framework results. However, the machine learning surrogate model

provides more feasible nominal compositions and helps us get the mean and SD for different properties. As a result, we could select the alloys with the best mean property for optimal design or the smallest SD for robust design.

Table 3-10 Optimal compositions determined using surrogate models *

C	Cr	Cu	Mn	Nb	Mo	Ni	Si	Al	Yield strength (MPa)		Freezing range (K)		ITT (°C)	
									Mean	SD	Mean	SD	Mean	SD
0.055	0.5	1.45	0.4	0.08	0.5	4	0.125	0.03	984	45	9.1	1.1	-137	20
0.055	0.5	1.45	0.4	0.08	0.5	4.6	0.125	0.03	982	46	9.1	1.2	-141	20
0.055	0.3	1.45	0.4	0.08	0.6	4.2	0.125	0.03	1035	51	9.4	1.1	-113	22
0.055	0.3	1.45	0.4	0.08	0.6	4.4	0.125	0.03	1035	52	9.4	1.2	-115	22
0.055	0.4	1.45	0.4	0.07	0.6	3.8	0.125	0.03	1029	53	9.6	1.0	-94	20
0.055	0.4	1.45	0.4	0.07	0.6	4	0.125	0.03	1030	53	9.3	1.1	-95	20
0.055	0.4	1.45	0.4	0.07	0.6	4.2	0.125	0.03	1030	53	9.2	1.1	-96	21
0.055	0.4	1.3	0.4	0.07	0.6	4	0.125	0.03	1016	54	9.4	1.1	-100	21
0.055	0.4	1.45	0.6	0.07	0.6	4	0.125	0.03	1027	54	9.5	1.1	-97	21
0.055	0.4	1.45	0.4	0.07	0.6	4.4	0.125	0.03	1030	54	9.1	1.2	-97	21
0.055	0.4	1.45	0.6	0.07	0.6	4.2	0.125	0.03	1027	54	9.4	1.1	-98	21
0.055	0.4	1.3	0.4	0.07	0.6	4.2	0.125	0.03	1016	54	9.2	1.1	-101	21
0.055	0.4	1.45	0.4	0.08	0.6	4	0.125	0.03	1046	54	9.5	1.1	-109	21
0.055	0.4	1.45	0.4	0.08	0.6	4.2	0.125	0.03	1046	54	9.4	1.1	-110	21
0.055	0.4	1.45	0.4	0.07	0.6	4.6	0.125	0.03	1029	54	9.2	1.2	-98	21
0.055	0.4	1.45	0.6	0.07	0.6	4.4	0.125	0.03	1027	54	9.4	1.2	-99	21
0.055	0.4	1.3	0.4	0.07	0.6	4.4	0.125	0.03	1016	54	9.1	1.2	-102	21
0.055	0.4	1.45	0.6	0.08	0.6	4	0.125	0.03	1043	54	9.7	1.1	-111	21
0.055	0.4	1.45	0.4	0.08	0.6	4.4	0.125	0.03	1045	54	9.3	1.2	-112	21
0.055	0.4	1.3	0.4	0.08	0.6	4	0.125	0.03	1033	55	9.5	1.1	-113	21
0.055	0.4	1.3	0.6	0.07	0.6	4.4	0.125	0.03	1012	55	9.4	1.2	-104	22
0.055	0.4	1.3	0.4	0.07	0.6	4.6	0.125	0.03	1015	55	9.1	1.2	-103	22
0.055	0.4	1.3	0.4	0.08	0.6	4.2	0.125	0.03	1033	55	9.4	1.1	-115	22
0.055	0.4	1.3	0.4	0.07	0.6	4.8	0.125	0.03	1015	55	9.2	1.2	-104	22
0.055	0.4	1.3	0.4	0.08	0.6	4.4	0.125	0.03	1033	55	9.3	1.2	-116	22
0.055	0.4	1.3	0.6	0.08	0.6	4.2	0.125	0.03	1030	56	9.6	1.1	-117	22
0.055	0.4	1.3	0.4	0.08	0.6	4.6	0.125	0.03	1032	56	9.3	1.2	-117	22
0.055	0.4	1.3	0.6	0.08	0.6	4.4	0.125	0.03	1029	56	9.6	1.2	-118	22
0.055	0.4	1.15	0.4	0.08	0.6	4.2	0.125	0.03	1022	57	9.4	1.1	-120	22
0.055	0.4	1.15	0.4	0.08	0.6	4.4	0.125	0.03	1021	57	9.3	1.2	-122	23
0.055	0.4	1.15	0.6	0.08	0.6	4.2	0.125	0.03	1019	57	9.6	1.1	-122	23

0.055	0.4	1.15	0.6	0.08	0.6	4.4	0.125	0.03	1017	58	9.5	1.2	-124	23
0.055	0.5	1.45	0.4	0.08	0.6	4	0.125	0.03	1026	64	9.5	1.1	-119	24
0.055	0.5	1.45	0.4	0.08	0.6	4.2	0.125	0.03	1027	65	9.3	1.1	-120	24
0.055	0.5	1.45	0.4	0.08	0.6	4.4	0.125	0.03	1026	65	9.3	1.2	-122	24
0.055	0.5	1.45	0.4	0.08	0.6	4.6	0.125	0.03	1025	65	9.3	1.2	-122	24
0.055	0.3	1.45	0.4	0.08	0.7	4.4	0.125	0.03	1076	67	9.6	1.1	-100	27
0.055	0.4	1.45	0.4	0.08	0.7	4.2	0.125	0.03	1084	77	9.7	1.1	-97	28
0.055	0.4	1.3	0.4	0.08	0.7	4.2	0.125	0.03	1072	78	9.7	1.1	-101	29
0.055	0.4	1.3	0.4	0.08	0.7	4.4	0.125	0.03	1071	78	9.5	1.1	-102	30
0.05	0.4	1.45	0.4	0.08	0.5	4	0.25	0.03	999	39	9.4	1.1	-128	17
0.05	0.4	1.45	0.4	0.08	0.5	4.2	0.25	0.03	999	39	9.3	1.1	-130	18
0.05	0.4	1.45	0.4	0.08	0.5	3.6	0.125	0.03	998	40	9.6	0.9	-125	17
0.05	0.4	1.45	0.4	0.08	0.5	4	0.125	0.03	998	40	8.8	1.1	-128	17
0.05	0.4	1.45	0.6	0.08	0.5	4	0.25	0.03	997	40	9.6	1.1	-131	17
0.05	0.4	1.45	0.4	0.08	0.5	4.4	0.25	0.03	998	40	9.3	1.2	-131	18
0.05	0.4	1.45	0.4	0.08	0.5	4.2	0.125	0.03	998	40	8.7	1.1	-129	18
0.05	0.4	1.45	0.6	0.08	0.5	3.8	0.125	0.03	995	40	9.2	1.0	-129	18
0.05	0.4	1.45	0.4	0.08	0.5	4.4	0.125	0.03	997	40	8.7	1.2	-131	18
0.05	0.4	1.45	0.6	0.08	0.5	4	0.125	0.03	995	40	9.0	1.0	-130	18
0.05	0.4	1.3	0.4	0.08	0.5	3.6	0.125	0.03	985	40	9.7	0.9	-131	18
0.05	0.4	1.45	0.6	0.08	0.5	4.2	0.125	0.03	995	41	9.0	1.1	-132	18
0.05	0.4	1.45	0.6	0.08	0.5	4.4	0.125	0.03	994	41	9.0	1.2	-133	18
0.05	0.4	1.45	0.8	0.08	0.5	4	0.125	0.03	991	41	9.2	1.0	-132	18
0.05	0.2	1.45	0.4	0.08	0.6	4	0.125	0.03	1018	54	9.2	1.1	-116	22
0.05	0.2	1.3	0.4	0.08	0.6	4.2	0.125	0.03	1004	54	9.1	1.1	-122	22
0.05	0.2	1.45	0.8	0.08	0.6	4.2	0.125	0.03	1011	55	9.5	1.1	-121	22
0.05	0.2	1.45	0.4	0.08	0.6	4.8	0.125	0.03	1016	55	9.1	1.2	-121	23
0.05	0.3	1.45	0.4	0.08	0.6	3.8	0.125	0.03	1029	57	9.5	1.0	-111	21
0.05	0.3	1.45	0.4	0.08	0.6	4	0.125	0.03	1029	57	9.2	1.1	-112	21
0.05	0.3	1.45	0.4	0.08	0.6	4.2	0.125	0.03	1029	57	9.0	1.1	-114	22
0.05	0.3	1.45	0.6	0.08	0.6	4	0.125	0.03	1027	57	9.4	1.0	-114	22
0.05	0.3	1.45	0.4	0.08	0.6	4.4	0.125	0.03	1028	57	9.0	1.2	-115	22
0.05	0.3	1.45	0.4	0.08	0.6	4.6	0.125	0.03	1027	58	9.0	1.2	-116	22
0.05	0.3	1.45	0.6	0.08	0.6	4.4	0.125	0.03	1026	58	9.3	1.2	-117	22
0.05	0.3	1.45	0.4	0.08	0.6	4.8	0.125	0.03	1027	58	9.1	1.2	-117	23
0.05	0.4	1.45	0.4	0.08	0.6	3.8	0.125	0.03	1033	64	9.5	1.0	-111	22
0.05	0.4	1.45	0.4	0.08	0.6	4.2	0.25	0.03	1033	64	9.5	1.1	-115	23
0.05	0.4	1.45	0.4	0.08	0.6	4	0.125	0.03	1034	64	9.2	1.1	-112	22

3.6 Additive Manufacturing and Experiments Verification

Due to the urgent time for the powder production, the full ICME model was not fully available when we designed the sample. As a result, I used the Ms temperature, precipitates fraction, freezing range, etc., to optimize the composition, and the composition is slightly different compared with the final optimized composition listed in Table 3-11. But the change of the composition trend is similar. The initial optimized composition (for powder production) and the final optimized composition both show higher C, Cu, and lower Cr. Some elements have different trends because the models implemented are different. The detail of the experimental study is available in the unpublished paper in our lab.

The sample was built using EOS M290 laser sintering machine, and print parameters are listed in the following: laser power 215 W, hatch spacing is 0.09 mm, layer height is 0.02 mm, and the laser travel is 741 mm/s. The as-built sample shows no cracks and a density higher than 99.5%, which is measured using the Archimedes method, indicating good printability. Then, the sample was homogenized at 950°C for 80 minutes followed by water quench, and then tempered at 550°C for 5 hours followed by water quench. Based on the Charpy V-notch test, the sample shows a ductile to brittle transition temperature lower than -20°C, which means the sample has good low temperature ductility. Finally, the room temperature performance was measured, and it shows the yield strength of 875 ± 22 MPa is above the requirement 115 ksi (793 MPa) and similar to the model prediction, which is 945 MPa in Table 3-12, first column. Moreover, the elongation is 23 %.

However, if the same composition shift happens in the original wrought HSLA composition, then, according to the model prediction, the yield strength will only be 677 MPa Table 3-12 second column and will fail the requirement. Moreover, assuming the exact composition change happens for the second optimized composition that is optimized using the full ICME model framework for reliability design, the sample will also meet the property requirements, indicating the strategy of adapting HSLA wrought composition for AM is effective.

Table 3-11 The optimized composition and the produced powder and printed sample composition.

	C	Cr	Cu	Mn	Nb	Mo	Ni	Si	Al	Fe
Sample Composition	0.042	0.41	1.32	0.77	0.03	0.84	3.45	0.19	0.006	Bal.
Powder Composition	0.046	0.4	1.44	0.9	0.03	0.8	3.47	0.19	0.006	Bal.
Initial Optimized	0.06	0.4	1.45	0.95	0.03	0.8	3.4	0.23	0.03	Bal.
Final Optimized	0.057	0.525	1.55	0.5	0.08	0.57	3.43	0.125	0.03	Bal.

Table 3-12 The composition and predicted key properties. Those properties are predicted for the ICP measured AM prints composition (composition variation for the firstly optimized composition), and what if the same error happens in the original wrought composition and the error happens in the second optimized composition. Fe is the balancing element. All compositions have similar freezing range and locate at Graville diagram Zone 1.

	C	Cr	Cu	Mn	Nb	Mo	Ni	Si	Al	YS pred. (MPa)	YS test (MPa)
ICP measured	0.042	0.41	1.32	0.77	0.03	0.84	3.45	0.19	0.006	945	875 ± 22
Same error in original composition	0.035	0.67	1.14	0.8	0.03	0.61	3.48	0.19	0.006	677	…
Same error in 2nd optimization	0.039	0.535	1.42	0.32	0.08	0.61	3.48	0.085	0.006	1001	…

3.7 Limitation of Current Study and Discussion on Uncertainties Sources

The uncertainty involved in this work includes aleatory and epistemic uncertainty [56]. The aleatory uncertainty refers to natural variation and is hard to avoid. In contrast, the epistemic uncertainty originates from the lack of knowledge and model approximations [155]. In this work, our primary goal is to study the influence of the aleatory uncertainty of composition in the performance of post-heat-treated AM builds and optimize the composition to gain higher chances of a successful build. We believe that based on the widely accepted physical models and the reliable databases developed over several decades, such as the TCFE steel database released by the Thermo-Calc software company [156,157], the ICME model prediction is adequate to guide composition optimization. However, it is noteworthy that the accuracy of the ICME model prediction relies on the quality of the CALPHAD database. Therefore, instead of performing a composition design based on the model prediction with absolute values, this work would rather aim at composition optimization by predicting the alloying effects with the trend analysis.

Due to the lack of experimental studies on the influence of composition change on AM build property, the uncertainty quantification for other uncertainty sources is challenging and is not performed in this work [47]. Other aleatory uncertainties from the processing parameters play an important role in the performance of AM. It should be further studied by coupling the CALPHAD-based ICME framework with the existing AM simulation models to address the process uncertainties in the future [20,158,159].

Epistemic uncertainty includes data uncertainty and model uncertainty [160]. Data uncertainty is originated from the limited information of data and is reduceable by collecting more

data. In this study, only the composition uncertainty range is available, while the composition distribution is yet unknown. As a result, we have assumed that the distribution of composition is uniform. Since provided composition within the uncertainty range meets the property requirement, the manufactured component should meet the property requirement regardless of the distribution. However, the calculated success rate may vary with different distributions. In the future, if massive production and chemical analysis are performed to gain the composition distribution, a more representative result can be obtained.

The other epistemic uncertainties that represent the difference between model prediction and experimental observation are called model uncertainty, which includes the model form uncertainty, solution approximation, and model parameter uncertainty [20]. Model form uncertainty stems from the assumption/simplification in the model. For example, it is assumed that the precipitate size is a fixed value in this work, while the real precipitate size is within a range and follows a specific distribution. It is possible to further increase the model accuracy by simulating precipitate size distribution [161] and incorporating the size distribution into the strengthening model [162]. Moreover, the porosity also determines the strength and ductility, while the influence of porosity is not considered in the current model framework. The model bias can be further reduced by integrating the porosity prediction into the ICME model framework [163].

The model parameter uncertainty originates from the fact that some parameters used in the model are not accurate enough. For example, the Hall-Petch coefficient used in this work is determined from references [131], while it may not be precisely the same for the alloy composition studied in this work, and it may lead to a discrepancy between the model output and experiments. Such uncertainties can be minimized by performing experiments to measure the parameter. As

shown in Table 3-7, there are discrepancies between the surrogate models and the original models. Such uncertainties can be reduced by generating more and unbiased training data, optimizing the hyper-parameters, etc. Finally, it is possible to calibrate models by experiment design and use the framework proposed by Kennedy and O'Hagan [104–106]. During the calibration process, the difference between model prediction and experiments can be modeled as a Gaussian process model, and the unknown model parameters shall be studied using the Bayesian calibration method [106].

3.8 Conclusions and Future Works

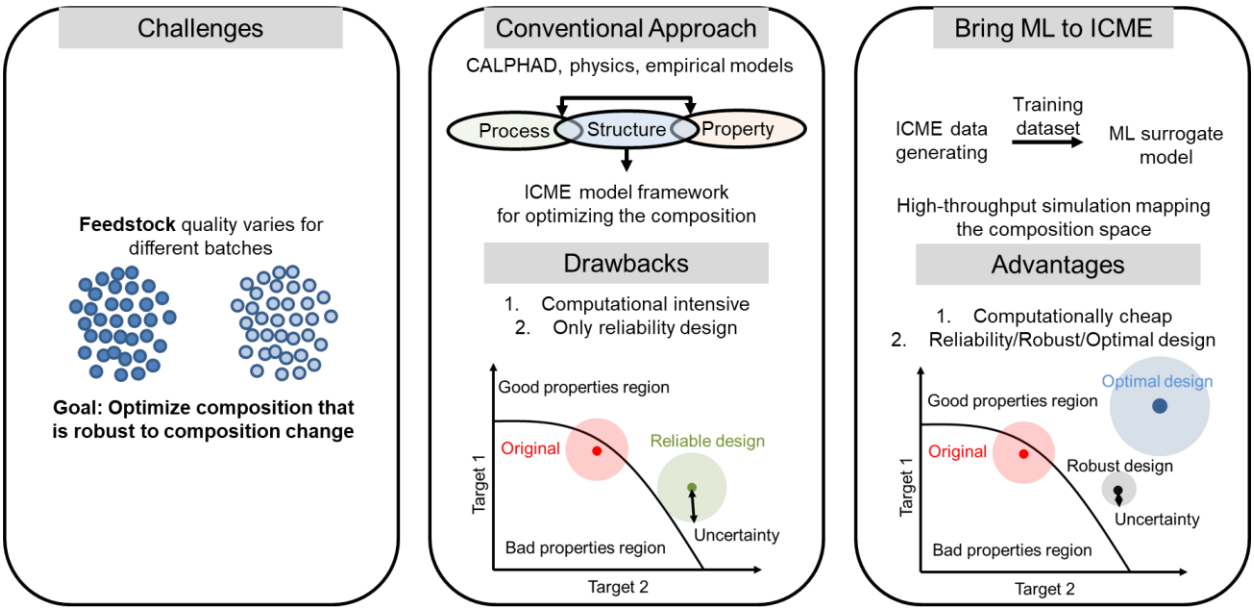

Figure 3-12 Summary of data-driven approach solving feedstock composition variation.

As shown in Fig. 3-12, the goal of this section is to optimize the feedstock composition that is robust to composition change, and the prints built from different batches of feedstock should have good performance for the application. In the conventional ICME approach, various models are integrated to simulate the process, structure, and property relationships. This method successfully increased the rate of a successful build by more than 40%. However, it is computationally intensive and can only be used for reliability design. As a result, the ML surrogate model was applied to accelerate the computation. Thus, it is possible to perform a robust design with small variations in the final product and the optimal design that has the best mean properties.

This work proves the effectiveness of the data-driven ICME approach in addressing the AM feedstock composition variation challenges. However, it still has several limitations that need to be addressed in the future.

1. The model framework is designed for a fully heat-treated sample. However, the printing parameters' impact on the residual stress, porosity, etc., should be considered for developing an as-built sample by applying other models, such as the FEA approach.
2. The model has only been verified with limited data due to the high cost of making customized powder. However, the model calibration should be conducted when more data are available. This requirement also necessitates sharing data in a platform worldwide for accelerating the data-driven approach model development.

4.0 Stacking Fault Energy Prediction via ML for AM Steel with Segregation

This chapter is modified from the publication:

- **Mainly from:** Wang, Xin, and Wei Xiong. "Stacking fault energy prediction for austenitic steels: thermodynamic modeling vs. machine learning." Science and Technology of Advanced Materials 21.1 (2020): 626-634. Figures and contents are reused under the CC-BY license.
- **Some discussions from:** Wang, Xin, et al. "Design metastability in high-entropy alloys by tailoring unstable fault energies." Science Advances 8.36 (2022): eabo7333. No figures and tables are copied from this paper in the thesis.

4.1 Evaluation of Different Models for Predicting SFE

4.1.1 Empirical Model

Although various empirical equations have been proposed for calculating the stacking fault energy [164–169], the equations for calculating SFE are inconsistent in different studies, as listed in Table 4-1. For example, the equations proposed by Schramm [164], Rhodes [165], and Yonezawa [168] show that adding Cr will increase SFE. On the contrary, Brofman [166], Ojima [167], and Bellefon [169] proposed that high Cr content leads to a lower SFE. This phenomenon indicates that the empirical equations are not very accurate, and most are localized for a limited

composition. Among all of the equations collected in this work, Bellefon *et al*. [169] equation was based on most of the data points, and it contains 144 different compositions. However, the prediction model was established for stainless steel. There is a need to build a model suitable for other austenitic steel, such as high Mn steels, with higher accuracy by utilizing a more comprehensive database and applying different algorithms.

Table 4-1 Summary of empirical equations for the SFE calculation

Authors	Empirical equations
Schramm [164]	SFE = -53+6.2Ni+0.7Cr+3.2Mn+9.3Mo
Rhodes [165]	SFE = 1.2+1.4Ni+0.6Cr+17.7Mn-44.7Si
Brofman [166]	SFE = 16.7+2.1Ni- 0.9Cr+26C
Ojima [167]	SFE = 5.53+1.4Ni-0.16Cr+17.1N
Yonezawa [168]	SFE = -7.1+2.8Ni+0.49Cr+2Mo-2Si+0.75Mn-5.7C-24N
Bellefon [169]	SFE = 2.2+1.9Ni-2.9Si+0.7Mo+0.5Mn+40C-0.016Cr-3.6

4.1.2 Thermodynamic Model

A thermodynamic model was proposed by Olson and Cohen [170] and has been adapted in many modeling of SFE in the austenitic steels [171–174]. Within this approach, an intrinsic stacking fault is defined as an hcp phase with two boundaries shared with the fcc matrix. The thermodynamic expression of the SFE is shown in Eq. (4-1) [170,174]:

$$\gamma = 2\rho\Delta G^{fcc\rightarrow hcp} + 2\sigma^{fcc/hcp}, \quad \rho = \frac{4}{\sqrt{3}a_{fcc}^2}\frac{1}{N_A} \qquad (4\text{-}1)$$

Where γ is the SFE (mJ/m^2), $\Delta G^{fcc\rightarrow hcp}$ is the Gibbs energies difference between the fcc and hcp phases [175] that can be modeled using the CALPHAD approach and commercial thermodynamic databases. Thermo-Calc [110] software with TCFE9 and TCHEA3 databases was used to calculate the Gibbs energy. The TCFE9 is mainly designed for steels, and TCHEA3 is constructed for multi-

principal element alloys. These commercial databases developed by experts are expected to achieve reasonable thermodynamic prediction over a wide composition range for multicomponent alloys by comparing with the ones reported in the literature, which are usually designated to specific steels with limited composition and temperature ranges. ρ is the molar surface density (mol/m^2) of {111} plane, N_A is the Avogadro's number, a_{fcc} = 0.36 nm is the lattice parameter of fcc, $\sigma^{fcc/hcp}$ = 8 mJ/m^2 is interfacial energy [175].

However, in most of the past research, the SFE model and Gibbs free energy functions for phases are designed for steels with 2-3 alloying elements [171–174], while modeling the multicomponent systems is challenging since it involves many parameters. Moreover, they have not been verified for alloys with a wide composition range [171,174,176]. Thus, this work evaluated the accuracy of the thermodynamic SFE model for more than 300 compositions collected (Fig. 4-1).

Although a few data points lie in the black dashed line in Figs. 4-1(a) and 4-1(b), indicating the equivalency between the thermodynamic model prediction (SFE_{calc}) and experiments (SFE_{exp}), but many other data points show a large deviation. Moreover, SFE_{exp} varies from 3 to 80 mJ/m^2, while SFE_{calc} with TCFE9 varies between -100 to 150 mJ/m^2, and the TCHEA3 predicted values were as high as 800 mJ/m^2. The large discrepancy between SFE_{calc} and SFE_{exp} may originate from the following reasons. First, the interfacial energy used in this work and other reports is constant, while it is a composition-dependent variable. Also, the difference in interfacial energy among previous studies differs by more than 20 mJ/m^2, which could introduce considerable uncertainty [93,173,176–179]. Secondly, most SFE measurements are performed at room temperature, while

the low-temperature CALPHAD databases for multi-component systems lack precision, and the current works mainly focus on the pure element and binary reassessment [180,181].

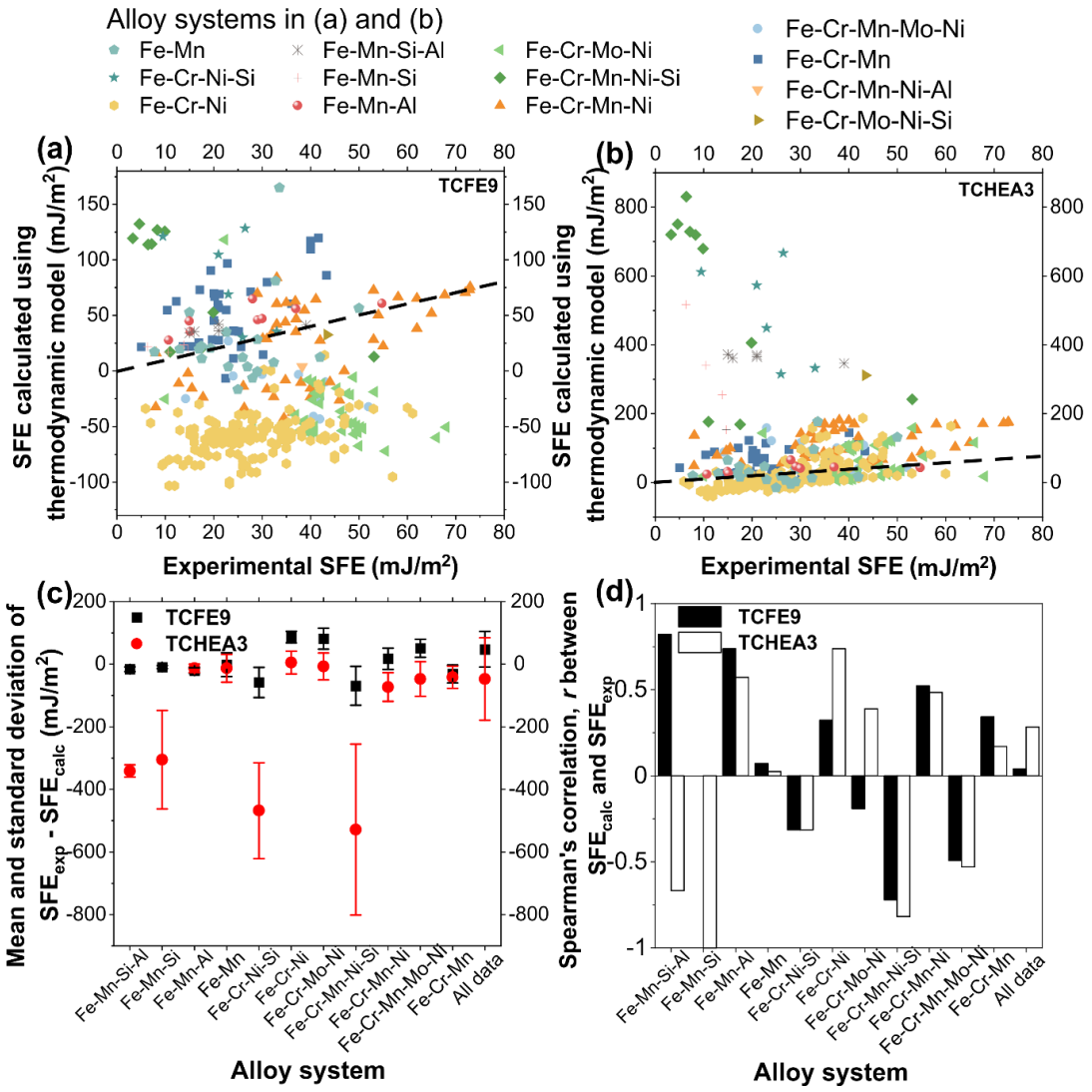

Figure 4-1 Comparison of SFE for different alloy systems between experimental value (SFEexp) and model-prediction based on CALPHAD databases (SFEcalc). (a) TCFE9 and (b) TCHEA3. The black dashed line indicates the equivalent relationship between SFEcalc and SFEexp, i.e., SFEcalc = SFEexp; (c) Mean value and SD for the difference between SFEcalc and SFEexp of different alloy systems; (d) The Spearman's correlation coefficient, r, between the SFEcalc and SFEexp for each alloy system.

According to Fig. 4-1(c), the two databases predict several alloy systems well. For TCFE9, the error in Fe-Mn-Si-Al, Fe-Mn-Si, Fe-Mn, and Fe-Mn-Al systems are relatively small. For TCHEA3, the error in Fe-Cr-Ni, Fe-Cr-Mo-Ni, Fe-Mn-Al, and Fe-Mn systems is acceptable. Moreover, Spearman's rank correlation coefficient *r*, a statistic measure of the strength of the monotonic relationship between two data that lies between -1 to 1, has been calculated and presented in Fig. 4-1(d). A positive value corresponds to a positive monotonic relation, i.e., as one variable increases, another also increases. A negative value indicates a negative monotonic relationship that when one variable increases, another variable will decrease. Moreover, 0 denotes that the two variables are not monotonically related. Suppose the absolute value of *r* is <0.4, 0.4-0.6, >0.6, and the correlation between the two variables can be interpreted as weak, moderate, and strong, respectively [151]. For Fe-Mn-Si-Al, Fe-Mn-Al, and Fe-Cr-Mn-Ni systems, the *r* values between SFE_{exp} and SFE_{calc} using TCFE9 are higher than 0.5, which indicates TCFE9 can predict the trend of SFE change with different elements in steels containing Mn. However, for the Fe-Cr-Ni system, TCHEA3 performs better with an *r* value of around 0.75, indicating that it is suitable for steels with high Cr and Ni. In summary, the performance of the thermodynamic model heavily depends on the quality of CALPHAD databases, which should be carefully chosen depending on the alloy composition.

To show the effect of temperature on the thermodynamic model accuracy, the whole dataset was split into three different groups: elevated temperature (300 < T < 600K, 12 samples), room temperature (300 K, 290 samples), and low temperature (94 < T < 300 K, 47 samples). The MAE of the CALPHAD prediction with different databases was calculated and listed in Table 4-2. The prediction error is relatively small at the elevated temperature compared to room and low

temperatures. Moreover, Spearman's correlation analysis of the temperature and the absolute error of CALPHAD-based calculation was performed. For TCHEA3 and TCFE9 databases, Spearman's correlation coefficient is -0.24 and -0.19, respectively. According to the negative correlation coefficient *r*, when the temperature is increasing, the error of CALPHAD simulation has a weak monotonic trend to decrease. Additionally, the magnetic contribution to SFE is significant at low temperatures, and there is a need to establish a robust and sophisticated magnetic model to improve the accuracy of the thermodynamic model [182,183]. Though the thermodynamic model is not accurate for all steels tested in this work, it is useful for certain alloy systems.

Table 4-2 MAE of TCFE9 and TCHEA3 prediction in the different temperature ranges

Temperature range	MAE of TCFE9 prediction (mJ/m^2)	MAE of TCHEA3 prediction (mJ/m^2)
300 K < T < 600 K	65.5	18.4
T = 300 K	62.8	72.0
94 K < T < 300 K	77.3	55.4

4.1.3 ab initio Approach

It is challenging and time-consuming for *ab initio* methods [184,185] to deal with chemical and magnetic energy contributions in complex multicomponent alloys [186]. Certain works underestimate the SFE and even report negative values [187,188]. Thus, some models are often only capable of predicting trends due to simple alloying effects with a limited composition range. As summarized by Sun et al. [189], TRIP happens when experiments measured SFE is below 20 mJ/m^2 and TWIP shows when SFE is in the range of 20-40 mJ/m^2, and the ab initio calculated and experiments measured SFE shows a good correlation. However, the absolute value of the

calculation and experiments are different, indicating it is hard to use the ab initio calculated SFE for the TRIP/TWIP alloy design.

4.1.4 Machine Learning Approach

Besides the aforementioned approach, a promising way to leverage the wealth of data and circumvent the difficulty of SFE prediction is by applying data-driven methods [190,191]. In recent years, only a few studies have applied ML for SFE prediction [192,193]. Das [192] predicted SFE using an artificial neural network (ANN) with 100 compositions as an input. But, that work did not incorporate temperature into the model, while the temperature is an important factor that controls SFE [194], and ANN requires an extensive database for generating a reliable model, which may limit the accuracy of this work. Chaudhary *et al.* [193] built a classifier that categorizes compositions into high, medium, and low SFE. However, the prediction of the actual SFE value is crucial since the SFE value is a key parameter in modeling the critical stress for twinning and the mechanical properties [195,196]. Thus, a systematic study for understanding the relationship between composition and SFE, together with building an accurate SFE predictor, is imperative. Overall, this work (i) assessed the quality of the CALPHAD-based thermodynamic model-prediction and revealed the importance of robust CALPHAD databases on accurate SFE prediction; (ii) discussed the influence of alloying elements on SFE through a statistical approach and found Ni and Fe have a moderate monotonic influence on SFE while other elements might have a complex effect; and (iii) predicted SFE using ML, and proved the performance of the ML model developed in this work was superior to the thermodynamic and empirical models.

4.2 Modeling SFE with Machine Learning

Figure 4-2 depicts the framework used in this work. A comprehensive literature survey was performed to construct an experimental database containing 349 entries with temperature, composition, and experiments measured SFE [98–102,165,167,168,170,174,197–237]. But compositions containing uncommon elements such as W and V were not collected since the number of data is limited. Further, we randomly split them into train and test datasets. Our dataset covered a broad range of compositions, and its descriptive statistics are listed in Table 4-3. Furthermore, we performed Spearman's correlation analysis using Python [111] and SciPy [238] to find the influence of alloying elements on SFE. Three different sets of features named Standard, WithTCFE9, and WithTCHEA3 were built to find out whether the thermodynamic model can enhance the model predictability. An appropriate selection of features, which distinguish the material and describe the property of interest, can lead to better performance of the ML model. Further, we evaluated the performance of 19 algorithms available in Scikit-learn [113] with different hyper-parameters for the three different feature sets using the 10-fold cross-validation [112] to discover the model with the highest accuracy and generalizability. The 75% train data is randomly split into ten subsets, and the model is fitted with nine subgroups and tested with the remaining subgroup [78]. After training and testing ten times, the average metrics values, such as the root mean square error (RMSE) and mean absolute error (MAE). Finally, the model with the lowest RMSE was selected and compared with the empirical and thermodynamic models.

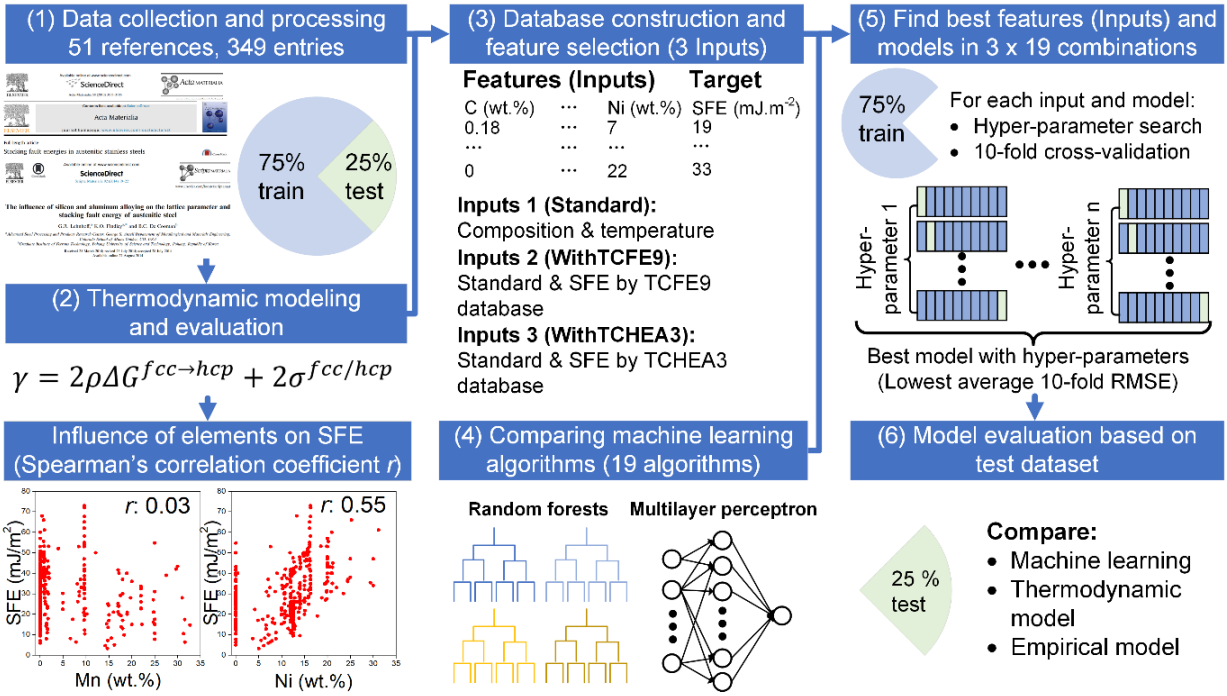

Figure 4-2 Schematic flow chart of this work.Including (1) data collection and curation (2) thermodynamic modeling of SFE (3) database construction and feature selection for machine learning (4) machine learning using 19 algorithms (5) finding best features (inputs) and models (6) model evaluation based on the test dataset.

Table 4-3 Descriptive statistics of the database used in this work.Temperature unit is Kelvin, composition is given as wt.%, SFE is in mJ/m^2

	Temperature	C	Cr	Mn	Mo	N	Ni	Si	Al	P	S	Fe	SFE
Mean	289.94	0.09	15.36	5.09	0.41	0.07	11.23	0.34	0.10	0.00	0.00	67.31	30.60
SD	46.87	0.26	6.39	8.18	0.89	0.15	6.87	0.99	0.52	0.01	0.00	7.19	13.55
Min	94.30	0.00	0.00	0.00	0.00	0.00	0.00	0.00	0.00	0.00	0.00	47.04	3.26
Max	598.15	3.21	30.00	32.69	2.70	1.00	31.16	6.22	4.80	0.07	0.04	86.46	72.97

4.2.1 Model Performance

Table 4-4 summarizes the mean RMSE and MAE of the 10-fold cross-validation for each model with optimized hyperparameters. We found that the ensembled tree algorithms, including random forest [239], GB, and XGBoost [240] algorithms, generate a more accurate model than other algorithms tested in this work. The GB model has an MAE of around 5.5 mJ/m^2 for all input sets. The RMSE is sensitive to large prediction errors and is reported to be near 8 mJ/m^2. This implies that a few large deviations happen during the prediction. Moreover, the overall performance of the ML models is reasonable for such an error. In our study, the ensembled methods always perform better than the multilayer perceptron (MLP, an ANN model) based on different metrics, suggesting that there are better algorithms for predicting SFE than ANN, as stated in the introduction. We also found that the overall performance is similar among the three input sets. Although the performance of adding TCFE9 calculated SFE is slightly better than the standard inputs, the improvement is minor. As a result, adding thermodynamic calculations does not significantly benefit the ML model.

Table 4-4 Performance of different algorithms for different input sets using 10-fold cross-validation (CV)

Machine learning algorithm	Mean RMSE (mJ/m^2) of 10-fold CV			Mean MAE (mJ/m^2) of 10-fold CV		
	Standard	With TCFE9	With TCHEA3	Standard	With TCFE9	With TCHEA3
Gradient boosting	7.8	7.8	7.9	5.5	5.5	5.5
Random forest	7.8	7.9	8.1	5.7	5.7	5.8
XGBoost	8.1	8.0	8.2	5.6	5.7	5.9
Huber	9.3	9.2	9.4	6.9	6.9	7.1
Adaptive boosting	9.3	9.3	9.5	7.6	7.6	7.7
K-nearest neighbors	9.4	8.9	9.3	6.8	6.6	7.0
Elastic net	9.5	9.2	9.5	7.1	7.0	7.1
Ridge	9.5	9.3	9.5	7.1	7.0	7.1
Kernel ridge	9.5	9.3	9.5	7.1	7.0	7.1
Lasso	9.5	9.2	9.5	7.2	7.0	7.1
Automatic relevance determination	9.5	9.3	9.5	7.2	7.1	7.2
LassoLars	9.5	9.3	9.5	7.2	7.1	7.2
Extra-trees	9.5	10.5	10.2	6.9	8.0	7.2
Monotonic regression	9.6	9.4	9.6	7.3	7.1	7.4
Bayesian ridge	9.6	9.3	9.5	7.2	7.0	7.1
Multilayer perception	9.7	9.5	10.1	7.4	7.2	7.3
Supporting vector machine	9.8	9.3	9.7	7.0	6.8	7.0
Decision tree	9.5	10.5	9.6	7.2	6.9	7.5
Stochastic gradient descent	11.4	11.3	11.3	9.3	8.9	9.1

Finally, the GB algorithm with optimized hyper-parameters was re-trained with 75% data and tested with untouched 25% data. According to Fig. 4-3(a), almost all the data in the training dataset align with the black dash line, which represents the prediction is the same as experiments. This implies that the ML model successfully correlates the composition and temperature to SFE for the training dataset. This model also performs well on the untouched test dataset, except for

one outlier. Based on the inset plot, it is clear that more than 70% of the prediction error is less than 10 mJ/m^2, which is close to the experimental error [169,211]. The error in SFE inferred from experiments may come from the equipment used for characterization, the inherent variation of SFE within a sample [199,241], and inaccurate elastic constants used when deducing SFE from experimental observation [99,174]. The performance of ML, thermodynamic, and empirical [169] models on the test dataset of SFE are compared, and the results are shown in Fig. 4-3(b). The MAE and RMSE of the ML model are the smallest among the empirical and thermodynamic models, confirming that ML is the most capable model for SFE prediction.

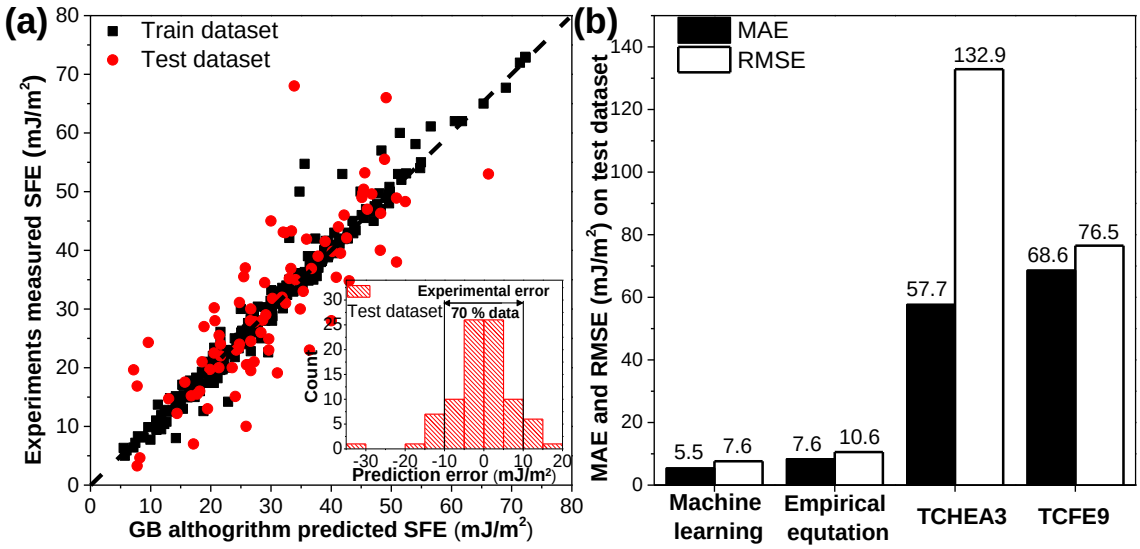

Figure 4-3 (a) Comparison of the experimental and ML predicted SFE. The black dash line represents the ideal case where prediction is same with measured SFE; (b) Comparison of the model accuracy between machine learning, empirical model, and thermodynamic modeling based on TCHEA3 and TCFE9 databases in terms of MAE and RMSE.

The advantage of the ML model is not only higher accuracy but also its ability to evolve continuously with more data [242,243]. Once the SFE measurements are reported, the new data

can be incorporated into the current dataset for improved prediction. Another pathway is to refine the thermodynamic models by improving the low-temperature database using the new lattice stability [181,244,245] coupled with an accurate prediction of interfacial energy to generate more reliable physical model-predicted data for ML model training.

4.3 Alloying Effects on SFE

4.3.1 Understanding the Influence with Statistical Analysis

Understanding the influence of alloying elements on SFE is crucial for alloy design and has attracted various studies [98,188,246]. However, due to the limited time and resources, previous work only focused on limited alloys to draw a conclusion. Vitos *et al.* [184] pointed out that the alloying effect on SFE is a function of alloying element content and the host composition. Thus, the general influence of elements on SFE remains unclear. Here, we calculated Spearman's *r* and the *p*-value for interpreting the relationship between each element and the SFE without considering the host composition. A *p*-value serves as evidence against a null hypothesis, and a smaller *p*-value indicates a low possibility that the null hypothesis is true. In this work, the null hypothesis is that the two variables are uncorrelated but still generate the exact Spearman's rank correlation. If a *p*-value is 0.05 (criteria used in Fig. 4-4), there is only a 5% chance of getting the same correlation coefficient *r* for two unrelated variables [152]. According to Fig. 4-4, Ni has the most pronounced effect in increasing the SFE regardless of the host composition, which agrees with the analysis by Das [192]. It was reported that from a total of 20 reports, 17 indicated an

increasing effect. Based on our study, C and Mn do not show a strong effect of increasing or decreasing the SFE. Because the *r* value is close to 0 and the p-value is larger than 0.05, which confirms that C and Mn do not have a statistically significant monotonic relationship with SFE. The importance of features in the GB has also been calculated and shown in Fig. 4-4(b). A high value denotes more times that this feature has been used as a critical decision in the model, and the feature is important in promoting the model's performance [247]. Based on Fig. 4-4(b), C and Mn are necessary for the SFE predictor generated through the gradient boosting (GB) algorithm [148]. This is because the effect of these elements on SFE is more complicated than that of Ni and varies with the host alloy, which has also been verified by the literature review [192]. For example, an *ab initio* study found that adding Mn into Fe-Cr-Ni stainless steel will always decrease the SFE at 0 K, and only increase the SFE at room temperature and when Ni content is higher than 16 % [248]. Meanwhile, Pierce et al. [174] showed that when Mn content was increased from 22 wt.% to 28 wt.% in Fe-xMn-3Al-3Si steel, the SFE increased monotonously. However, the Si [100,208] is generally considered to decrease the SFE. But this work gets a contradictory conclusion, which may be attributed to the collective effect from the data pertaining to different alloy systems, or because the traditional correlation analysis has limitations in studying the relationship between the composition and SFE since the relationship is complex and depends both on the alloying elements but also the matrix composition. As a result, a more advanced analysis should be performed to gain insights into the collected data.

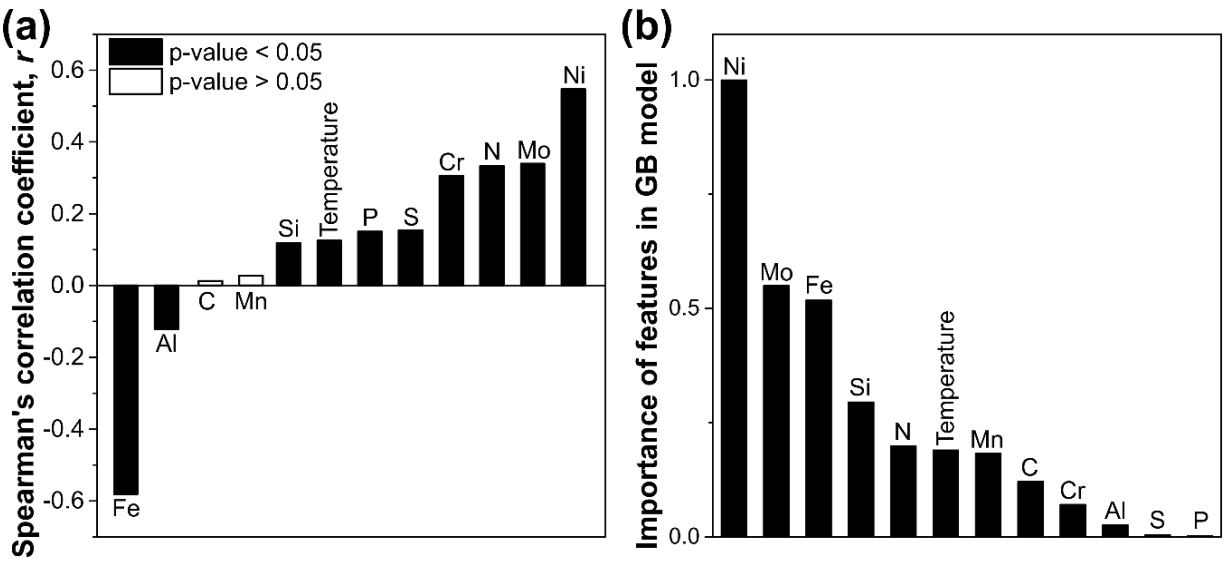

Figure 4-4 Analysis of the feature impacts on SFE.(a) Spearman's correlation coefficient and p-value for the SFE and all features used in this work; (b) Importance of each feature in gradient boosting (GB) model.

4.3.2 Understanding the Influence with Interpretable ML - SHAP

Usually, the machine learning model is considered as the black box, and thus, we lack confidence in using them as they may not interpret the data that aligns with our domain knowledge. Moreover, it is also essential to understand how the model works to have more confidence in the model and extract valuable knowledge. Recent efforts are working on model interpretability, such as SHAP [114] (SHapley Additive exPlanations), which is based on the game theoretic approach to explaining the output of any machine learning model. It connects optimal credit allocation with local explanations using the Shapley values from game theory and their related extensions. Fig. 4-5 summarizes the effects of machine learning model inputs on the SFE. From top to bottom, the impact of the input is decreasing, and from left to right, the feature has an effect on decreasing

SFE changes to increasing SFE. The color of each dot represents the value of the inputs for each data, and a blue color means the value of this data point has a low feature value in the dataset, and the red color means the value of this data point has a higher value. Take the Ni as an example, it is found that when the feature value is low (blue dots), the impact of Ni always decreases the SFE, and with more and more Ni added, the position of data moves from left to right which indicates adding more Ni will increase the SFE in most of the cases. This finding aligns with the literature view finding by Das et al. [249] that 17 works prove adding Ni will increase SFE in total 20 studies. And it also aligns with Fig. 4-4 with the conventional statistical analysis.

Similarly, we also know that adding Mo, N, Al, and S or increasing the temperature will lead to higher SFE while adding Si and P will decrease the SFE. The impact of adding Si is different from the correlation study in Fig. 4-4 but agrees with the literature study [100,208], proving the SHAP analysis for an accurate model helps discover the alloying effects on SFE and is better than the traditional correlation study. Elements like Mn and C also have a big influence on the SFE. However, both the red and blue dots span from left to right, indicating that the effect of those elements is not simple and may depend on the matrix composition. Those findings provide a guideline for composition optimization for TRIP/TWIP alloy design.

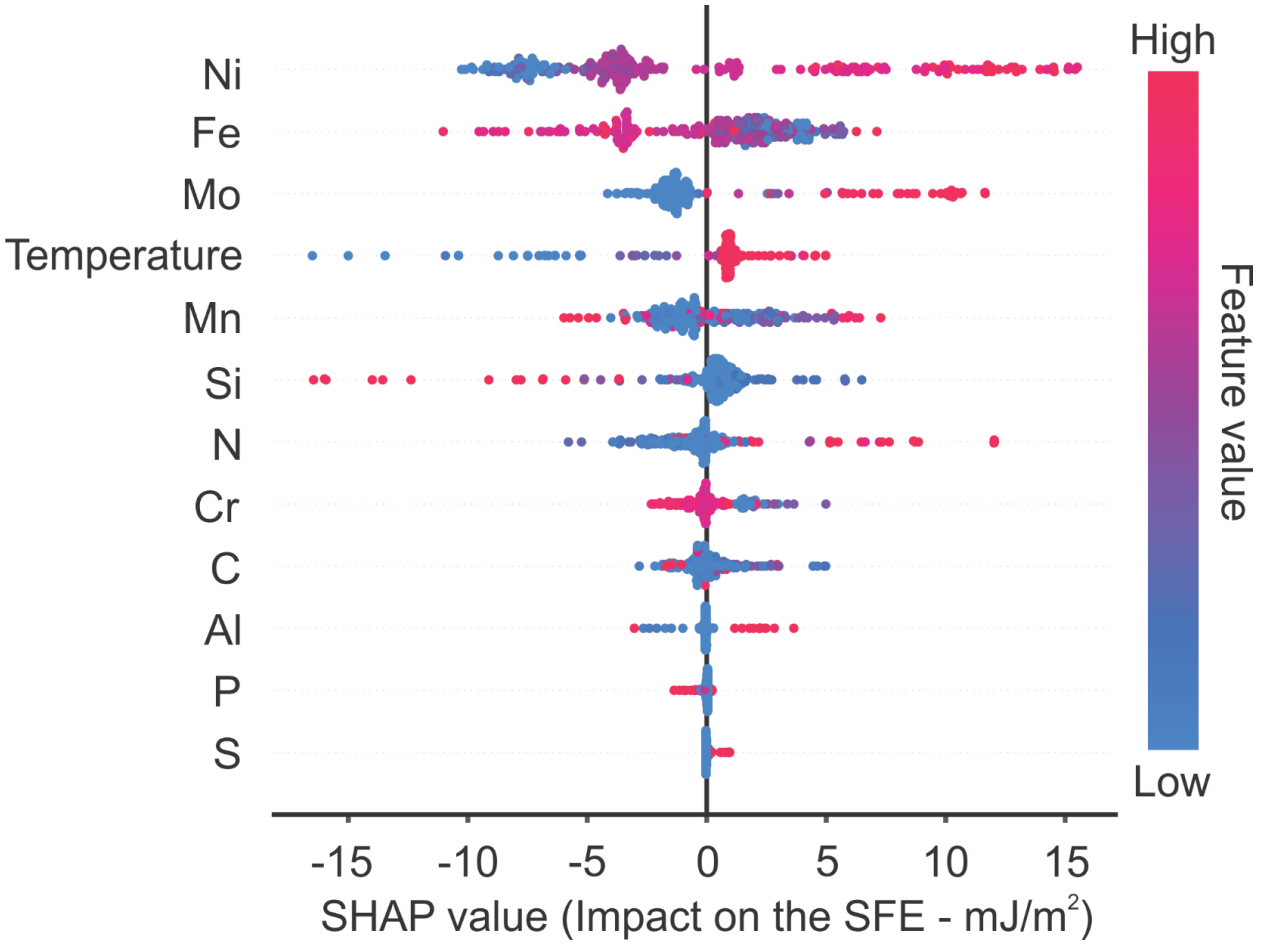

Figure 4-5 SHAP summary plot for SFE model with the 75% training dataset. From top to bottom, the feature importance is decreasing. From left to right, the impact of alloying elements changes from lower SFE to higher SFE. Each dot represents a data point.

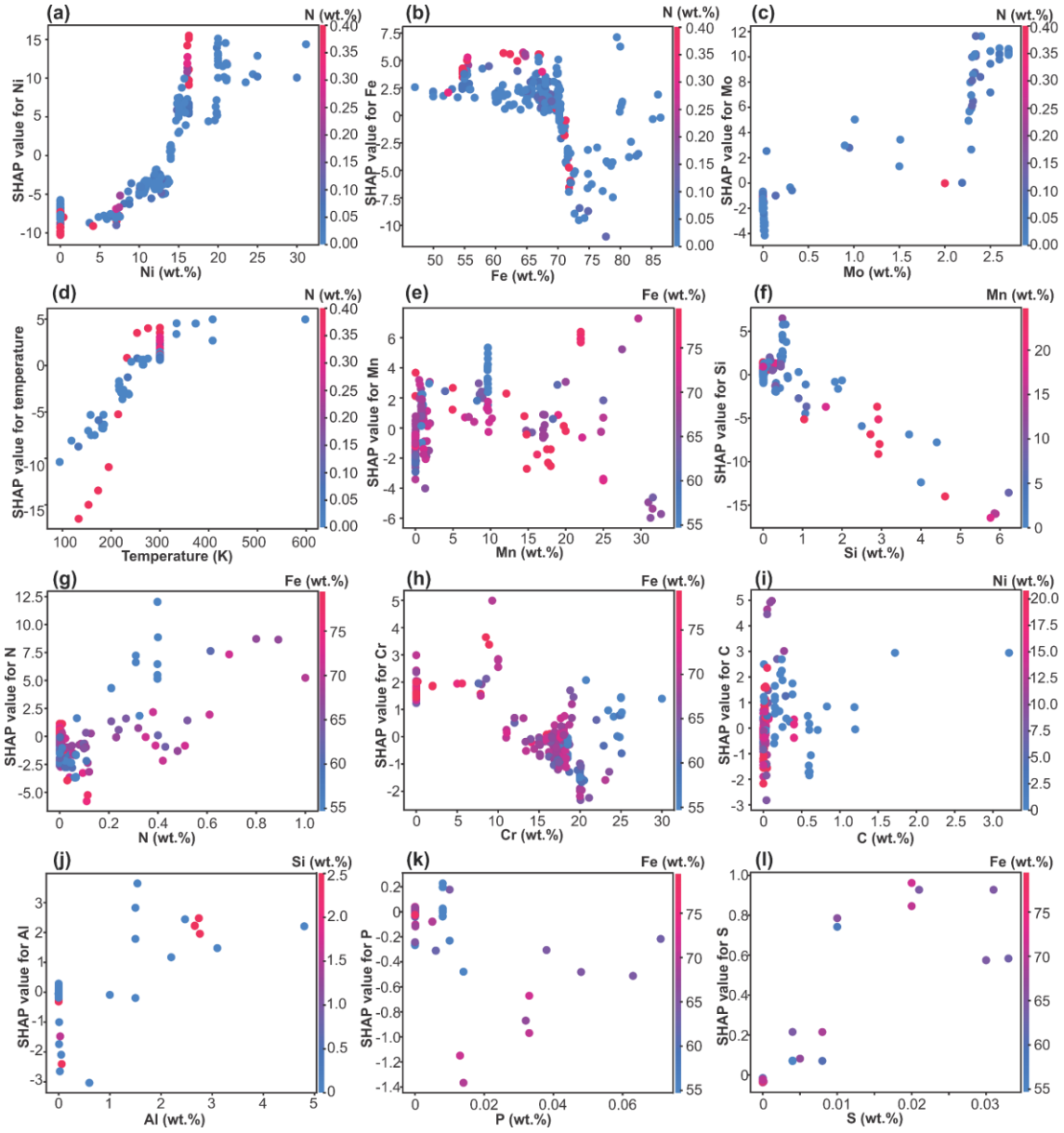

Figure 4-6 SHAP dependence plot for all features used in the machine learning model for training dataset. The dependence plot of (a) Ni content, (b) Fe content, (c) Mo content, (d) temperature, (e) Mn content, (f) Si content, (g) N content, (h) Cr content, (i) C content, (j) Al content, (k) P content, (l) S content. Each dot is a single prediction made in the model, the x-axis is the value of feature we have an interest, the y-axis is the SHAP value, i.e., how the feature value changes the output of the model, which is the SFE. The color represents the second feature value which interacts with the x-axis feature.

Moreover, we could also further study the effect of alloying elements by plotting the independence SHAP plot (Fig. 4-6). As shown in Fig. 4-6(a), adding more Ni will lead to higher SFE. But once the Ni content is above 15 wt.%, the SFE will not change too much. Furthermore, we also plot the interaction of Ni and N impacts on the SFE. The red symbol means the N content is high while blue symbol represents the alloy with low N content. When no Ni is added to the alloy, higher N content (red points) will lead to a lower SFE. On the contrary, when Ni content is higher than 15 wt.%, adding N will lead to higher SFE. In summary, the independence SHAP plots with machine learning can provide key knowledge of each alloying elements impact on the SFE. In summary, the data-driven approach provides an efficient and direct way to analyze the impact of alloying elements in the SFE.

4.4 Experiments: Applying SFE Model for AM Alloys.

The solute trapping model with the TCFE12 database was used to simulate the micro-segregation profile for AM 316L. The model inputs such as the nominal composition and scanning speed, is available in Woo et al. [97] and Pham et al. [18], respectively. The simulated composition from the start to the end of the solidification is presented in Fig. 4-7. For Fig. 4-7(a), all alloying elements will enrich at the end of solidification. However, for the composition simulated for Pham et al. work (Fig. 4-7(b)), the Co and Ni content will be depleted at the end of solidification. Based on section 4.3, the change of Ni, Mo, Mn, etc. elements content will change the SFE, which may in turn change the deformation mechanism for different locations in the AM build. As a result, the

data-driven based model was used to predict the SFE of the hundreds of data in the simulated profile.

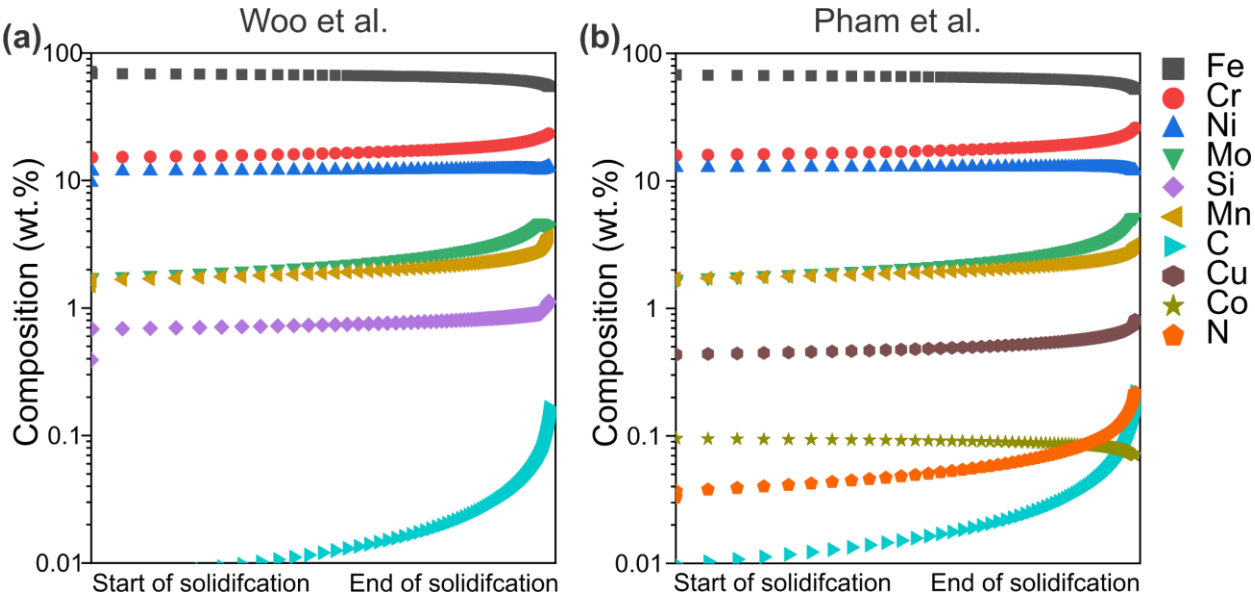

Figure 4-7 The simulated segregation profile.For Woo et al. [97], (b) Pham et al. [18]

Based on the SFE, the theoretical critical stress for twinning σ_{twin} can be calculated based on Byun's equation [95]:

$$\sigma_{twin} = \frac{2\gamma}{m \times b_p} \qquad (4\text{-}2)$$

where γ is the SFE (mJ/m^2), m is the Schmid factor, and $b_p = a/\sqrt{6}$ is the Burgers vector of partial dislocation, and a = 0.359 nm is the lattice parameter for 316L stainless steel. Here we took the average Schmid factor of 0.326 in this simulation [250]. Figure 4-8 shows the calculated critical stress based on the nominal alloy composition and the simulated segregation profile. The critical twinning stress for the nominal composition is much higher than the highest true stress during the tensile test, indicating twinning is unlikely to show during deformation. However, due to the

segregation, some parts of the print will show a reduced critical twinning stress, which is lower than the maximum true stress in Woo et al. work [97] or very close to the highest true stress in Pham et al.'s [18] work. Moreover, it is also found that the stacking fault energy may decrease during deformation [97], making the twinning easier to operate. In summary, the SFE offers a reasonable explanation of the TWIP phenomenon in AM 316L stainless steel.

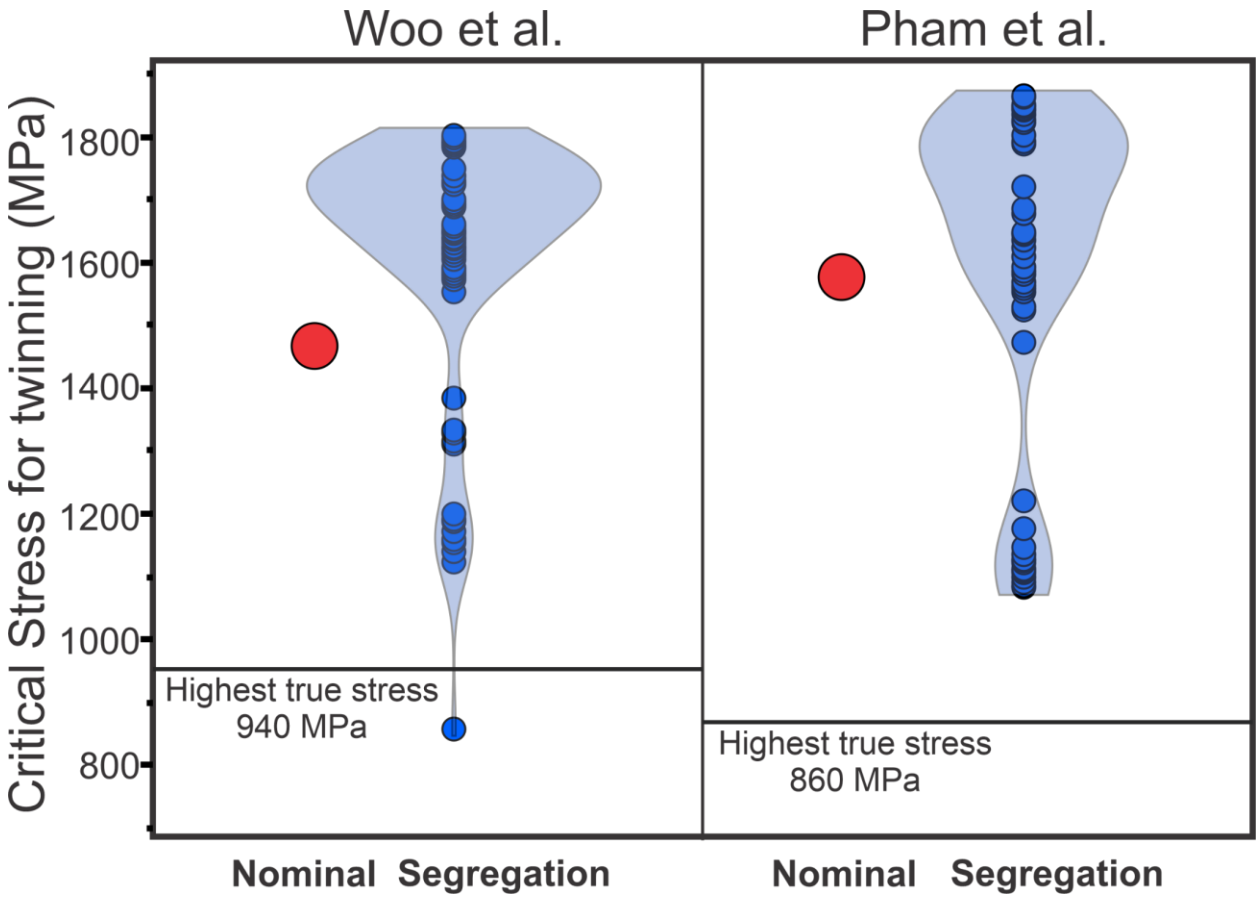

Figure 4-8 Critical twinning stress for AM 316L stainless steel.The calculation is performed for Woo et al. [97] and Pham et al. [18], respectively.

4.5 Conclusion and Future Work

In summary, compared with the thermodynamic model, empirical model, and ab initio approach, the machine learning model can predict the SFE in a timely and accurate manner. After applying the explainable ML tool - SHAP, the alloying effects on SFE have been revealed and provided for future alloy design. Finally, this model was used to explain the twinning phenomenon in AM 316L stainless steel.

However, several future works could be done to improve this work further:

1. The SFE model is purely based on composition and temperature. However, discovering more physics and structural based descriptors as the input may further improve the model performance.
2. The twining behavior may also be associated with other factors, such as residual stress caused during the deformation. Moreover, one of our recent studies shows that a low stacking fault energy is favorable for TWIP and TRIP. However, the competition between the unstable twin fault energy (UTFE) and unstable martensite fault energy (UMFE) is the actual factor controlling the TWIP and TRIP [251]. Currently, there are not enough USFE and UMFE data for the data-driven model.

5.0 Bayesian Model Calibration for Bulk Property Variation in AM

5.1 Yield Strength Model

Figure 5-1 illustrates the microstructure features that impact the yield strength. In this work, we will consider the solid solution strengthening, the second phase that is either precipitated or formed during the printing process, the grain boundary/cell boundary strengthening, the dislocation density strengthening, and the porosity difference. Moreover, Equation 5-1 is the mathematical equation used to calculate the strengthening contribution from microstructures illustrated in Fig. 5-1.

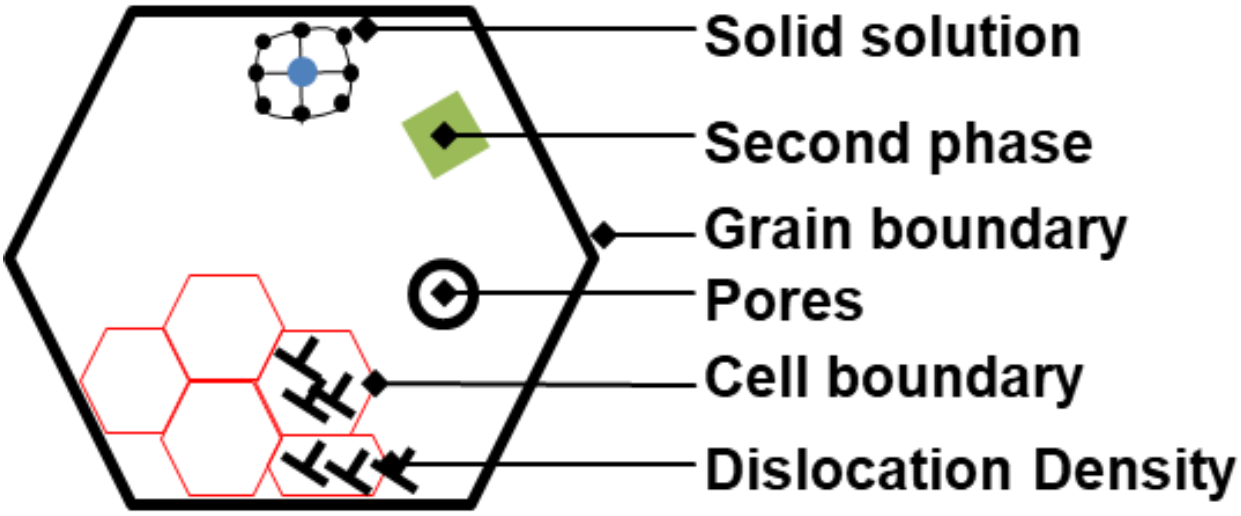

Figure 5-1 Schematic of the key structures impacting the strength of AM alloys

$$\sigma_y = \sigma_f + \frac{k}{\sqrt{d}} + \alpha M G b \sqrt{\rho} + \varepsilon \quad (5\text{-}1)$$

where σ_f is the sum of friction strength and solid solution strengthening effects. In CoCrFeMnNi alloys reported in the literature, most of them have a similar composition. The minor difference is caused by the feedstock composition variation and elements evaporation during AM, which usually has a negligible impact on the strengthening effect. The sum of solid solution strengthening and lattice friction stress in CoCrFeMnNi has been reported in many works, such as 125 MPa [252], 147 MPa [253], 160 MPa [254], 194 MPa [255]. In this work, the σ_f is taken as 160 MPa, which is close to the average of reported data.

The grain boundary or cell boundary strengthening is represented by $\frac{k}{\sqrt{d}}$, where k is the Hall-Petch coefficient, and d is the grain or cell size. In the study of AM CoCrFeMnNi HEA, most of the literature uses the grain size, and the coefficient value is 494 MPa/μm$^{0.5}$ [252,256], while some studies utilized the cell size for the grain boundary strengthening calculation [257]. As a result, there is a need to understand which structure should be used for the strengthening effect calculation. As plotted in Fig. 5-2, the LPBF as-built alloy shows a much smaller grain size than the cast one and is similar to the work-hardened and heat-treated casted alloys, while the DED as-built shows a larger variation in grain size. This work will use the grain size reported in the literature to study if the Hall-Petch coefficient for grain size is appropriate or if we should consider using the cell size.

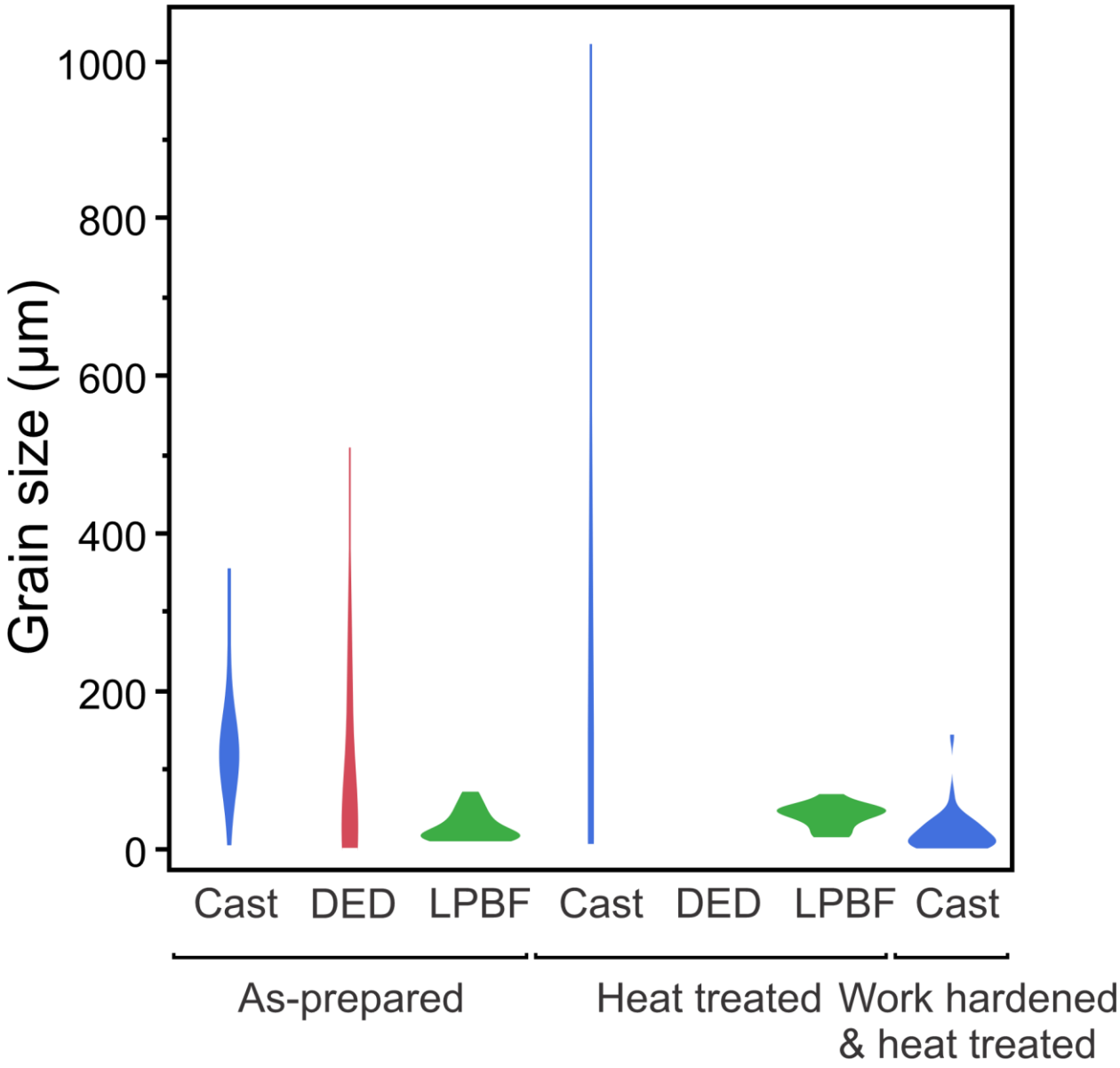

Figure 5-2 Literature review of the grain size difference in FCC HEAs.

The dislocation strengthening is calculated via the equation $\alpha MGb\sqrt{\rho}$, where α = 0.2 is a constant for FCC alloys, and M is the Taylor factor that depends on the grain texture and the tensile test loading direction. For most of the literature, without considering the grain texture, the M is

3.06. However, Taylor factors of additively manufactured CoCrFeMnNi HEA measured by Kim et al. range from 3.05 to 3.34 [258]. G is the shear modulus that is not sensitive to the microstructure and is measured to be 80 GPa at room temperature [259]. b = 0.254 nm is the magnitude of the Burgers vector of the full dislocation [258]. And ρ is the dislocation density that is usually measured by experiments, such as TEM and XRD. This work aims to reveal if the grain texture (represented by M) and dislocation density will significantly differ in AM compared with the casted Alloy.

The last item ε represents all other effects, such as the porosity difference or the Nitrogen/Oxygen introduced in the additive manufacturing process. Moreover, the cast CoCrFeMnNi HEA is a single fcc phase, while the additive manufactured HEA may also have the BCC, HCP, σ, Oxides, etc., as summarized by Zhang et al. [260]. Moreover, the literature seldom reports the N or O content, which may cause additional strengthening effects. Due to the complexity of those additional factors, I used only one simplified constant to represent all additional impacts. Moreover, only the single fcc CoCrFeMnNi HEA data will be included in the database for Bayesian model calibration.

5.2 Bayesian Model Calibration

The Bayesian and Gaussian model calibration were performed using OpenTURNS [115]. During the Bayesian calibration, the parameters are determined based on the literature. The Burgers vector b is set as 0.254 nm, shear modulus μ is set as 80 GPa, friction stress is set as 160

MPa, and the SD of experiments measured yield strength is set as 20 MPa. The parameters that need to be calibrated are set as follows: additional effect ε is 0 with an SD of 20 MPa, Taylor factor M is 3.06 with an SD of 0.2, Hall-Petch coefficient k as 490 MPa with an SD of 10 MPa, and the magnitude of dislocation density is 13 with an SD of 1. The Metropolis-Hastings algorithm was used for obtaining the samples during the Bayesian calibration process with a thinning parameter 3, a burn-in period of 1000. We used the Gaussian approach to find the model parameters within the range of Bayesian calibrated parameter ranges where the model outputs will match the experiments' measured yield strength.

After a comprehensive literature review and data curation, the final data are summarized in Table 5-1. Those works were selected because they did a comprehensive characterization to get the grain size, and room temperature static uniaxial tensile test. Moreover, the printed samples show a single fcc phase confirmed by XRD and SEM, and all samples have very low porosity to reduce the impact of pores and secondary phases that is not well described in Eq. 5-1. However, directly fitting the equation with those data may lead to various combinations of parameters that can fit well. Therefore, we adopted the Bayesian approach to combine the data of AM HEAs and the parameters adopted in previous literature for casted HEAs as the prior knowledge for better model calibration.

Figure 5-3 presents the probability density function (PDF) plot and the mean ± SD of the prior distribution in blue, which is based on the literature used parameter, and the posterior distribution in red, which is calibrated with experimental data.

The first column is the distribution of the Hall-Petch coefficient k, and it is clear the calibrated values for cast, DED, and LPBF are very similar to the prior mean value 490 MPa/$\mu m^{0.5}$,

and the SD is all close to 10 MPa/μm$^{0.5}$, which proves that using the grain size can accurately for model prediction, and it also agrees with a previous study [261]. Moreover, in the AM literature, I adopted the grain width of the columnar grains as grain size, indicating that grain width should be used rather than the grain length for the Hall-Petch coefficient.

Table 5-1 Summary of Collected Data of CoCrFeMnNi HEAs. WH represents work hardened and heat treated, H represents heat treated, AB represents as-built.

Manufacturing Approach	Beam diameter (μm)	Layer Thickness (μm)	Power (W)	Travel Speed (mm/min)	Hatch space	Grain size (μm)	Yield Strength (Mpa)	Reference
Cast - WH						9.8	484	[262]
Cast - WH						25	226	[263]
Cast - WH						17	229.6	[264]
Cast - H						25	537	[265]
Cast - WH						7.6	254	[266]
Cast - WH						2.2	649	[266]
Cast - WH						2.5	630	[267]
Cast - WH						2.8	406	[267]
Cast - WH						22.8	228	[267]
Cast - H						17	267	[268]
DED - AB	1800	450	1400	400		500	175	[269]
DED - AB		300	400	300	460	19	387	[270]
DED - AB		300	450	300	460	28	351	[270]
DED - AB	260	25	300	500		50	499	[271]
DED - AB	2500	600	880	600	1200	3.5	518	[272]
DED - AB	600	154	400	300	460	13	517	[254]
DED - AB		275	375	500	800	42	424	[273]
LPBF - AB	70	30	200	42000	120	24	565	[274]
LPBF - AB	60	30	160	72000	50	16.4	558	[275]
LPBF - AB	60	30	160	72000	50	15	564	[275]
LPBF - AB	60	30	160	72000	50	15.3	515	[275]
LPBF - AB	75	40	240	120000	50	12.9	510	[276]
LPBF - AB	65	50	200	45000	85	30	520	[277]

The second parameter is the Taylor factor *M*, while the mean and SD do not change very much. This result indicates that the grain texture in the AM build sample does not have a larger

difference than the work-hardened and annealed cast alloy. The average Taylor factor is close to 3.1 and ranges from 2.9 to 3.3.

The dislocation density shows a significant difference after the model calibration. In the prior distribution, the magnitude of dislocation density has a mean of 13, with the SD as 1. After the calibration, the cast alloy shows a dislocation density of $10^{12.88\pm0.54}$ /m^2, smaller than DED ($10^{14.05\pm0.16}$ /m^2) and LPBF ($10^{14.64\pm0.10}$ /m^2). Moreover, the dislocation density of LPBF is higher than DED, and the variation in LPBF is smaller than DED, and this is because the LPBF shows a higher cooling rate and less variation in processing parameters than DED. So, we could claim that besides the small grain size by AM, the high dislocation density is another root cause for higher yield strength in AM products. Fig. 5-4 shows the dislocation density deduced from model calibration, and it was compared with the XRD-measured dislocation density by the Williamson-Hall method [278]. The model-calibrated dislocation density is very close to the experimentally measured results, indicating that the calibration is reliable.

The last parameter is the additional constant used to summarize the impact of pores, secondary phase, and interstitial elements. As the results showed that there is no big difference between the three manufacturing processes, this might be because builds with secondary phases are excluded from the database, and those works only report the data with good print quality that has high density.

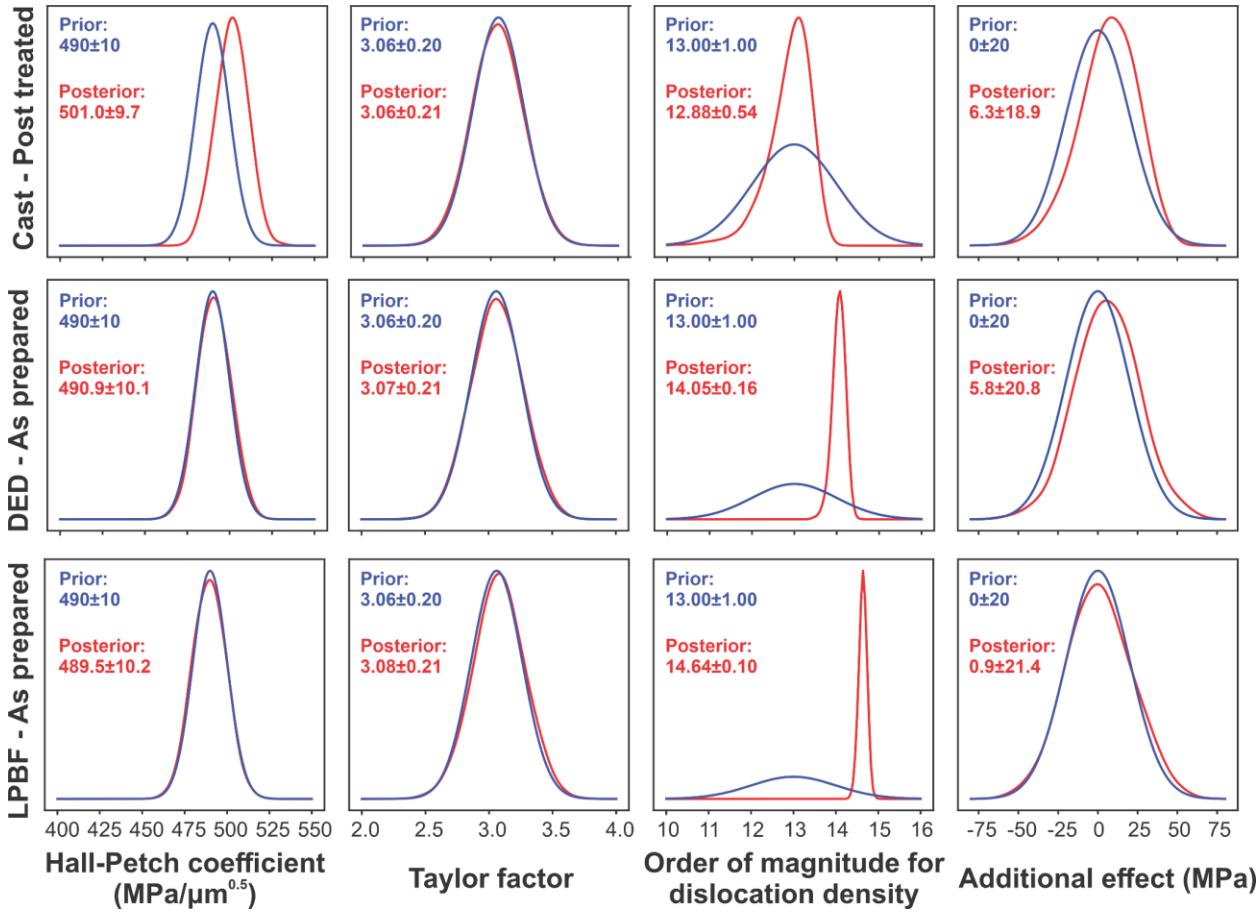

Figure 5-3 Summary of the prior and posterior distributions for each key model parameter. (a) Cast/work headend alloys with heat treatment. (b) as-prepared additive manufactured alloys. (1) Hall-Petch coefficient, (2) Taylor factor, (3) Magnitude of dislocation density, and (4) other effects including the impact of nano-size particles that cannot be detected by SEM and XRD, pores/cracks, etc.

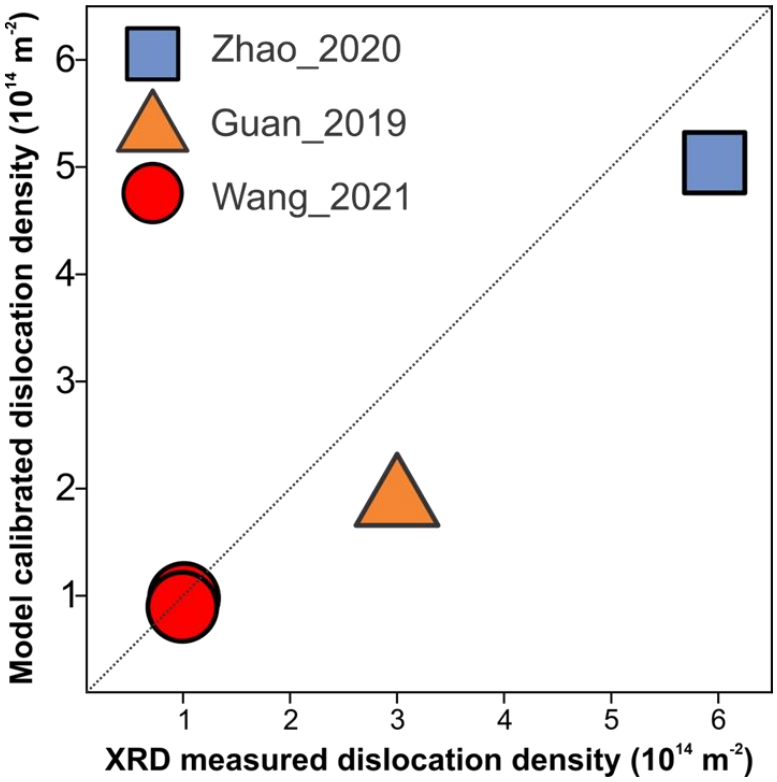

Figure 5-4 Comparison of experiments measured and the calibration deduced dislocation density. The references are coming from Zhao et al. [274], Guan et al. [254], and Wang et al. [270].

As discussed in Fig. 5-3, the difference in dislocation density and the grain size leads to the significant difference in yield strength of CoCrFeMnNi HEA manufactured by different approaches. Thus, the dislocation strengthening contribution based on the Bayesian calibrated dislocation density and grain boundary strengthening effects based on the literature-reported grain size has been plotted in Fig. 5-5. For the dislocation strengthening, the annealed cast CoCrFeMnNi will have a dislocation strengthening smaller than 100 MPa, with most of the work showing only the 50 MPa hardening effect. Dislocation strengthening in as-built DED alloy ranges from 100 to 200 MPa, while the as-built LPBF sample has an average strengthening effect of 250 MPa. The

grain boundary hardening effect shows more variations in post-processed cast alloy and as-built DED alloy, while the grain size of LPBF CoCrFeMnNi HEA is relatively stable. The grain size may change significantly in the LPBF sample because of the large variation in processing parameters, while the LPBF processing parameters are usually similar.

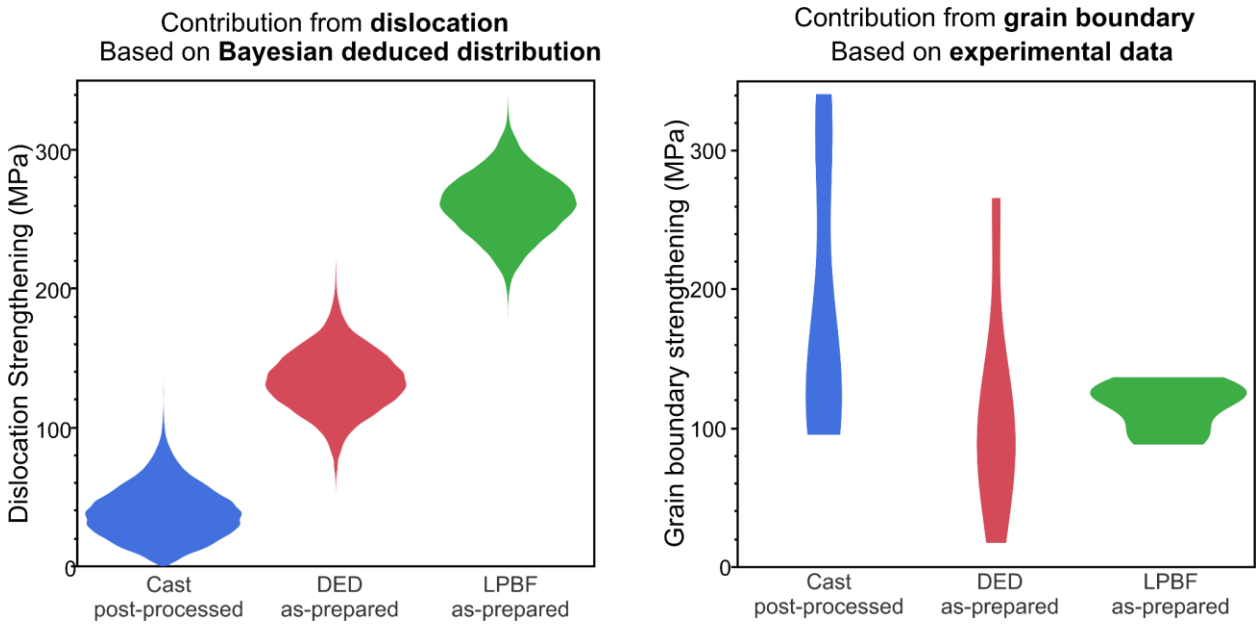

Figure 5-5 Comparison of the strengthening contribution difference in the cast, DED, and LPBF CoCrFeMnNi alloy. (a) The dislocation strengthening effects are based on the Bayesian calibrated data. (b) The grain boundary strengthening effects are based on the experimental data.

5.3 Correlation Study of Printing Parameters and Yield Strength

The correlation analysis was conducted to study the impact of different processing parameters on the yield strength and the strengthening effects contributed by grain boundary and dislocations. In addition to the beam diameter and other parameters directly set up in the machine,

the volumetric energy density (VED) and linear energy density (LED) were also included in the correlation study. The $LED = \frac{P}{v}$ and $VED = \frac{P}{vht}$, where P is the power, v is the scanning speed, h is the hatch spacing, and t is the layer height. Pearson's correlations are summarized in Table 5-2 for DED and Table 5-3 for LPBF, respectively. Due to the limited data, the threshold for statistical significance - α value is 0.25, which means there is a less than 25% chance that the tested data could have no linear correlation. All statistically significant results are bolded in the table.

Table 5-2 Correlation study for DED. The bolded correlation is statistically significant

DED parameters	Dislocation strengthening	Grain boundary strengthening	Yield strengthening
Beam diameter	**-0.88**	0.50	-0.29
Layer height	**-0.85**	0.48	-0.31
Power	**-0.72**	-0.06	**-0.66**
Scanning speed	0.14	0.39	0.33
Hatch space	-0.27	**0.75**	0.53
Linear energy density	**-0.75**	-0.28	**-0.83**
Volumetric energy density	0.51	-0.32	0.05

Table 5-3 Correlation study for LPBF. The bolded correlation is statistically significant

LPBF parameters	Dislocation strengthening	Grain boundary strengthening	Yield strengthening
Beam diameter	-0.21	0.00	-0.31
Layer height	-0.23	-0.45	**-0.60**
Power	-0.31	-0.05	-0.46
Scanning speed	-0.80	**0.87**	-0.45
Hatch space	**0.68**	**-0.80**	0.31
Linear energy density	**0.65**	**-0.94**	0.19
Volumetric energy density	0.33	0.24	**0.60**

As Table 5-2 shows, smaller beam diameter, layer height, lower power, and LED in the DED process will increase the contribution from the dislocation strengthening. Increasing the

hatch space will refine the grain size and contribute to the grain boundary strengthening effects. While for the LPBF process (Table 5-3), a larger hatch space and LED will increase the dislocation density but lower the grain boundary strengthening effects. Moreover, this differs from the impact of hatch space in the DED process. Due to the complex effect in both the dislocation and grain boundary strengthening, the yield strength does not show a significant correlation with the hatch space and LED. The LPBF builds yield strength will have a negative correlation with layer height and a positive correlation with volumetric energy density (VED).

5.4 Experimental Validation with LPBF 316L

Since the correlation is based on a few literature results, further experimental validation would be helpful to verify this finding. Due to the limitation in the HEA feedstock, I used the 316L stainless steel to validate the findings since 316L also has a single fcc structure, and the powder is available in the lab. Table 5-4 lists all the powder composition in wt.%, and Table 5-5 lists the printing parameters for printing the 1 x 1 x 1 cm 316L stainless steel. The design of experiments is based on the following levels of processing parameters: Power: 97.5, 295, and 292.5 W; scan speed: 541.5, 1083, and 1624.5 mm/s; hatch space: 0.05, 0.09, and 0.14 mm; layer height: 20 and 40 μm.

Table 5-4 Composition of 316L powder (wt.%)

Cr	Ni	Mo	Mn	Si	P	C	S	O	N	Fe
16.64	11.30	2.27	0.10	0.77	0.007	0.01	0.006	0.09	0.02	Bal.

Table 5-5 Design of experiments of printing parameter for 316L stainless steel.The beam size is fixed at 80 µm, rotation angle is 67°, while other tunable parameters are listed below.

ID	Power (W)	Scan speed (mm/s)	Hatch space (mm)	Layer height (µm)	LED (J/mm)	VED (J/mm^3)	Density Archimedes (%)	Density Optical (%)
1	292.5	1083	0.135	20	0.27	100.03	99.8±0.3	99.7±0.1
2	292.5	1624.5	0.09	20	0.18	100.03	100.0±0.3	99.5±0.1
3	195	1083	0.09	20	0.18	100.03	100.9±0.3	100.0±0.0
4	97.5	541.5	0.09	20	0.18	100.03	101.3±0.3	99.9±0.0
5	97.5	1083	0.045	20	0.09	100.03	99.5±0.3	99.2±0.1
6	195	1624.5	0.135	20	0.12	44.46	95.9±0.3	92.0±1.0
7	97.5	1083	0.09	20	0.09	50.02	95.8±0.3	94.8±0.5
8	195	1624.5	0.09	20	0.12	66.69	100.2±0.3	98.6±0.4
9	195	1083	0.135	20	0.18	66.69	101.0±0.3	99.5±0.1
10	97.5	541.5	0.135	20	0.18	66.69	100.4±0.3	97.8±0.3
11	97.5	1624.5	0.045	20	0.06	66.69	97.6±0.3	90.2±1.5
12	292.5	1624.5	0.135	20	0.18	66.69	100.2±0.3	98.4±0.3
13	195	541.5	0.135	20	0.36	133.37	101.2±0.3	100.0±0.0
14	195	1624.5	0.045	20	0.12	133.37	100.9±0.3	100.0±0.0
15	292.5	1083	0.09	20	0.27	150.05	101.1±0.3	100.0±0.0
16	292.5	541.5	0.135	20	0.54	200.06	100.9±0.3	99.9±0.1
17	195	1083	0.045	20	0.18	200.06	101.2±0.3	100.0±0.0
18	97.5	541.5	0.045	20	0.18	200.06	101.9±0.3	100.0±0.0
19	292.5	1624.5	0.045	20	0.18	200.06	101.7±0.3	99.8±0.1
20	195	541.5	0.09	20	0.36	200.06	99.9±0.3	99.9±0.1
21	292.5	1083	0.135	40	0.27	50.02	100.6±0.3	98.4±0.3
22	292.5	1624.5	0.09	40	0.18	50.02	100.9±0.3	99.3±0.2
23	195	1083	0.09	40	0.18	50.02	99.7±0.3	99.9±0.0
24	97.5	541.5	0.09	40	0.18	50.02	97.7±0.3	97.2±0.4
25	97.5	1083	0.045	40	0.09	50.02	93.7±0.3	90.9±0.8
26	195	541.5	0.135	40	0.36	66.69	100.9±0.3	100.0±0.0
27	195	1624.5	0.045	40	0.12	66.69	101.6±0.3	99.8±0.1
28	292.5	1083	0.09	40	0.27	75.02	100.8±0.3	100.0±0.0
29	292.5	541.5	0.135	40	0.54	100.03	99.0±0.3	100.0±0.0
30	195	1083	0.045	40	0.18	100.03	101.5±0.3	100.0±0.0
31	97.5	541.5	0.045	40	0.18	100.03	97.1±0.3	93.0±2.0
32	292.5	1624.5	0.045	40	0.18	100.03	100.0±0.3	99.7±0.1
33	195	541.5	0.09	40	0.36	100.03	NA	NA
34	292.5	1083	0.045	40	0.27	150.05	101.2±0.3	99.9±0.1
35	292.5	541.5	0.09	40	0.54	150.05	101.4±0.3	100.0±0.0
36	195	541.5	0.045	40	0.36	200.06	99.90.3	99.9±0.1

High densification is necessary for additive manufacturing, and many works utilize the volumetric energy density to optimize the processing parameters. A low VED will result in the formation of voids, while vaporization may happen when VED is too high. The 316L stainless

steel will show good printability when VED is in the range of 44.5-200 J/mm^3 [279,280]. With the appropriate volumetric energy density range for high densification, various combinations of power, scanning speed, hatch spacing, and layer height can be adopted. The builds porosity was measured three times using the Archimedes method, with the room temperature water density taken as 0.997 g/cm^3 and the theoretical density of the 316L (7.78423 g/cm^3) calculated using TCFE12 database. The dislocation density was also checked by using the optical images five times, and their average and SD are documented. Moreover, sample 16 was not printed at the desired height, and sample 35 was lost after the printing.

The sample Vickers hardness was measured to represent the yield strength as the hardness is easier to measure, and it has a positive correlation to yield strength. Figure 5-7 summarizes the impact of layer height on hardness for all prints with a density higher than 99%. It shows that increasing layer height will decrease the hardness, except for one condition at 195 W power, 1083 mm/s travel speed, and the 0.045 mm hatch space. Thus, we can claim that increasing the layer height will lower the yield strength, and this finding aligns with the findings in Table 5-3 that are based on the findings of CoCrFeMnNi HEA.

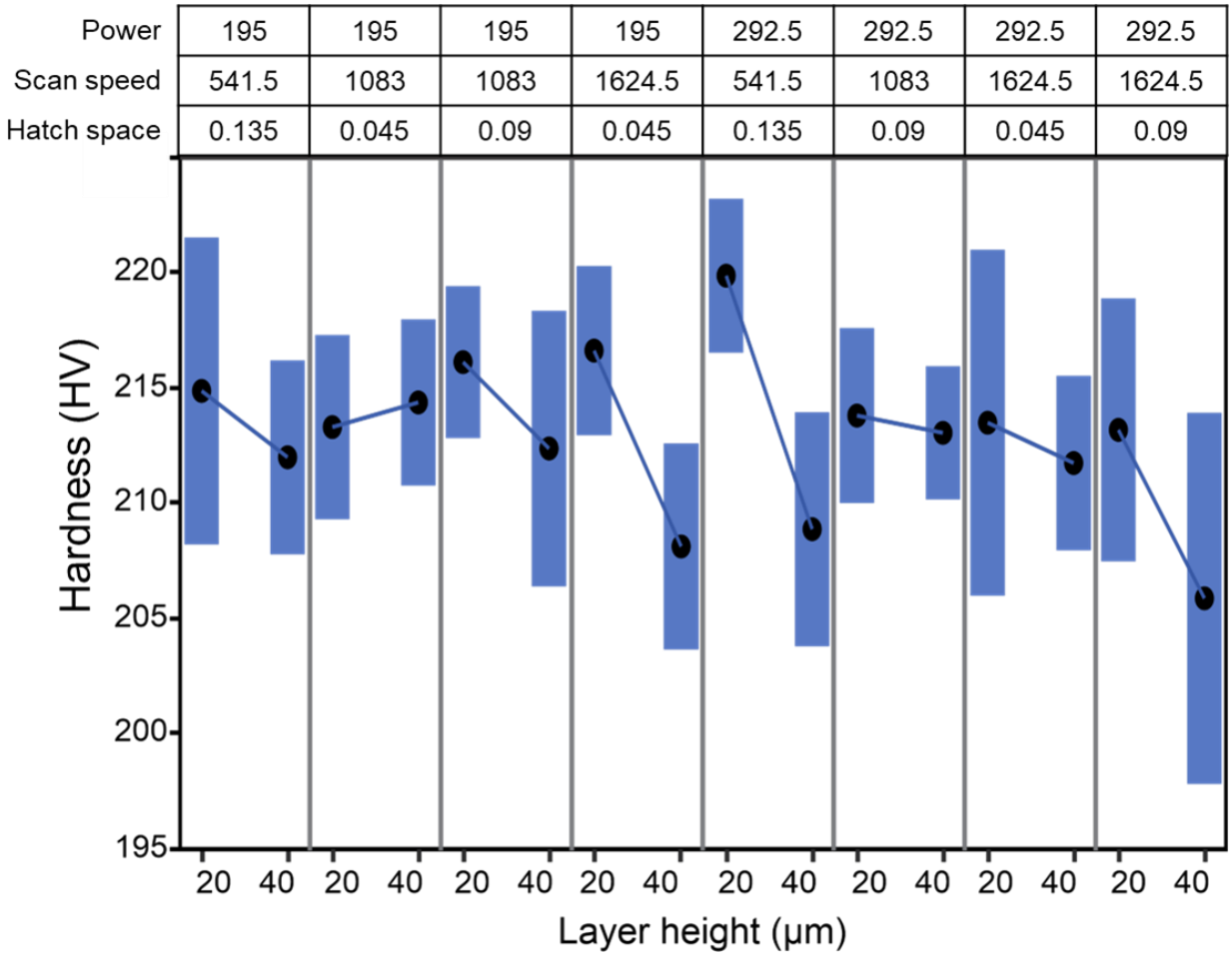

Figure 5-6 Impact of layer height on LPBF 316L hardness. Each column represents the experiments with the same power (W), scan speed (mm/s), and hatch space (mm), while the layer height varies from 20 to 40 μm. The black dot is the mean hardness, while the blue band is the SD of the measurement.

Moreover, the impact of other processing parameters with controlled experiments setting is summarized in Table 5-6. The number of conditions represents the total group of conditions with fixed all other processing parameters with at least two different values of the parameter of interest with a density higher than 99%. A positive correlation means increasing the parameter will lead to higher yield hardness, negative means increasing the parameter will lead to lower hardness,

and a complex correlation means the hardness will increase then decrease or decrease then increase. Clearly, the study agrees with Table 5-3 for the layer height, power, and scan speed. However, the 316L experimental study shows that increasing hatch space will decrease the hardness, while Table 5-3 shows a non-significant positive effect. This might be due to the limitation of experimental data and linear correlation study.

Table 5-6 Impact of processing parameter on hardness by experiments.

Parameter	Number of conditions	Positive correlation	Negative correlation	Complex correlation
Power (W)	11	3	8	0
Scan speed	10	4	3	3
Hatch space	9	2	7	0
Layer height	9	1	8	0

Moreover, the dislocation density ρ of several prints has been estimated by using the Williamson-Hall method [278], as shown in Eqs. 5-2 and 5-3.

$$\rho = \frac{2\sqrt{3}\varepsilon}{db} \tag{5-2}$$

$$FWHM * \cos\theta = \frac{0.94\lambda}{d} + 4\varepsilon\sin\theta \tag{5-3}$$

where ε is the average lattice strain, and d is the average grain size that both can be derived based on XRD profile, $b = a/\sqrt{2}$ is the burgers vector, and the lattice parameter a is 0.359 nm based on XRD measurement for all tested prints, FWHM is the full width at the half maximum intensity in the XRD profile for the selected peak, and θ is the degree of the Bragg's angle of the selected peak, the full width at half maximum intensity obtained from the XRD spectrum at the corresponding Bragg's angle of diffraction (θ), λ = 0.15406 nm is the wavelength of the X-ray of Cu source. The

dislocation density of 5 different samples was measured. Table 5-7 shows that the power of sample #5 is smaller than #17 and sample #26 is smaller than #29, while the dislocation density is #5 and #26 larger than #17 and #29, respectively. Moreover, #16 has a lower layer height than #19, while the dislocation density of #16 is higher than #19. Finally, the sample with lower hatch space (#5 and #17) also tends to show less dislocation density. All of those findings are similar to Table 5-3, which shows that using Bayesian to derive the properties that are hard to measure is an effective way to dig out more information from the literature and provide more data for analysis.

Table 5-7 Dislocation densities of 316L LPBF prints.

ID	Power (W)	Scan speed (mm/s)	Hatch space (mm)	Layer height (μm)	Dislocation density ($/m^2$)
5	97.5	1083	0.045	20	9.57E+14
16	292.5	541.5	0.135	20	1.15E+15
17	195	1083	0.045	20	6.50E+14
26	195	541.5	0.135	40	1.23E+15
29	292.5	541.5	0.135	40	5.91E+14

5.5 Conclusion and Future Work

In summary, this work applied the Bayesian model calibration methods to combine the physics-based yield strength model and a few experimental data to study the structural difference in conventional manufactured and AM alloys. The high strength and its variation in LPBF and DED as-built HEAs are found to be related to the dislocation density and grain size variation with different processing parameters. Moreover, it is also found that the Hall-Petch equation should be used with the grain size, and the columnar width should be used as grain size. Finally, the Bayesian

calibration can also be used to derive the dislocation density, which is rarely reported in the literature. The deduced value has been compared with XRD-measured dislocation density. The impact of processing parameters on the yield strength and the contribution from grain boundary and dislocation densities have been analyzed using correlation study and verified with experiments in LPBF 316L. Finally, the printing parameters' impact on the strength/hardness and the dislocation density has been investigated. However, this work also has some limitations, and some future work is desired:

- Notably, some important features, such as the shielding gas type, oxygen content in feedstock, and the differences in laser wavelength, were not included in this work since they are rarely reported in the literature. Moreover, the data is biased as the literature tends to report good print with high density and exclude the bad printing parameters that lead to builds with defects. As a result, the Bayesian approach in this work may be able to describe the PSPP relationship for conditions that result in successful build, not the conditions that will fail. It is desired that the researchers also report the failed prints and their properties to establish a comprehensive database for the data-driven study.
- Moreover, the segregation, residual stress, and many other parameters may also significantly impact the yield strength. For example, the tensile residual stress is detrimental to mechanical properties [281]. However, only a few literatures performed comprehensive characterization to study those properties.
- The challenges and limitations mentioned in the previous discussion highlight the need for more information reported in the literature and for establishing an open

database for storing and exchanging information to accelerate the data-driven approach for AM.

6.0 Summary and Future Work

In this dissertation, the variations in AM feedstock, microstructure, and as-built prints have been assessed by bringing the data-driven approach into the ICME model framework. The following conclusions can be drawn:

1. Data-driven model can surrogate the ICME model framework to describe the composition-process-structure-property relationship for the AM heat-treated components. Applying the machine learning approach, alloy compositions are optimized to be robust to variations and will always meet the properties requirements. The designed composition has been printed using the LPBF approach, and all the key properties have passed the requirements.

2. The local composition variation in AM prints challenges modeling for AM properties. In this thesis, a machine learning model has been established that provide an accurate and quick method for predicting SFE change along with the segregation in AM. This model outperforms the thermodynamic model and other empirical models. Moreover, it explains why the AM 316L stainless steel shows better mechanical properties and TWIP compared with the one manufactured using the conventional approach.

3. Lastly, this thesis discussed the structural origins of the yield strength difference in AM and conventionally manufactured HEAs. By using Bayesian calibration with limited experimental data, this work updated the structural parameters of the yield strength model for AM alloys based on prior knowledge about the parameters for conventional alloys. It reveals that the grain size and dislocation density are the key factors in controlling the mechanical properties of AM alloys.

Moreover, it studies the relationship between the printing parameters on the yield strength and dislocation density using correlation analysis. The findings were also confirmed by experiments for fcc single-phase 316L stainless steel.

Though this work explored combining materials science with data-driven approaches to solve some challenges in AM, more work is suggested in the future for more comprehensive research and full utilization of the data-driven approach in AM alloy and process design.

1. **Automated data extraction from literature and a platform to report data are necessary.** In the study of the SFE machine learning model and the Bayesian model calibration, one of the biggest challenges is the limited size of dataset. In the study of the SFE machine learning model and the Bayesian model calibration, one of the biggest challenges is the limited size of the dataset. In this thesis, all data were extracted from research papers manually and carefully to ensure the dataset is reliable. However, it is time-consuming for large dataset preparation. Recently, automated data extraction has been applied for materials database development with the development of natural language processing (NLP) and large language models (LLMs) [282–284]. For example, Maciej and Dane [285] presented a novel automated bulk modulus extraction method based on ChatGPT, which has achieved 100% precision and 90% recall rates. This means that 90% of the data has been accurately extracted by the machine learning model and all extracted data were correct. However, it is hard to fully rely on the NLP technique for database construction due to several factors. For example, low-quality results may be generated if the provided prompts are improper [286], and some data are presented in figures and tables rather than textual descriptions. Therefore, it is important to develop artificial intelligence tools for mining data accurately and comprehensively.

Moreover, many research works cannot be incorporated into the dataset due to the incomplete characterization or list of processing parameters. As a result, it is advised for the community to establish a standard way to report and share their data in a unified way to accelerate the data-driven model development.

3. **A comprehensive understanding of the AM processing-structural property relationship is desired.** This thesis work studies simplified problems in AM design. In the work of feedstock composition, this thesis focuses on the properties after heat treatment. Thus, the as-print structure and properties, such as segregation, residual stress, etc., are removed after heat treatment and are not considered in the modeling framework. In the work of local variation, the SFE is not sensitive to the microstructure and is determined by the composition. However, many other properties of interest are associated with the as-built structure, which is related to the printing parameters. Incorporating models addressing the printing parameters with the residual stress, grain size, textures, etc., is necessary for achieving the full capability of the ICME model framework for AM design.

Bibliography

[1] A. Vafadar, F. Guzzomi, A. Rassau, K. Hayward, Advances in metal additive manufacturing: a review of common processes, industrial applications, and current challenges, Appl. Sci. 11 (2021) 1213.

[2] J. Smith, W. Xiong, W. Yan, S. Lin, P. Cheng, O.L. Kafka, G.J. Wagner, J. Cao, W.K. Liu, Linking process, structure, property, and performance for metal-based additive manufacturing: computational approaches with experimental support, Comput. Mech. 57 (2016) 583–610. https://doi.org/10.1007/s00466-015-1240-4.

[3] T. Wohler, Additive manufacturing and 3D printing—state of the industry annual worldwide progress report 2014, Wohler's associates, Inc., Fort Collins, CO. (2013).

[4] I.E. Anderson, E.M.H. White, R. Dehoff, Feedstock powder processing research needs for additive manufacturing development, Curr. Opin. Solid State Mater. Sci. 22 (2018) 8–15. https://doi.org/10.1016/j.cossms.2018.01.002.

[5] A. Bandyopadhyay, Y. Zhang, S. Bose, Recent developments in metal additive manufacturing, Curr. Opin. Chem. Eng. 28 (2020) 96–104.

[6] M.D. Monzón, Z. Ortega, A. Martínez, F. Ortega, Standardization in additive manufacturing: activities carried out by international organizations and projects, Int. J. Adv. Manuf. Technol. 76 (2015) 1111–1121.

[7] H.A. Hegab, Design for additive manufacturing of composite materials and potential alloys: A review, Manuf. Rev. 3 (2016). https://doi.org/10.1051/mfreview/2016010.

[8] D. Bourell, J.P. Kruth, M. Leu, G. Levy, D. Rosen, A.M. Beese, A. Clare, Materials for additive manufacturing, CIRP Ann. 66 (2017) 659–681. https://doi.org/https://doi.org/10.1016/j.cirp.2017.05.009.

[9] G.A. Tapia Imbaquingo, Quantifying and Reducing Uncertainty in Metal-Based Additive Manufacturing Laser Powder-Bed Fusion Processes, (2018).

[10] W.Y. Wang, B. Tang, D. Lin, C. Zou, Y. Zhang, S.-L. Shang, Q. Guan, J. Gao, L. Fan, H. Kou, A brief review of data-driven ICME for intelligently discovering advanced structural metal materials: Insight into atomic and electronic building blocks, J. Mater. Res. (n.d.) 1–18.

[11] R. de Borst, Challenges in computational materials science: Multiple scales, multi-physics and evolving discontinuities, Comput. Mater. Sci. 43 (2008) 1–15.

[12] C.J. Kuehmann, G.B. Olson, Computational materials design and engineering, Mater. Sci. Technol. 25 (2009) 472–478.

[13] J. Allison, D. Backman, L. Christodoulou, Integrated computational materials engineering: a new paradigm for the global materials profession, Jom. 58 (2006) 25–27.

[14] W.Y. Wang, J. Li, W. Liu, Z.-K. Liu, Integrated computational materials engineering for advanced materials: A brief review, Comput. Mater. Sci. 158 (2019) 42–48.

[15] H. Fayazfar, M. Salarian, A. Rogalsky, D. Sarker, P. Russo, V. Paserin, E. Toyserkani, A critical review of powder-based additive manufacturing of ferrous alloys: Process parameters, microstructure and mechanical properties, Mater. Des. 144 (2018) 98–128. https://doi.org/10.1016/j.matdes.2018.02.018.

[16] Y. Kok, X.P. Tan, P. Wang, M.L.S. Nai, N.H. Loh, E. Liu, S.B. Tor, Anisotropy and heterogeneity of microstructure and mechanical properties in metal additive manufacturing: A critical review, Mater. Des. 139 (2018) 565–586. https://doi.org/https://doi.org/10.1016/j.matdes.2017.11.021.

[17] J. Günther, F. Brenne, M. Droste, M. Wendler, O. Volkova, H. Biermann, T. Niendorf, Design of novel materials for additive manufacturing - Isotropic microstructure and high defect tolerance, Sci. Rep. 8 (2018) 1298. https://doi.org/10.1038/s41598-018-19376-0.

[18] M.S. Pham, B. Dovgyy, P.A. Hooper, Twinning induced plasticity in austenitic stainless steel 316L made by additive manufacturing, Mater. Sci. Eng. A. 704 (2017) 102–111. https://doi.org/https://doi.org/10.1016/j.msea.2017.07.082.

[19] B. Brown, W. Everhart, J. Dinardo, Characterization of bulk to thin wall mechanical response transition in powder bed AM, Rapid Prototyp. J. (2016).

[20] Z. Hu, S. Mahadevan, Uncertainty quantification and management in additive manufacturing: current status, needs, and opportunities, Int. J. Adv. Manuf. Technol. 93 (2017) 2855–2874. https://doi.org/10.1007/s00170-017-0703-5.

[21] F. Lopez, P. Witherell, B. Lane, Identifying uncertainty in laser powder bed fusion additive manufacturing models, J. Mech. Des. 138 (2016) 114502. https://doi.org/10.1115/1.4034103.

[22] W.E. King, A.T. Anderson, R.M. Ferencz, N.E. Hodge, C. Kamath, S.A. Khairallah, A.M. Rubenchik, Laser powder bed fusion additive manufacturing of metals; physics, computational, and materials challenges, Appl. Phys. Rev. 2 (2015) 041304. https://doi.org/10.1063/1.4937809.

[23] W. Devesse, D. De Baere, P. Guillaume, The isotherm migration method in spherical coordinates with a moving heat source, Int. J. Heat Mass Transf. 75 (2014) 726–735.

https://doi.org/https://doi.org/10.1016/j.ijheatmasstransfer.2014.04.015.

[24] A. Klassen, T. Scharowsky, C. Körner, Evaporation model for beam based additive manufacturing using free surface lattice Boltzmann methods, J. Phys. D. Appl. Phys. 47 (2014) 275303. https://doi.org/10.1088/0022-3727/47/27/275303.

[25] M. Megahed, H.-W. Mindt, N. N'Dri, H. Duan, O. Desmaison, Metal additive-manufacturing process and residual stress modeling, Integr. Mater. Manuf. Innov. 5 (2016) 61–93. https://doi.org/10.1186/s40192-016-0047-2.

[26] C. Körner, E. Attar, P. Heinl, Mesoscopic simulation of selective beam melting processes, J. Mater. Process. Technol. 211 (2011) 978–987. https://doi.org/https://doi.org/10.1016/j.jmatprotec.2010.12.016.

[27] K. Dai, L. Shaw, Parametric studies of multi-material laser densification, Mater. Sci. Eng. A. 430 (2006) 221–229. https://doi.org/https://doi.org/10.1016/j.msea.2006.05.113.

[28] M.F. Zaeh, G. Branner, Investigations on residual stresses and deformations in selective laser melting, Prod. Eng. 4 (2010) 35–45. https://doi.org/10.1007/s11740-009-0192-y.

[29] Y.A. Chang, S. Chen, F. Zhang, X. Yan, F. Xie, R. Schmid-Fetzer, W.A. Oates, Phase diagram calculation: past, present and future, Prog. Mater. Sci. 49 (2004) 313–345.

[30] G.B. Olson, C.J. Kuehmann, Materials genomics: from CALPHAD to flight, Scr. Mater. 70 (2014) 25–30.

[31] L. Kaufman, J. Ågren, CALPHAD, first and second generation–Birth of the materials genome, Scr. Mater. 70 (2014) 3–6.

[32] S. Grimme, J. Antony, S. Ehrlich, H. Krieg, A consistent and accurate ab initio parametrization of density functional dispersion correction (DFT-D) for the 94 elements H-Pu, J. Chem. Phys. 132 (2010) 154104.

[33] N. Kouraytem, X. Li, W. Tan, B. Kappes, A.D. Spear, Modeling process–structure–property relationships in metal additive manufacturing: a review on physics-driven versus data-driven approaches, J. Phys. Mater. 4 (2021) 32002.

[34] C. Tian, T. Li, J. Bustillos, S. Bhattacharya, T. Turnham, J. Yeo, A. Moridi, Data-Driven Approaches Toward Smarter Additive Manufacturing, Adv. Intell. Syst. 3 (2021) 2100014.

[35] A. Agrawal, A. Choudhary, Perspective: Materials informatics and big data: Realization of the "fourth paradigm" of science in materials science, Apl Mater. 4 (2016) 53208.

[36] K. Schwab, The fourth industrial revolution, Currency, 2017.

[37] K.T. Butler, D.W. Davies, H. Cartwright, O. Isayev, A. Walsh, Machine learning for

molecular and materials science, Nature. 559 (2018) 547–555. https://doi.org/10.1038/s41586-018-0337-2.

[38] P. Raccuglia, K.C. Elbert, P.D.F. Adler, C. Falk, M.B. Wenny, A. Mollo, M. Zeller, S.A. Friedler, J. Schrier, A.J. Norquist, Machine-learning-assisted materials discovery using failed experiments, Nature. 533 (2016) 73–76. https://doi.org/10.1038/nature17439.

[39] C. Wen, Y. Zhang, C. Wang, D. Xue, Y. Bai, S. Antonov, L. Dai, T. Lookman, Y. Su, Machine learning assisted design of high entropy alloys with desired property, Acta Mater. 170 (2019) 109–117. https://doi.org/10.1016/j.actamat.2019.03.010.

[40] C. Te Wu, H.T. Chang, C.Y. Wu, S.W. Chen, S.Y. Huang, M. Huang, Y.T. Pan, P. Bradbury, J. Chou, H.W. Yen, Machine learning recommends affordable new Ti alloy with bone-like modulus, Mater. Today. (2019). https://doi.org/10.1016/j.mattod.2019.08.008.

[41] Y. Liu, T. Zhao, W. Ju, S. Shi, Materials discovery and design using machine learning, J. Mater. 3 (2017) 159–177. https://doi.org/https://doi.org/10.1016/j.jmat.2017.08.002.

[42] F. Ren, L. Ward, T. Williams, K.J. Laws, C. Wolverton, J. Hattrick-Simpers, A. Mehta, Accelerated discovery of metallic glasses through iteration of machine learning and high-throughput experiments, Sci. Adv. 4 (2018) eaaq1566. https://doi.org/10.1126/sciadv.aaq1566.

[43] R. Ramprasad, R. Batra, G. Pilania, A. Mannodi-Kanakkithodi, C. Kim, Machine learning in materials informatics: recent applications and prospects, Npj Comput. Mater. 3 (2017) 54. https://doi.org/10.1038/s41524-017-0056-5.

[44] L. Ward, A. Agrawal, A. Choudhary, C. Wolverton, A general-purpose machine learning framework for predicting properties of inorganic materials, Npj Comput. Mater. 2 (2016) 16028. https://doi.org/10.1038/npjcompumats.2016.28.

[45] Y. Liu, T. Zhao, W. Ju, S. Shi, S. Shi, S. Shi, Materials discovery and design using machine learning, J. Mater. 3 (2017) 159–177. https://doi.org/10.1016/j.jmat.2017.08.002.

[46] D.J. Walters, A. Biswas, E.C. Lawrence, D.C. Francom, D.J. Luscher, D.A. Fredenburg, K.R. Moran, C.M. Sweeney, R.L. Sandberg, J.P. Ahrens, Bayesian calibration of strength parameters using hydrocode simulations of symmetric impact shock experiments of Al-5083, J. Appl. Phys. 124 (2018) 205105.

[47] Y. Ling, J. Mullins, S. Mahadevan, Selection of model discrepancy priors in Bayesian calibration, J. Comput. Phys. 276 (2014) 665–680. https://doi.org/https://doi.org/10.1016/j.jcp.2014.08.005.

[48] A. Raza, K.M. Deen, R. Jaafreh, K. Hamad, A. Haider, W. Haider, Incorporation of machine learning in additive manufacturing: a review, Int. J. Adv. Manuf. Technol. (2022) 1–24.

[49] R. Cang, H. Yao, Y. Ren, One-shot generation of near-optimal topology through theory-driven machine learning, Comput. Des. 109 (2019) 12–21. https://doi.org/https://doi.org/10.1016/j.cad.2018.12.008.

[50] J.H. Martin, B.D. Yahata, J.M. Hundley, J.A. Mayer, T.A. Schaedler, T.M. Pollock, 3D printing of high-strength aluminium alloys, Nature. 549 (2017) 365–369.

[51] G. Tapia, S. Khairallah, M. Matthews, W.E. King, A. Elwany, Gaussian process-based surrogate modeling framework for process planning in laser powder-bed fusion additive manufacturing of 316L stainless steel, Int. J. Adv. Manuf. Technol. 94 (2018) 3591–3603. https://doi.org/10.1007/s00170-017-1045-z.

[52] J. Munguía, J. Ciurana, C. Riba, Neural-network-based model for build-time estimation in selective laser sintering, Proc. Inst. Mech. Eng. Part B J. Eng. Manuf. 223 (2009) 995–1003.

[53] L.D. Bobbio, R.A. Otis, J.P. Borgonia, R.P. Dillon, A.A. Shapiro, Z.-K. Liu, A.M. Beese, Additive manufacturing of a functionally graded material from Ti-6Al-4V to Invar: experimental characterization and thermodynamic calculations, Acta Mater. 127 (2017) 133–142. https://doi.org/10.1016/j.actamat.2016.12.070.

[54] A. Hope, P. Mason, Applying computational thermodynamics to additive manufacturing, MRS Bull. 44 (2019) 156–157. https://doi.org/10.1557/mrs.2019.48.

[55] W.E. Frazier, Metal additive manufacturing: A review, J. Mater. Eng. Perform. 23 (2014) 1917–1928. https://doi.org/10.1007/s11665-014-0958-z.

[56] Z. Hu, S. Mahadevan, Uncertainty quantification in prediction of material properties during additive manufacturing, Scr. Mater. 135 (2017) 135–140. https://doi.org/10.1016/j.scriptamat.2016.10.014.

[57] D.S. Thomas, S.W. Gilbert, Costs and cost effectiveness of additive manufacturing, NIST Spec. Publ. 1176 (2014) 12.

[58] A. Bandyopadhyay, K.D. Traxel, M. Lang, M. Juhasz, N. Eliaz, S. Bose, Alloy design via additive manufacturing: Advantages, challenges, applications and perspectives, Mater. Today. (2022).

[59] A.T. Clare, R.S. Mishra, M. Merklein, H. Tan, I. Todd, L. Chechik, J. Li, M. Bambach, Alloy design and adaptation for additive manufacture, J. Mater. Process. Technol. 299 (2022) 117358.

[60] G. Bi, C.N. Sun, A. Gasser, Study on influential factors for process monitoring and control in laser aided additive manufacturing, J. Mater. Process. Technol. 213 (2013) 463–468.

[61] J.A. Slotwinski, E.J. Garboczi, P.E. Stutzman, C.F. Ferraris, S.S. Watson, M.A. Peltz,

Characterization of metal powders used for additive manufacturing, J. Res. Natl. Inst. Stand. Technol. 119 (2014) 460–493. https://doi.org/10.6028/jres.119.018.

[62] A. Strondl, O. Lyckfeldt, H. Brodin, U. Ackelid, Characterization and control of powder properties for additive manufacturing, Jom. 67 (2015) 549–554.

[63] W.J. Sames, F.A. List, S. Pannala, R.R. Dehoff, S.S. Babu, The metallurgy and processing science of metal additive manufacturing, Int. Mater. Rev. 61 (2016) 315–360. https://doi.org/10.1080/09506608.2015.1116649.

[64] J. Dawes, R. Bowerman, R. Trepleton, Introduction to the additive manufacturing powder metallurgy supply chain, Johnson Matthey Technol. Rev. 59 (2015) 243–256. https://doi.org/10.1595/205651315X688686.

[65] W. Li, X. Chen, L. Yan, J. Zhang, X. Zhang, F. Liou, Additive manufacturing of a new Fe-Cr-Ni alloy with gradually changing compositions with elemental powder mixes and thermodynamic calculation, Int. J. Adv. Manuf. Technol. 95 (2018) 1013–1023. https://doi.org/10.1007/s00170-017-1302-1.

[66] Y.-J. Liang, X.-J. Tian, Y.-Y. Zhu, J. Li, H.-M. Wang, Compositional variation and microstructural evolution in laser additive manufactured Ti/Ti–6Al–2Zr–1Mo–1V graded structural material, Mater. Sci. Eng. A. 599 (2014) 242–246. https://doi.org/10.1016/j.msea.2014.01.092.

[67] S. Sridar, Y. Zhao, K. Li, X. Wang, W. Xiong, Post-heat treatment design for high-strength low-alloy steels processed by laser powder bed fusion, Mater. Sci. Eng. A. (2020) 139531.

[68] S. Sridar, Y. Zhao, W. Xiong, Cyclic re-austenitization of copper-bearing high-strength low-alloy steels fabricated by laser powder bed fusion, Mater. Charact. 166 (2020) 110437. https://doi.org/https://doi.org/10.1016/j.matchar.2020.110437.

[69] N.J. Wengrenovich, G.B. Olson, Optimization of a TRIP steel for adiabatic fragment protection, Mater. Today Proc. 2 (2015) S639–S642. https://doi.org/10.1016/j.matpr.2015.07.365.

[70] X. Wang, S. Sridar, W. Xiong, Thermodynamic Investigation of New High-Strength Low-Alloy Steels with Heusler Phase Strengthening for Welding and Additive Manufacturing: High-Throughput CALPHAD Calculations and Key Experiments for Database Verification, J. Phase Equilibria Diffus. (2020). https://doi.org/https://doi.org/10.1007/s11669-020-00828-y.

[71] W.F. Savage, E.F. Nippes, E.S. Szekeres, Hydrogen induced cold cracking in a low alloy steel, Weld. J. 55 (1976) 275.

[72] Y. Chen, F. Lu, K. Zhang, P. Nie, S.R.E. Hosseini, K. Feng, Z. Li, Dendritic microstructure

and hot cracking of laser additive manufactured Inconel 718 under improved base cooling, J. Alloys Compd. 670 (2016) 312–321.

[73] M. Takahashi, H. Bhadeshia, Model for transition from upper to lower bainite, Mater. Sci. Technol. 6 (1990) 592–603. https://doi.org/10.1179/mst.1990.6.7.592.

[74] M. Hillert, Inhibition of grain growth by second-phase particles, Acta Metall. 36 (1988) 3177–3181. https://doi.org/10.1016/0001-6160(88)90053-3.

[75] E.I. Galindo-Nava, P.E.J. Rivera-Díaz-del-Castillo, A model for the microstructure behaviour and strength evolution in lath martensite, Acta Mater. 98 (2015) 81–93. https://doi.org/10.1016/j.actamat.2015.07.018.

[76] D. Bhattacharjee, J.F. Knott, C.L. Davis, Charpy-impact-toughness prediction using an "Effective" grain size for thermomechanically controlled rolled microalloyed steels, Metall. Mater. Trans. A. 35 (2004) 121–130. https://doi.org/10.1007/s11661-004-0115-7.

[77] B.A. Graville, Cold cracking in welds in HSLA steels. Welding of HSLA (microalloyed) structural steels, in: Proc. Int. Conf, 1976: pp. 85–101.

[78] A. Agrawal, A. Saboo, W. Xiong, G. Olson, A. Choudhary, Martensite Start Temperature Predictor for Steels Using Ensemble Data Mining, 2019 IEEE Int. Conf. Data Sci. Adv. Anal. (2019) 521–530.

[79] W. Xiong, G.B. Olson, Cybermaterials: materials by design and accelerated insertion of materials, NPJ Comput. Mater. 2 (2016) 15009. https://doi.org/10.1038/npjcompumats.2015.9.

[80] J. Zhao, Z. Jin, Isothermal decomposition of supercooled austenite in steels, Mater. Sci. Technol. 8 (1992) 1004–1010. https://doi.org/10.1179/mst.1992.8.11.1004.

[81] E.O. Hall, The deformation and ageing of mild steel: III discussion of results, Proc. Phys. Soc. Sect. B. 64 (1951) 747.

[82] N.J. Petch, The cleavage strength of polycrystals, J. Iron Steel Inst. 174 (1953) 25–28.

[83] K.C. Russell, L.M. Brown, A dispersion strengthening model based on differing elastic moduli applied to the iron-copper system, Acta Metall. 20 (1972) 969–974. https://doi.org/10.1016/0001-6160(72)90091-0.

[84] J.-S. Wang, M.D. Mulholland, G.B. Olson, D.N. Seidman, Prediction of the yield strength of a secondary-hardening steel, Acta Mater. 61 (2013) 4939–4952. https://doi.org/10.1016/j.actamat.2013.04.052.

[85] R.L. Fleischer, Substitutional solution hardening, Acta Metall. 11 (1963) 203–209.

https://doi.org/10.1016/0001-6160(63)90213-X.

[86] E.I. Galindo-Nava, W.M. Rainforth, P.E.J. Rivera-Díaz-del-Castillo, Predicting microstructure and strength of maraging steels: Elemental optimisation, Acta Mater. 117 (2016) 270–285. https://doi.org/10.1016/j.actamat.2016.07.020.

[87] B. Zheng, Y. Zhou, J.E. Smugeresky, J.M. Schoenung, E.J. Lavernia, Thermal behavior and microstructural evolution during laser deposition with laser-engineered net shaping: Part I. Numerical calculations, Metall. Mater. Trans. A. 39 (2008) 2228–2236.

[88] T. Vilaro, C. Colin, J.-D. Bartout, As-fabricated and heat-treated microstructures of the Ti-6Al-4V alloy processed by selective laser melting, Metall. Mater. Trans. A. 42 (2011) 3190–3199.

[89] B. Zheng, Y. Zhou, J.E. Smugeresky, J.M. Schoenung, E.J. Lavernia, Thermal behavior and microstructure evolution during laser deposition with laser-engineered net shaping: part II. Experimental investigation and discussion, Metall. Mater. Trans. A. 39 (2008) 2237–2245.

[90] H. Yin, M. Song, P. Deng, L. Li, B.C. Prorok, X. Lou, Thermal stability and microstructural evolution of additively manufactured 316L stainless steel by laser powder bed fusion at 500–800 ℃, Addit. Manuf. 41 (2021) 101981. https://doi.org/https://doi.org/10.1016/j.addma.2021.101981.

[91] A. Yadollahi, N. Shamsaei, S.M. Thompson, D.W. Seely, Effects of process time interval and heat treatment on the mechanical and microstructural properties of direct laser deposited 316L stainless steel, Mater. Sci. Eng. A. 644 (2015) 171–183.

[92] M. Ma, Z. Wang, X. Zeng, A comparison on metallurgical behaviors of 316L stainless steel by selective laser melting and laser cladding deposition, Mater. Sci. Eng. A. 685 (2017) 265–273.

[93] D.R. Steinmetz, T. Jäpel, B. Wietbrock, P. Eisenlohr, I. Gutierrez-Urrutia, A. Saeed–Akbari, T. Hickel, F. Roters, D. Raabe, Revealing the strain-hardening behavior of twinning-induced plasticity steels: Theory, simulations, experiments, Acta Mater. 61 (2013) 494–510. https://doi.org/https://doi.org/10.1016/j.actamat.2012.09.064.

[94] H. Kim, D.-W. Suh, N.J. Kim, Fe–Al–Mn–C lightweight structural alloys: a review on the microstructures and mechanical properties, Sci. Technol. Adv. Mater. 14 (2013) 14205.

[95] T.S. Byun, On the stress dependence of partial dislocation separation and deformation microstructure in austenitic stainless steels, Acta Mater. 51 (2003) 3063–3071.

[96] J. Su, D. Raabe, Z. Li, Hierarchical microstructure design to tune the mechanical behavior of an interstitial TRIP-TWIP high-entropy alloy, Acta Mater. 163 (2019) 40–54. https://doi.org/10.1016/j.actamat.2018.10.017.

[97] W. Woo, J.S. Jeong, D.-K. Kim, C.M. Lee, S.-H. Choi, J.-Y. Suh, S.Y. Lee, S. Harjo, T. Kawasaki, Stacking Fault Energy Analyses of Additively Manufactured Stainless Steel 316L and CrCoNi Medium Entropy Alloy Using In Situ Neutron Diffraction, Sci. Rep. 10 (2020) 1350. https://doi.org/10.1038/s41598-020-58273-3.

[98] J. Lu, L. Hultman, E. Holmström, K.H. Antonsson, M. Grehk, W. Li, L. Vitos, A. Golpayegani, Stacking fault energies in austenitic stainless steels, Acta Mater. 111 (2016) 39–46. https://doi.org/10.1016/j.actamat.2016.03.042.

[99] D.T. Pierce, J. Bentley, J.A. Jiménez, J.E. Wittig, Stacking fault energy measurements of Fe–Mn–Al–Si austenitic twinning-induced plasticity steels, Scr. Mater. 66 (2012) 753–756.

[100] G.R. Lehnhoff, K.O. Findley, B.C. De Cooman, The influence of silicon and aluminum alloying on the lattice parameter and stacking fault energy of austenitic steel, Scr. Mater. 92 (2014) 19–22. https://doi.org/10.1016/j.scriptamat.2014.07.019.

[101] J. Kim, B.C. De Cooman, On the stacking fault energy of Fe-18 Pct Mn-0.6 Pct C-1.5 Pct Al twinning-induced plasticity steel, Metall. Mater. Trans. A. 42 (2011) 932–936.

[102] T.H. Lee, E. Shin, C.S. Oh, H.Y. Ha, S.J. Kim, Correlation between stacking fault energy and deformation microstructure in high-interstitial-alloyed austenitic steels, Acta Mater. 58 (2010) 3173–3186. https://doi.org/10.1016/j.actamat.2010.01.056.

[103] B. Cantor, I.T.H. Chang, P. Knight, A.J.B. Vincent, Microstructural development in equiatomic multicomponent alloys, Mater. Sci. Eng. A. 375 (2004) 213–218.

[104] P. Nath, Z. Hu, S. Mahadevan, Sensor placement for calibration of spatially varying model parameters, J. Comput. Phys. 343 (2017) 150–169.

[105] Z. Hu, D. Ao, S. Mahadevan, Calibration experimental design considering field response and model uncertainty, Comput. Methods Appl. Mech. Eng. 318 (2017) 92–119.

[106] M.C. Kennedy, A. O'Hagan, Bayesian calibration of computer models, J. R. Stat. Soc. Ser. B (Statistical Methodol. 63 (2001) 425–464.

[107] B.H. Jared, M.A. Aguilo, L.L. Beghini, B.L. Boyce, B.W. Clark, A. Cook, B.J. Kaehr, J. Robbins, Additive manufacturing: Toward holistic design, Scr. Mater. 135 (2017) 141–147. https://doi.org/10.1016/j.scriptamat.2017.02.029.

[108] L. Kaufman, H. Bernstein, Computer calculation of phase diagrams. With special reference to refractory metals, (1970).

[109] Thermo-Calc Software TCFE9 Steels/Fe-alloys database (accessed 2020), (n.d.).

[110] J.-O. Andersson, T. Helander, L. Höglund, P. Shi, B. Sundman, Thermo-Calc & DICTRA,

computational tools for materials science, Calphad. 26 (2002) 273–312. https://doi.org/https://doi.org/10.1016/s0364-5916(02)00037-8.

[111] K.J. Millman, M. Aivazis, Python for scientists and engineers, Comput. Sci. Eng. 13 (2011) 9–12. https://doi.org/10.1109/MCSE.2011.36.

[112] R. Kohavi, A study of cross-validation and bootstrap for accuracy estimation and model selection, in: Ijcai, Montreal, Canada, 1995: pp. 1137–1145.

[113] F. Pedregosa, G. Varoquaux, A. Gramfort, V. Michel, B. Thirion, O. Grisel, M. Blondel, P. Prettenhofer, R. Weiss, V. Dubourg, Scikit-learn: Machine learning in Python, J. Mach. Learn. Res. 12 (2011) 2825–2830.

[114] S.M. Lundberg, S.-I. Lee, A unified approach to interpreting model predictions, Adv. Neural Inf. Process. Syst. 30 (2017).

[115] M. Baudin, A. Dutfoy, B. Iooss, A.-L. Popelin, Openturns: An industrial software for uncertainty quantification in simulation, in: Handb. Uncertain. Quantif., Springer, 2017: pp. 2001–2038.

[116] E. ASTM, Standard test methods for tension testing of metallic materials, Annu. B. ASTM Stand. ASTM. (2001).

[117] G.B. Olson, Computational design of hierarchically structured materials, Science (80-.). 277 (1997) 1237–1242. https://doi.org/10.1126/science.277.5330.1237.

[118] G. Sander, J. Tan, P. Balan, O. Gharbi, D.R. Feenstra, L. Singer, S. Thomas, R.G. Kelly, J.R. Scully, N. Birbilis, Corrosion of additively manufactured alloys: a review, Corrosion. 74 (2018) 1318–1350. https://doi.org/10.5006/2926.

[119] D. Jain, D. Isheim, D.N. Seidman, Carbon redistribution and carbide precipitation in a high-strength low-carbon HSLA-115 steel studied on a nanoscale by atom probe tomography, Metall. Mater. Trans. A. 48 (2017) 3205–3219. https://doi.org/10.1007/s11661-017-4129-3.

[120] H. Bhadeshia, R. Honeycombe, Steels: microstructure and properties, Butterworth-Heinemann, 2017.

[121] S. Kim, C. Lee, Behavior of Cu precipitates during thermo-mechanical cycling in the weld CGHAZ of Cu-containing HSLA steel, Met. Mater. Int. 18 (2012) 857–862.

[122] U.F. Kocks, The relation between polycrystal deformation and single-crystal deformation, Metall. Mater. Trans. B. 1 (1970) 1121–1143.

[123] S.A. Kim, W.L. Johnson, Elastic constants and internal friction of martensitic steel, ferritic-

pearlitic steel, and α-iron, Mater. Sci. Eng. A. 452 (2007) 633–639. https://doi.org/https://doi.org/10.1016/j.msea.2006.11.147.

[124] F. Christien, M.T.F. Telling, K.S. Knight, Neutron diffraction in situ monitoring of the dislocation density during martensitic transformation in a stainless steel, Scr. Mater. 68 (2013) 506–509. https://doi.org/https://doi.org/10.1016/j.scriptamat.2012.11.031.

[125] M. Grujicic, J.S. Snipes, S. Ramaswami, Application of the Materials-by-Design Methodology to Redesign a New Grade of the High-Strength Low-Alloy Class of Steels with Improved Mechanical Properties and Processability, J. Mater. Eng. Perform. 25 (2016) 165–178. https://doi.org/10.1007/s11665-015-1812-7.

[126] D. Jain, D. Isheim, A.H. Hunter, D.N. Seidman, Multicomponent high-strength low-alloy steel precipitation-strengthened by sub-nanometric Cu precipitates and M2C carbides, Metall. Mater. Trans. A. 47 (2016) 3860–3872. https://doi.org/10.1007/s11661-016-3569-5.

[127] L.A. Gypen, Ajj. Deruyttere, Multi-component solid solution hardening, J. Mater. Sci. 12 (1977) 1028–1033. https://doi.org/10.1007/BF00540987.

[128] J. Takahashi, K. Kawakami, Y. Kobayashi, Consideration of particle-strengthening mechanism of copper-precipitation-strengthened steels by atom probe tomography analysis, Mater. Sci. Eng. A. 535 (2012) 144–152. https://doi.org/10.1016/j.msea.2011.12.056Get.

[129] H.J. Kong, C. Xu, C.C. Bu, C. Da, J.H. Luan, Z.B. Jiao, G. Chen, C.T. Liu, Hardening mechanisms and impact toughening of a high-strength steel containing low Ni and Cu additions, Acta Mater. 172 (2019) 150–160. https://doi.org/10.1016/j.actamat.2019.04.041.

[130] V. Mohles, Simulations of dislocation glide in overaged precipitation-hardened crystals, Philos. Mag. A. 81 (2001) 971–990. https://doi.org/10.1080/01418610108214330.

[131] S. Takaki, K. Kawasaki, Y. Kimura, Mechanical properties of ultra fine grained steels, J. Mater. Process. Technol. 117 (2001) 359–363. https://doi.org/10.1016/S0924-0136(01)00797-X.

[132] Y. Tomita, K. Okabayashi, Mechanical properties of 0.40 pct C-Ni-Cr-Mo high strength steel having a mixed structure of martensite and bainite, Metall. Trans. A. 16 (1985) 73–82. https://doi.org/10.1007/BF02656714.

[133] K.-T. Park, H.-J. Kwon, Interpretation of the strengthening of steel with lower bainite and martensite mixed microstructure, Met. Mater. Int. 7 (2001) 95–99. https://doi.org/10.1007/BF03026946.

[134] R. Varughese, P.R. Howell, The application of metallographic techniques to the study of the tempering of HSLA-100 steel, Mater. Charact. 30 (1993) 261–267.

https://doi.org/10.1016/1044-5803(93)90073-5.

[135] S.K. Dhua, S.K. Sen, Effect of direct quenching on the microstructure and mechanical properties of the lean-chemistry HSLA-100 steel plates, Mater. Sci. Eng. A. 528 (2011) 6356–6365. https://doi.org/10.1016/j.msea.2011.04.084.

[136] G.H. Majzoobi, A.H. Mahmoudi, S. Moradi, Ductile to brittle failure transition of HSLA-100 Steel at high strain rates and subzero temperatures, Eng. Fract. Mech. 158 (2016) 179–193. https://doi.org/10.1016/j.engfracmech.2016.03.001.

[137] J. Du, M. Strangwood, C.L. Davis, Effect of TiN particles and grain size on the charpy impact transition temperature in steels, J. Mater. Sci. Technol. 28 (2012) 878–888. https://doi.org/10.1016/S1005-0302(12)60146-7.

[138] J. Mendez, M. Ghoreshy, W.B.F. Mackay, T.J.N. Smith, R.W. Smith, Weldability of austenitic manganese steel, J. Mater. Process. Technol. 153 (2004) 596–602. https://doi.org/10.1016/j.jmatprotec.2004.04.033.

[139] Y.D. Chung, H. Fujii, R. Ueji, N. Tsuji, Friction stir welding of high carbon steel with excellent toughness and ductility, Scr. Mater. 63 (2010) 223–226. https://doi.org/10.1016/j.scriptamat.2010.03.060.

[140] A. Piglione, B. Dovgyy, C. Liu, C.M. Gourlay, P.A. Hooper, M.S. Pham, Printability and microstructure of the CoCrFeMnNi high-entropy alloy fabricated by laser powder bed fusion, Mater. Lett. 224 (2018) 22–25. https://doi.org/10.1016/j.matlet.2018.04.052.

[141] Z. Wu, S.A. David, Z. Feng, H. Bei, Weldability of a high entropy CrMnFeCoNi alloy, Scr. Mater. 124 (2016) 81–85. https://doi.org/10.1016/j.scriptamat.2016.06.046.

[142] J.L. Caron, Weldability evaluation of naval steels, (2010).

[143] J.C. Helton, F.J. Davis, Latin hypercube sampling and the propagation of uncertainty in analyses of complex systems, Reliab. Eng. Syst. Saf. 81 (2003) 23–69.

[144] S.K. Das, S. Chatterjee, S. Tarafder, Effect of microstructures on deformation behaviour of high-strength low-alloy steel, J. Mater. Sci. 44 (2009) 1094–1100. https://doi.org/10.1007/s10853-008-3106-z.

[145] A. Saha, G.B. Olson, Computer-aided design of transformation toughened blast resistant naval hull steels: Part I, J. Comput. Mater. Des. 14 (2007) 177–200. https://doi.org/10.1007/s10820-006-9031-z.

[146] Z. Wang, P. Liu, Y. Xiao, X. Cui, Z. Hu, L. Chen, A Data-Driven Approach for Process Optimization of Metallic Additive Manufacturing Under Uncertainty, J. Manuf. Sci. Eng. 141 (2019). https://doi.org/10.1115/1.4043798.

[147] D.R. Jones, M. Schonlau, W.J. Welch, Efficient global optimization of expensive black-box functions, J. Glob. Optim. 13 (1998) 455–492.

[148] J.H. Friedman, Greedy function approximation: a gradient boosting machine, Ann. Stat. 29 (2001) 1189–1232. https://doi.org/10.1214/aos/1013203451.

[149] X. Wang, W. Xiong, Stacking fault energy prediction for austenitic steels: thermodynamic modeling vs. machine learning, Sci. Technol. Adv. Mater. 21 (2020) 626–634. https://doi.org/10.1080/14686996.2020.1808433.

[150] C. Spearman, The proof and measurement of association between two things., Am. J. Psychol. 15 (1904) 72–101.

[151] H. Akoglu, User's guide to correlation coefficients, Turkish J. Emerg. Med. 18 (2018) 91–93.

[152] S. Kokoska, D. Zwillinger, CRC standard probability and statistics tables and formulae, Crc Press, 2000.

[153] I.M. Sobol, Global sensitivity indices for nonlinear mathematical models and their Monte Carlo estimates, Math. Comput. Simul. 55 (2001) 271–280.

[154] J. Herman, W. Usher, SALib: an open-source Python library for sensitivity analysis, J. Open Source Softw. 2 (2017) 97.

[155] A. Haldar, S. Mahadevan, Probability, reliability, and statistical methods in engineering design, John Wiley, 2000.

[156] D. Shin, Y. Yamamoto, M.P. Brady, S. Lee, J.A. Haynes, Modern data analytics approach to predict creep of high-temperature alloys, Acta Mater. 168 (2019) 321–330. https://doi.org/10.1016/j.actamat.2019.02.017.

[157] C. Shen, C. Wang, X. Wei, Y. Li, S. van der Zwaag, W. Xu, Physical metallurgy-guided machine learning and artificial intelligent design of ultrahigh-strength stainless steel, Acta Mater. 179 (2019) 201–214. https://doi.org/10.1016/j.actamat.2019.08.033.

[158] C. Qiu, C. Panwisawas, M. Ward, H.C. Basoalto, J.W. Brooks, M.M. Attallah, On the role of melt flow into the surface structure and porosity development during selective laser melting, Acta Mater. 96 (2015) 72–79.

[159] X. Lu, X. Lin, M. Chiumenti, M. Cervera, Y. Hu, X. Ji, L. Ma, H. Yang, W. Huang, Residual stress and distortion of rectangular and S-shaped Ti-6Al-4V parts by Directed Energy Deposition: modelling and experimental calibration, Addit. Manuf. 26 (2019) 166–179.

[160] S. Sankararaman, Y. Ling, S. Mahadevan, Uncertainty quantification and model validation

of fatigue crack growth prediction, Eng. Fract. Mech. 78 (2011) 1487–1504.

[161] J.D. Robson, Modelling the evolution of particle size distribution during nucleation, growth and coarsening, Mater. Sci. Technol. 20 (2004) 441–448.

[162] E.I. Galindo-Nava, L.D. Connor, C.M.F. Rae, On the prediction of the yield stress of unimodal and multimodal γ′ Nickel-base superalloys, Acta Mater. 98 (2015) 377–390. https://doi.org/https://doi.org/10.1016/j.actamat.2015.07.048.

[163] J. Ning, D.E. Sievers, H. Garmestani, S.Y. Liang, Analytical modeling of part porosity in metal additive manufacturing, Int. J. Mech. Sci. 172 (2020) 105428. https://doi.org/https://doi.org/10.1016/j.ijmecsci.2020.105428.

[164] R.E. Schramm, R.P. Reed, Stacking fault energies of seven commercial austenitic stainless steels, Metall. Trans. A. 6 (1975) 1345.

[165] C.G. Rhodes, A.W. Thompson, The composition dependence of stacking fault energy in austenitic stainless steels, Metall. Trans. A. 8 (1977) 1901–1906.

[166] P.J. Brofman, G.S. Ansell, On the effect of carbon on the stacking fault energy of austenitic stainless steels, Metall. Mater. Trans. A. 9 (1978) 879–880.

[167] M. Ojima, Y. Adachi, Y. Tomota, Y. Katada, Y. Kaneko, K. Kuroda, H. Saka, Weak beam TEM study on stacking fault energy of high nitrogen steels, Steel Res. Int. 80 (2009) 477–481.

[168] T. Yonezawa, K. Suzuki, S. Ooki, A. Hashimoto, The effect of chemical composition and heat treatment conditions on stacking fault energy for Fe-Cr-Ni austenitic stainless steel, Metall. Mater. Trans. A. 44 (2013) 5884–5896.

[169] G.M. de Bellefon, J.C. van Duysen, K. Sridharan, Composition-dependence of stacking fault energy in austenitic stainless steels through linear regression with random intercepts, J. Nucl. Mater. 492 (2017) 227–230.

[170] G.B. Olson, M. Cohen, A general mechanism of martensitic nucleation: Part I. General concepts and the FCC→ HCP transformation, Metall. Trans. A. 7 (1976) 1897–1904.

[171] S. Curtze, V.-T. Kuokkala, Dependence of tensile deformation behavior of TWIP steels on stacking fault energy, temperature and strain rate, Acta Mater. 58 (2010) 5129–5141.

[172] S.-J. Lee, Y. Sun, H. Fujii, Stacking-fault energy, mechanical twinning and strain hardening of Fe-18Mn-0.6 C-(0, 1.5) Al twinning-induced plasticity steels during friction stir welding, Acta Mater. 148 (2018) 235–248.

[173] A. Saeed-Akbari, J. Imlau, U. Prahl, W. Bleck, Derivation and variation in composition-

dependent stacking fault energy maps based on subregular solution model in high-manganese steels, Metall. Mater. Trans. A Phys. Metall. Mater. Sci. 40 (2009) 3076–3090. https://doi.org/10.1007/s11661-009-0050-8.

[174] D.T. Pierce, J.A. Jiménez, J. Bentley, D. Raabe, C. Oskay, J.E. Wittig, The influence of manganese content on the stacking fault and austenite/ε-martensite interfacial energies in Fe-Mn-(Al-Si) steels investigated by experiment and theory, Acta Mater. 68 (2014) 238–253. https://doi.org/10.1016/j.actamat.2014.01.001.

[175] S. Curtze, V.-T.T. Kuokkala, A. Oikari, J. Talonen, H. Hänninen, Thermodynamic modeling of the stacking fault energy of austenitic steels, Acta Mater. 59 (2011) 1068–1076. https://doi.org/10.1016/j.actamat.2010.10.037.

[176] L. Mosecker, A. Saeed-Akbari, Nitrogen in chromium-manganese stainless steels: A review on the evaluation of stacking fault energy by computational thermodynamics, Sci. Technol. Adv. Mater. 14 (2013) 033001. https://doi.org/10.1088/1468-6996/14/3/033001.

[177] S. Allain, J.-P. Chateau, O. Bouaziz, S. Migot, N. Guelton, Correlations between the calculated stacking fault energy and the plasticity mechanisms in Fe–Mn–C alloys, Mater. Sci. Eng. A. 387 (2004) 158–162.

[178] S.M. Cotes, A.F. Guillermet, M. Sade, Fcc/Hcp martensitic transformation in the Fe-Mn system: Part II. Driving force and thermodynamics of the nucleation process, Metall. Mater. Trans. A. 35 (2004) 83–91.

[179] P.U. Volosevich, V.N. Gridnev, Y.U.N. Petrov, Influence of Mn and the stacking fault energy of Fe-Mn alloys, Phys. Met. Met. 42 (1976) 126–130.

[180] Q. Chen, B. Sundman, Modeling of thermodynamic properties for Bcc, Fcc, liquid, and amorphous iron, J. Phase Equilibria. 22 (2001) 631–644.

[181] W. Xiong, P. Hedström, M. Selleby, J. Odqvist, M. Thuvander, Q. Chen, An improved thermodynamic modeling of the Fe–Cr system down to zero kelvin coupled with key experiments, Calphad. 35 (2011) 355–366.

[182] W. Xiong, H. Zhang, L. Vitos, M. Selleby, Magnetic phase diagram of the Fe–Ni system, Acta Mater. 59 (2011) 521–530.

[183] W. Xiong, Q. Chen, P.A. Korzhavyi, M. Selleby, An improved magnetic model for thermodynamic modeling, Calphad. 39 (2012) 11–20.

[184] L. Vitos, J.-O. Nilsson, B. Johansson, Alloying effects on the stacking fault energy in austenitic stainless steels from first-principles theory, Acta Mater. 54 (2006) 3821–3826.

[185] S. Huang, W. Li, S. Lu, F. Tian, J. Shen, E. Holmström, L. Vitos, Temperature dependent

stacking fault energy of FeCrCoNiMn high entropy alloy, Scr. Mater. 108 (2015) 44–47. https://doi.org/10.1016/j.scriptamat.2015.05.041.

[186] X. Wu, Z. Li, Z. Rao, Y. Ikeda, B. Dutta, F. Körmann, J. Neugebauer, D. Raabe, Role of magnetic ordering for the design of quinary TWIP-TRIP high entropy alloys, Phys. Rev. Mater. 4 (2020) 33601. https://doi.org/10.1103/PhysRevMaterials.4.033601.

[187] D. Wei, X. Li, J. Jiang, W. Heng, Y. Koizumi, W.-M. Choi, B.-J. Lee, H.S. Kim, H. Kato, A. Chiba, Novel Co-rich high performance twinning-induced plasticity (TWIP) and transformation-induced plasticity (TRIP) high-entropy alloys, Scr. Mater. 165 (2019) 39–43.

[188] S. Kibey, J.B. Liu, M.J. Curtis, D.D. Johnson, H. Sehitoglu, Effect of nitrogen on generalized stacking fault energy and stacking fault widths in high nitrogen steels, Acta Mater. 54 (2006) 2991–3001. https://doi.org/https://doi.org/10.1016/j.actamat.2006.02.048.

[189] X. Sun, S. Lu, R. Xie, X. An, W. Li, T. Zhang, C. Liang, X. Ding, Y. Wang, H. Zhang, Can experiment determine the stacking fault energy of metastable alloys?, Mater. Des. 199 (2021) 109396.

[190] Y. Iwasaki, M. Ishida, M. Shirane, Predicting material properties by integrating high-throughput experiments, high-throughput ab-initio calculations, and machine learning, Sci. Technol. Adv. Mater. (2019).

[191] S. Pruksawan, G. Lambard, S. Samitsu, K. Sodeyama, M. Naito, Prediction and optimization of epoxy adhesive strength from a small dataset through active learning, Sci. Technol. Adv. Mater. 20 (2019) 1010–1021.

[192] A. Das, Revisiting Stacking Fault Energy of Steels, Metall. Mater. Trans. A Phys. Metall. Mater. Sci. 47 (2016) 748–768. https://doi.org/10.1007/s11661-015-3266-9.

[193] N. Chaudhary, A. Abu-Odeh, I. Karaman, R. Arróyave, A data-driven machine learning approach to predicting stacking faulting energy in austenitic steels, J. Mater. Sci. 52 (2017) 11048–11076. https://doi.org/10.1007/s10853-017-1252-x.

[194] S. Tian, X. Zhu, J. Wu, H. Yu, D. Shu, B. Qian, Influence of temperature on stacking fault energy and creep mechanism of a single crystal nickel-based superalloy, J. Mater. Sci. Technol. 32 (2016) 790–798.

[195] S. Kibey, J.B. Liu, D.D. Johnson, H. Sehitoglu, Predicting twinning stress in fcc metals: Linking twin-energy pathways to twin nucleation, Acta Mater. 55 (2007) 6843–6851.

[196] G.M. de Bellefon, M.N. Gussev, A.D. Stoica, J.C. van Duysen, K. Sridharan, G. Meric de Bellefon, M.N. Gussev, A.D. Stoica, J.C. van Duysen, K. Sridharan, Examining the influence of stacking fault width on deformation twinning in an austenitic stainless steel,

Scr. Mater. 157 (2018) 162–166. https://doi.org/https://doi.org/10.1016/j.scriptamat.2018.08.012.

[197] F. Abrassart, Stress-induced γ→ α martensitic transformation in two carbon stainless steels. Application to trip steels, Metall. Trans. 4 (1973) 2205–2216.

[198] C.C. Bampton, I.P. Jones, M.H. Loretto, Stacking fault energy measurements in some austenitic stainless steels, Acta Metall. 26 (1978) 39–51.

[199] P. Behjati, A. Najafizadeh, Role of chemical driving force in martensitic transformations of high-purity Fe-Cr-Ni alloys, Metall. Mater. Trans. A. 42 (2011) 3752.

[200] J.T. Benzing, W.A. Poling, D.T. Pierce, J. Bentley, K.O. Findley, D. Raabe, J.E. Wittig, Effects of strain rate on mechanical properties and deformation behavior of an austenitic Fe-25Mn-3Al-3Si TWIP-TRIP steel, Mater. Sci. Eng. A. 711 (2018) 78–92.

[201] L. Bracke, J. Penning, N. Akdut, The influence of Cr and N additions on the mechanical properties of FeMnC steels, Metall. Mater. Trans. A. 38 (2007) 520–528.

[202] D. Dulieu, Metallurgical Developments in High-Alloy-Steels, Spec. Rep. 86 (1964) 140.

[203] R. Fawley, M.A. Quader, R.A. Dodd, Compositional effects on the deformation modes, annealing twin frequencies, and stacking fault energies of austenitic stainless steels, Trans. Met. Soc. AIME. 242 (1968) 771–776.

[204] V. Gavriljuk, Y. Petrov, B. Shanina, Effect of nitrogen on the electron structure and stacking fault energy in austenitic steels, Scr. Mater. 55 (2006) 537–540.

[205] V.G. Gavriljuk, A.L. Sozinov, J. Foct, J.N. Petrov, Y.A. Polushkin, Effect of nitrogen on the temperature dependence of the yield strength of austenitic steels, Acta Mater. 46 (1998) 1157–1163.

[206] H. Idrissi, K. Renard, L. Ryelandt, D. Schryvers, P.J. Jacques, On the mechanism of twin formation in Fe–Mn–C TWIP steels, Acta Mater. 58 (2010) 2464–2476.

[207] L.G. Martinez, K. Imakuma, A.F. Padilha, Influence of niobium on stacking-fault energy of all-austenite stainless steels, Steel Res. 63 (1992) 221–223.

[208] K. Jeong, J.E. Jin, Y.S. Jung, S. Kang, Y.K. Lee, The effects of Si on the mechanical twinning and strain hardening of Fe-18Mn-0.6C twinning-induced plasticity steel, Acta Mater. 61 (2013) 3399–3410. https://doi.org/10.1016/j.actamat.2013.02.031.

[209] Z. Jiao, G.S. Was, The role of irradiated microstructure in the localized deformation of austenitic stainless steels, J. Nucl. Mater. 407 (2010) 34–43.

[210] M. Kang, W. Woo, Y.-K. Lee, B.-S. Seong, Neutron diffraction analysis of stacking fault

energy in Fe–18Mn–2Al–0.6 C twinning-induced plasticity steels, Mater. Lett. 76 (2012) 93–95.

[211] J. Kim, S.-J. Lee, B.C. De Cooman, Effect of Al on the stacking fault energy of Fe–18Mn–0.6 C twinning-induced plasticity, Scr. Mater. 65 (2011) 363–366.

[212] R.M. Latanision, A.W. Ruff, The temperature dependence of stacking fault energy in Fe-Cr-Ni alloys, Metall. Trans. 2 (1971) 505–509.

[213] F. Lecroisey, B. Thomas, On the variation of the intrinsic stacking fault energy with temperature in Fe-18 Cr-12 Ni alloys, Phys. Status Solidi. 2 (1970) K217–K220.

[214] F. Lecroisey, A. Pineau, Martensitic transformations induced by plastic deformation in the Fe-Ni-Cr-C system, Metall. Mater. Trans. B. 3 (1972) 391–400.

[215] T.-H. Lee, H.-Y. Ha, B. Hwang, S.-J. Kim, E. Shin, Effect of Carbon Fraction on Stacking Fault Energy of Austenitic Stainless Steels, Metall. Mater. Trans. A. 43 (2012) 4455–4459. https://doi.org/10.1007/s11661-012-1423-y.

[216] S.J. Lee, Y.S. Jung, S. Il Baik, Y.W. Kim, M. Kang, W. Woo, Y.K. Lee, The effect of nitrogen on the stacking fault energy in Fe-15Mn-2Cr-0.6C-xN twinning-induced plasticity steels, Scr. Mater. 92 (2014) 23–26. https://doi.org/10.1016/j.scriptamat.2014.08.004.

[217] J.C. Li, W. Zheng, Q. Jiang, Stacking fault energy of iron-base shape memory alloys, Mater. Lett. 38 (1999) 275–277.

[218] X. Li, A. Almazouzi, Deformation and microstructure of neutron irradiated stainless steels with different stacking fault energy, J. Nucl. Mater. 385 (2009) 329–333.

[219] L. Mosecker, D.T. Pierce, A. Schwedt, M. Beighmohamadi, J. Mayer, W. Bleck, J.E. Wittig, Temperature effect on deformation mechanisms and mechanical properties of a high manganese C+ N alloyed austenitic stainless steel, Mater. Sci. Eng. A. 642 (2015) 71–83.

[220] L. Mujica, S. Weber, W. Theisen, The Stacking Fault Energy and its Dependence on the Interstitial Content in Various Austenitic Steels, Mater. Sci. Forum. 706–709 (2012) 2193–2198. https://doi.org/10.4028/www.scientific.net/MSF.706-709.2193.

[221] Y.N. Petrov, EFFECT OF ALLOYING ON THE STACKING-FAULT ENERGY OF AUSTENITE IN STEELS, Phys. Met. 6 (1985) 735–741.

[222] Y.N. Petrov Kiev, On the carbon distribution at structural imperfections in manganese austenite, Scr. Metall. Mater. 29 (1993) 1471–1476. https://doi.org/10.1016/0956-716X(93)90339-T.

[223] Y.N. Petrov, Effect of carbon and nitrogen on the stacking fault energy of high-alloyed iron-

based austenite, Zeitschrift Für Met. 94 (2003) 1012–1016.

[224] Y. Petrov, Surface structure of different interstitial austenitic steels after impact wear, Int. J. Mater. Res. 103 (2012) 551–553.

[225] D. Rafaja, C. Krbetschek, C. Ullrich, S. Martin, Stacking fault energy in austenitic steels determined by using in situ X-ray diffraction during bending, J. Appl. Crystallogr. 47 (2014) 936–947.

[226] W. Reick, M. Pohl, A.F. Padilha, Recrystallization–transformation combined reactions during annealing of a cold rolled ferritic–austenitic duplex stainless steel, ISIJ Int. 38 (1998) 567–571.

[227] L. Rémy, A. Pineau, B. Thomas, Temperature dependence of stacking fault energy in close-packed metals and alloys, Mater. Sci. Eng. 36 (1978) 47–63.

[228] G.S. Shin, J.Y. Yun, M.C. Park, S.J. Kim, Effect of Mechanical Properties on Cavitation Erosion Resistance in $\gamma \rightarrow \alpha'$ Phase Transformable Fe–Cr–C–Mn Alloys, Tribol. Lett. 57 (2015) 25.

[229] J.M. Silcock, Nucleation and Growth of Stress Corrosion Cracks in Austenitic Steels with Varying Ni and Mo Contents, Corrosion. 38 (1982) 144–156.

[230] R.E. Stoltz, J.B. Vander Sande, The effect of nitrogen on stacking fault energy of Fe-Ni-Cr-Mn steels, Metall. Trans. A. 11 (1980) 1033–1037.

[231] J.R. Strife, M.J. Carr, G.S. Ansell, The effect of austenite prestrain above the M d temperature on the martensitic transformation in Fe-Ni-Cr-C alloys, Metall. Trans. A. 8 (1977) 1471–1484.

[232] P.R. Swann, Dislocation substructure vs transgranular stress corrosion susceptibility of single phase alloys, Corrosion. 19 (1963) 102t-114t.

[233] R. Taillard and J. Foct, Mechanisms of the action of nitrogen interstitials upon low cycle fatigue behaviour of 316 stainless steels, in: A. Hendry (Eds.), High Nitrogen Steels, HNS 88, Inst. Met. London, 1988: pp. 387–391.

[234] J. Talonen, H. Hänninen, Formation of shear bands and strain-induced martensite during plastic deformation of metastable austenitic stainless steels, Acta Mater. 55 (2007) 6108–6118.

[235] B. Thomas, G. Henry, J. Plateau, J. Hochmann, Effect of silicon on the stacking fault energy of 18 percent Cr 10 percent Ni stainless steel, Compt. Rend. Acad. Sic. 264 (1967) 31–34.

[236] X. Tian, Y. Zhang, Effect of Si content on the stacking fault energy in γ-Fe–Mn–Si–C

alloys: Part I. X-ray diffraction line profile analysis, Mater. Sci. Eng. A. 516 (2009) 73–77.

[237] S.W. Yang, J.E. Spruiell, Cold-worked state and annealing behaviour of austenitic stainless steel, J. Mater. Sci. 17 (1982) 677–690.

[238] P. Virtanen, R. Gommers, T.E. Oliphant, M. Haberland, T. Reddy, D. Cournapeau, E. Burovski, P. Peterson, W. Weckesser, J. Bright, SciPy 1.0: fundamental algorithms for scientific computing in Python, Nat. Methods. 17 (2020) 261–272. https://doi.org/https://doi.org/10.1038/s41592-019-0686-2.

[239] L. Breiman, Random forests, Mach. Learn. 45 (2001) 5–32.

[240] T. Chen, C. Guestrin, Xgboost: A scalable tree boosting system, in: Proc. 22nd ACM SIGKDD Int. Conf. Knowl. Discov. Data Min., 2016: pp. 785–794.

[241] N.L. Okamoto, S. Fujimoto, Y. Kambara, M. Kawamura, Z.M.T. Chen, H. Matsunoshita, K. Tanaka, H. Inui, E.P. George, Size effect, critical resolved shear stress, stacking fault energy, and solid solution strengthening in the CrMnFeCoNi high-entropy alloy, Sci. Rep. 6 (2016) 35863.

[242] L. Ward, S.C. O'Keeffe, J. Stevick, G.R. Jelbert, M. Aykol, C. Wolverton, A machine learning approach for engineering bulk metallic glass alloys, Acta Mater. 159 (2018) 102–111. https://doi.org/https://doi.org/10.1016/j.actamat.2018.08.002.

[243] D. Xue, P. V Balachandran, J. Hogden, J. Theiler, D. Xue, T. Lookman, Accelerated search for materials with targeted properties by adaptive design, Nat. Commun. 7 (2016) 11241. https://doi.org/10.1038/ncomms11241.

[244] M. Palumbo, B. Burton, A. Costa e Silva, B. Fultz, B. Grabowski, G. Grimvall, B. Hallstedt, O. Hellman, B. Lindahl, A. Schneider, P.E.A. Turchi, W. Xiong, Thermodynamic modelling of crystalline unary phases, Phys. Status Solidi. 251 (2014) 14–32. https://doi.org/10.1002/pssb.201350133.

[245] B. Hu, S. Sridar, L. Hao, W. Xiong, A new thermodynamic modeling of the Ti–V system including the metastable ω phase, Intermetallics. 122 (2020) 106791. https://doi.org/10.1016/j.intermet.2020.106791.

[246] V.S.Y. Injeti, Z.C. Li, B. Yu, R.D.K. Misra, Z.H. Cai, H. Ding, Macro to nanoscale deformation of transformation-induced plasticity steels: impact of aluminum on the microstructure and deformation behavior, J. Mater. Sci. Technol. 34 (2018) 745–755.

[247] T. Hastie, R. Tibshirani, J. Friedman, The elements of statistical learning: data mining, inference, and prediction, Springer Science & Business Media, 2009.

[248] S. Lu, Q.-M. Hu, B. Johansson, L. Vitos, Stacking fault energies of Mn, Co and Nb alloyed

austenitic stainless steels, Acta Mater. 59 (2011) 5728–5734. https://doi.org/https://doi.org/10.1016/j.actamat.2011.05.049.

[249] A. Das, Revisiting Stacking Fault Energy of Steels, Metall. Mater. Trans. A Phys. Metall. Mater. Sci. 47 (2016) 748–768. https://doi.org/10.1007/s11661-015-3266-9.

[250] Z. Jin, T.R. Bieler, A numerical force and stress analysis on a thin twin layer in TiAl, Philos. Mag. A. 72 (1995) 1201–1219.

[251] X. Wang, R.R. De Vecchis, C. Li, H. Zhang, X. Hu, S. Sridar, Y. Wang, W. Chen, W. Xiong, Design metastability in high-entropy alloys by tailoring unstable fault energies, Sci. Adv. 8 (2022) eabo7333.

[252] F. Otto, A. Dlouhý, C. Somsen, H. Bei, G. Eggeler, E.P. George, The influences of temperature and microstructure on the tensile properties of a CoCrFeMnNi high-entropy alloy, Acta Mater. 61 (2013) 5743–5755.

[253] J. Moon, M.J. Jang, J.W. Bae, D. Yim, J.M. Park, J. Lee, H.S. Kim, Mechanical behavior and solid solution strengthening model for face-centered cubic single crystalline and polycrystalline high-entropy alloys, Intermetallics. 98 (2018) 89–94.

[254] S. Guan, D. Wan, K. Solberg, F. Berto, T. Welo, T.M. Yue, K.C. Chan, Additive manufacturing of fine-grained and dislocation-populated CrMnFeCoNi high entropy alloy by laser engineered net shaping, Mater. Sci. Eng. A. 761 (2019) 138056. https://doi.org/https://doi.org/10.1016/j.msea.2019.138056.

[255] S.J. Sun, Y.Z. Tian, H.R. Lin, X.G. Dong, Y.H. Wang, Z.J. Zhang, Z.F. Zhang, Enhanced strength and ductility of bulk CoCrFeMnNi high entropy alloy having fully recrystallized ultrafine-grained structure, Mater. Des. 133 (2017) 122–127.

[256] J.M. Park, J. Choe, H.K. Park, S. Son, J. Jung, T.-S. Kim, J.-H. Yu, J.G. Kim, H.S. Kim, Synergetic strengthening of additively manufactured (CoCrFeMnNi) 99C1 high-entropy alloy by heterogeneous anisotropic microstructure, Addit. Manuf. 35 (2020) 101333.

[257] F. Weng, Y. Chew, Z. Zhu, X. Yao, L. Wang, F.L. Ng, S. Liu, G. Bi, Excellent combination of strength and ductility of CoCrNi medium entropy alloy fabricated by laser aided additive manufacturing, Addit. Manuf. 34 (2020) 101202. https://doi.org/https://doi.org/10.1016/j.addma.2020.101202.

[258] Q. Lin, X. An, H. Liu, Q. Tang, P. Dai, X. Liao, In-situ high-resolution transmission electron microscopy investigation of grain boundary dislocation activities in a nanocrystalline CrMnFeCoNi high-entropy alloy, J. Alloys Compd. 709 (2017) 802–807.

[259] Z. Wu, H. Bei, G.M. Pharr, E.P. George, Temperature dependence of the mechanical properties of equiatomic solid solution alloys with face-centered cubic crystal structures,

Acta Mater. 81 (2014) 428–441.

[260] W. Zhang, A. Chabok, B.J. Kooi, Y. Pei, Additive manufactured high entropy alloys: a review on the microstructure and properties, Mater. Des. (2022) 110875.

[261] Y. Wang, Y. Wang, R. Li, P. Niu, M. Wang, T. Yuan, K. Li, Hall-Petch relationship in selective laser melting additively manufactured metals: using grain or cell size?, J. Cent. South Univ. 28 (2021) 1043–1057. https://doi.org/10.1007/s11771-021-4678-x.

[262] M. Kang, J.W. Won, J.B. Kwon, Y.S. Na, Intermediate strain rate deformation behavior of a CoCrFeMnNi high-entropy alloy, Mater. Sci. Eng. A. 707 (2017) 16–21.

[263] J.X. Fu, C.M. Cao, W. Tong, Y.X. Hao, L.M. Peng, The tensile properties and serrated flow behavior of a thermomechanically treated CoCrFeNiMn high-entropy alloy, Mater. Sci. Eng. A. 690 (2017) 418–426.

[264] S.H. Joo, H. Kato, M.J. Jang, J. Moon, C.W. Tsai, J.W. Yeh, H.S. Kim, Tensile deformation behavior and deformation twinning of an equimolar CoCrFeMnNi high-entropy alloy, Mater. Sci. Eng. A. 689 (2017) 122–133. https://doi.org/10.1016/j.msea.2017.02.043.

[265] J.J. Licavoli, M.C. Gao, J.S. Sears, P.D. Jablonski, J.A. Hawk, Microstructure and Mechanical Behavior of High-Entropy Alloys, J. Mater. Eng. Perform. 24 (2015) 3685–3698. https://doi.org/10.1007/s11665-015-1679-7.

[266] J.B. Seol, J.W. Bae, Z. Li, J.C. Han, J.G. Kim, D. Raabe, H.S. Kim, Boron doped ultrastrong and ductile high-entropy alloys, Acta Mater. 151 (2018) 366–376.

[267] C. Haase, L.A. Barrales-Mora, Influence of deformation and annealing twinning on the microstructure and texture evolution of face-centered cubic high-entropy alloys, Acta Mater. 150 (2018) 88–103.

[268] G. Laplanche, J. Bonneville, C. Varvenne, W.A. Curtin, E.P. George, Thermal activation parameters of plastic flow reveal deformation mechanisms in the CrMnFeCoNi high-entropy alloy, Acta Mater. 143 (2018) 257–264.

[269] J. Li, H. Luan, L. Zhou, A. Amar, R. Li, L. Huang, X. Liu, G. Le, X. Wang, J. Wu, Phase transformation-induced strengthening of an additively manufactured multi-principal element CrMnFeCoNi alloy, Mater. Des. 195 (2020) 108999.

[270] Y.L. Wang, L. Zhao, D. Wan, S. Guan, K.C. Chan, Additive manufacturing of TiB2-containing CoCrFeMnNi high-entropy alloy matrix composites with high density and enhanced mechanical properties, Mater. Sci. Eng. A. 825 (2021) 141871.

[271] Y. Bai, H. Jiang, K. Yan, M. Li, Y. Wei, K. Zhang, B. Wei, Phase transition and heterogeneous strengthening mechanism in CoCrFeNiMn high-entropy alloy fabricated by

laser-engineered net shaping via annealing at intermediate-temperature, J. Mater. Sci. Technol. 92 (2021) 129–137.

[272] Y. Chew, G.J. Bi, Z.G. Zhu, F.L. Ng, F. Weng, S.B. Liu, S.M.L. Nai, B.Y. Lee, Microstructure and enhanced strength of laser aided additive manufactured CoCrFeNiMn high entropy alloy, Mater. Sci. Eng. A. 744 (2019) 137–144.

[273] M.A. Melia, J.D. Carroll, S.R. Whetten, S.N. Esmaeely, J. Locke, E. White, I. Anderson, M. Chandross, J.R. Michael, N. Argibay, Mechanical and corrosion properties of additively manufactured CoCrFeMnNi high entropy alloy, Addit. Manuf. 29 (2019) 100833.

[274] D. Zhao, Q. Yang, D. Wang, M. Yan, P. Wang, M. Jiang, C. Liu, D. Diao, C. Lao, Z. Chen, Ordered nitrogen complexes overcoming strength–ductility trade-off in an additively manufactured high-entropy alloy, Virtual Phys. Prototyp. 15 (2020) 532–542.

[275] C. Zhang, K. Feng, H. Kokawa, B. Han, Z. Li, Cracking mechanism and mechanical properties of selective laser melted CoCrFeMnNi high entropy alloy using different scanning strategies, Mater. Sci. Eng. A. 789 (2020) 139672.

[276] Z.G. Zhu, Q.B. Nguyen, F.L. Ng, X.H. An, X.Z. Liao, P.K. Liaw, S.M.L. Nai, J. Wei, Hierarchical microstructure and strengthening mechanisms of a CoCrFeNiMn high entropy alloy additively manufactured by selective laser melting, Scr. Mater. 154 (2018) 20–24.

[277] M. Jin, A. Piglione, B. Dovgyy, E. Hosseini, P.A. Hooper, S.R. Holdsworth, M.-S. Pham, Cyclic plasticity and fatigue damage of CrMnFeCoNi high entropy alloy fabricated by laser powder-bed fusion, Addit. Manuf. 36 (2020) 101584.

[278] A.H. Baghdadi, A. Rajabi, N.F.M. Selamat, Z. Sajuri, M.Z. Omar, Effect of post-weld heat treatment on the mechanical behavior and dislocation density of friction stir welded Al6061, Mater. Sci. Eng. A. 754 (2019) 728–734.

[279] N. Ahmed, I. Barsoum, G. Haidemenopoulos, R.K.A. Al-Rub, Process parameter selection and optimization of laser powder bed fusion for 316L stainless steel: A review, J. Manuf. Process. 75 (2022) 415–434.

[280] J.A. Cherry, H.M. Davies, S. Mehmood, N.P. Lavery, S.G.R. Brown, J. Sienz, Investigation into the effect of process parameters on microstructural and physical properties of 316L stainless steel parts by selective laser melting, Int. J. Adv. Manuf. Technol. 76 (2015) 869–879.

[281] M. Yakout, M.A. Elbestawi, S.C. Veldhuis, Density and mechanical properties in selective laser melting of Invar 36 and stainless steel 316L, J. Mater. Process. Technol. 266 (2019) 397–420.

[282] A. Dunn, J. Dagdelen, N. Walker, S. Lee, A.S. Rosen, G. Ceder, K. Persson, A. Jain,

Structured information extraction from complex scientific text with fine-tuned large language models, ArXiv Prepr. ArXiv2212.05238. (2022).

[283] E.A. Olivetti, J.M. Cole, E. Kim, O. Kononova, G. Ceder, T.Y.-J. Han, A.M. Hiszpanski, Data-driven materials research enabled by natural language processing and information extraction, Appl. Phys. Rev. 7 (2020) 41317.

[284] M.P. Polak, S. Modi, A. Latosinska, J. Zhang, C.-W. Wang, S. Wang, A.D. Hazra, D. Morgan, Flexible, Model-Agnostic Method for Materials Data Extraction from Text Using General Purpose Language Models, ArXiv Prepr. ArXiv2302.04914. (2023).

[285] M.P. Polak, D. Morgan, Extracting Accurate Materials Data from Research Papers with Conversational Language Models and Prompt Engineering--Example of ChatGPT, ArXiv Prepr. ArXiv2303.05352. (2023).

[286] J.-J. Zhu, J. Jiang, M. Yang, Z.J. Ren, ChatGPT and environmental research, Environ. Sci. Technol. (2023).